Transient Load-Speed Control in Multi-Cylinder Recompression HCCI Engines

by

Shyam Dilip Jade

A dissertation submitted in partial fulfillment
of the requirements for the degree of
Doctor of Philosophy
(Mechanical Engineering)
in The University of Michigan
2014

Doctoral Committee:
Professor Anna G. Stefanopoulou, Co-Chair
Erik Hellström, Ford Motor Company, Co-Chair
Professor Ilya V. Kolmanovsky
Professor Volker Sick

© Shyam Dilip Jade

All Rights Reserved
2014

To HCCI. Without you, it is safe to say that this work would not be possible.

Acknowledgments

I was warned that earning a Ph.D. would be a long and arduous struggle – a process designed to frustrate and weed out all those who are not utterly devoted. Although I've burned my fair share of the midnight oil and have questioned the direction of my research on numerous occasions, I must be one of the lucky ones, because all in all, the last four and a half years at the University of Michigan have been very enjoyable and fulfilling. There are a number of people who have made this possible. They have given me opportunities, and have helped shape me as both a researcher and a person.

I must first thank my research advisor and doctoral committee co-chair, Professor Anna Stefanopoulou. I will always be grateful for her trust when she hired me to work with her. Her work ethic, and her dedication to her research and her students are amazing to watch. The second co-chair of my committee – Dr. Erik Hellström – has had perhaps the largest influence on the technical content of my Ph.D. dissertation. He was exceptionally patient with my naïve questions when I started my research. He instilled in the lab the traditions of excellent Latex figures, and of *fika*. Erik is one of the smartest researchers I have met, and I have learnt a lot from him over the years. The members of my dissertation committee, Professors Kolmanovsky and Sick, have generously given me their time and expertise. I thank them for their contributions that have improved my work.

I would like to acknowledge all of the friends and colleagues I've worked with at the Autolab. I need to especially thank Jacob Larimore and Pat Gorzelic from the Powertrain Control Lab. We've worked together in our basement dungeon for the last three years, and they've been a constant source of help, inspiration, and entertainment. Not only are they really smart people who are a pleasure to work with, they've also taught me a lot about American culture – Jacob via his excellent barbecue, and Pat by simply being Pat. I would also like to express my appreciation to the talented group of researchers at the Autolab – Prasad Shingne, Stani Bohac, Aris Babajimopoulous, Adam Vaughan, Jason Siegel, Sandro Nuesch, Yi Chen, Jason Martz, Justin Negrete, Phil Bonkoski, and others – for their time, technical expertise, and friendship.

I have been fortunate to have worked on the ACCESS advanced combustion project for my Ph.D. research. I gratefully acknowledge the financial support of the Department of Energy and Robert Bosch LLC. This project has been a rich source of challenging and consequential research problems to work on. Along the way, I've met a number of intelligent, dedicated, and helpful people. I especially enjoyed working with folks like Jeff Sterniak, Julien Vanier, Li Jiang, Jason Schwanke and Oliver Miersch-Wiemers from Robert Bosch LLC, and Tom Marino from Roush. I look forward to working with the ENS group at Bosch after I graduate.

Finally, like so many international graduate students, I came to the US alone and with my family far away. My friends, both new and old, made sure that that I was never lonely, and have enriched my stay in Ann Arbor. I am truly indebted to my parents, Jui, and Anna for their constant love, support, and encouragement through the years.

Last but definitely not least, I would like to thank you, the reader. I hope that you find this work useful or, at the very least, interesting. I am available via email[1] if there is anything that you would like to discuss.

[1] mailto:sjade@umich.edu

Table of Contents

List of Tables

Table

List of Figures

Figure

List of Appendices

Appendix

Abstract

Strict proposed fuel economy and emissions standards for automotive internal combustion engines have motivated the study of advanced low-temperature combustion modes that promise higher combustion efficiencies with low engine-out emissions. This work presents modeling and control results for one such combustion mode – recompression homogeneous charge compression ignition (HCCI) combustion.

Regulating desired charge properties in recompression HCCI involves the retention of a large amount of the residual charge between engine cycles, thus introducing significant inter-cycle feedback in the system. This work considers a baseline controller from literature, and proposes two improved model-based control strategies. The controllers use exhaust valve timing and fuel injection timings to track combustion phasings during transitions in the HCCI region of the multi-cylinder engine load-speed operating map. Fast and stable control of these transitions is demonstrated, which maximizes the length of stay in the HCCI region, and hence the efficiency benefit of advanced combustion.

The baseline controller, which is a feedback-feedforward controller adapted from literature, is tuned using a low-order, discrete-time, control-oriented model that describes the stable, high efficiency HCCI region. The first improved control strategy augments the baseline controller with a reference or fuel governor that modifies transient fuel mass commands during large load transitions, when the possibility of future actuator constraint violations exists. This approach is shown in experiments to improve the combustion phasing and load responses, as well as prevent engine misfires.

Issues with high cyclic variability (CV) during late phasing and low load conditions, and their impact on transient performance, are discussed. These issues are physically explained through heat release caused due to unburned and recycled fuel in the recompression region. The control-oriented model is augmented with recompression heat release to predict the onset of the oscillatory, high variability region. The second improved control strategy uses this physical understanding of high CV to improve combustion phasing tracking performance during load and speed transients.

Transitions tested on a multicylinder HCCI engine include load transitions at fixed engine speeds, engine speed ramps at fixed load conditions, simultaneous load and speed transitions, and select FTP75 drive-cycle transitions with high load slew rates. This improved model-based control strategy is proposed as a solution for the HCCI transient control problem.

Chapter 1

Introduction

1.1 Background

Internal combustion engines have played a central role in the modern world over the last century. However, serious concerns about vehicular pollutants and energy sustainability have led to ever tightening emissions and fuel economy legislation, examples of which can be found in Fig. 1.1 and Tab. 1.1. Figure 1.1 presents actual and projected fuel economy mandates in various regions in the world, while Tab. 1.1 presents a historical perspective on vehicular emissions mandates in the US and the European Union. Zero-emission transportation solutions such as electric battery and fuel cell based vehicles still face issues of cost, practicality, performance and infrastructure development. These are long term solutions that may take decades to significantly displace fossil-fuel based vehicles [9]. Thus in the short and medium term, a combination of several advanced internal combustion engine technologies need to be developed and brought to the market to meet aggressive fuel and emissions targets [10]. Examples of such internal combustion engine technologies include engine improvements (such as advanced combustion, variable valve lift and timing, cylinder deactivation, turbocharging and downsizing), transmission technologies (such as higher speed automatic transmissions, and improved dual clutch transmissions), and partial electrification (such as start-stop technologies, and regenerative braking systems) [10]. This dissertation focuses on HCCI (homogeneous charge compression ignition) combustion, which is one such promising combustion technology for gasoline internal combustion engines.

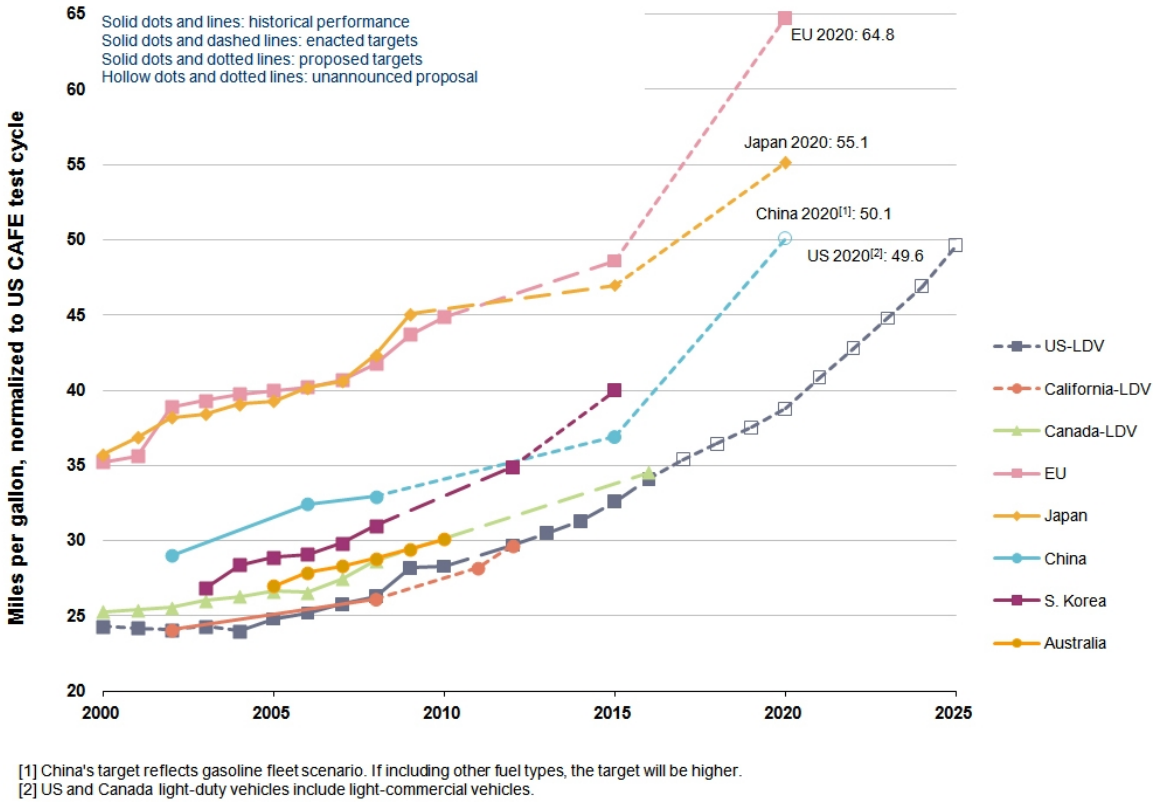

Figure 1.1: Comparison of actual and projected fuel economy targets for new passenger vehicles across different regions. Source: [2].

Year	**HC** (g/km)	**CO** (g/km)	**NO$_x$** (g/km)	**PM**
1957—1962 USA Fleet	5.5	51	2.3	-
1963—1967 USA Fleet	5.7	58	2.2	-
1975/76 USA Federal	0.94	9.4	1.9	-
1991 USA Federal	0.26	2.1	0.6	-
1994 USA Federal	0.26	2.1	0.25	-
2000 Euro III (gasoline @ 80000 km)	0.20	2.4	0.15	-
2004 USA Federal	0.08	1.1	0.13	-
2000 Euro IV (gasoline @ 100000 km)	0.10	1.0	0.08	0.005
2007 USA Federal (Tier II Bin 5 average @ 80000 km)	0.05	2.1	0.03	-

Table 1.1: Emissions standards history for light duty vehicles. Source: [1]

.

1.1.1 Homogeneous Charge Compression Ignition

The HCCI combustion strategy aims to combine the high efficiency of diesel engines with the lower cost emissions after-treatment systems of gasoline engines [11–13]. It is characterized by compression-driven near simultaneous auto-ignition events at multiple sites throughout a uniformly mixed air-fuel-residuals mixture. The HCCI combustion event occurs nearly instantaneously, with no discernible flame front.

HCCI is known by other names in literature, such as ATAC (Active Thermo Atmospheric Combustion) and CAI (Controlled Auto-Ignition). It was first explored in gasoline engines in the late 1970s by researchers such as Onishi et al. [14], who noted improvements in fuel economy and emissions through gasoline auto-ignition in two-stroke engines. Noguchi et al. [15] used optical measurements to observe ignition at multiple sites throughout the charge, without a flame front. Najt and Foster [16] extended the work to four-stroke engines using intake air heating. Thring [17] examined the effect of external EGR and air-fuel ratios on HCCI combustion. It took several years for engine technology, such as variable valve actuation, electronic engine control, and in-cylinder pressure sensors, to become cost-effective and reliable enough to implement HCCI combustion in commercial vehicles. One of the first production HCCI automotive engines was a Honda two-stroke motorcycle engine in 1997 [18]. The use of variable valve actuation to set up and control recompression HCCI, the strategy used in this work, was mentioned in papers such as [19].

Advantages of HCCI

HCCI has been the focus of a large amount of research in recent years, due to its various benefits [11–13]. HCCI combustion can be achieved with fuel-air mixtures significantly leaner than in conventional spark ignited (SI) engines. The high level of diluents in the lean mixture causes low temperature combustion (LTC), which has several thermodynamic efficiency advantages. The resulting increased specific heat ratio during expansion increases the thermal efficiency and the work output [20]. There is also a gain in thermodynamic efficiency thanks to the rapid heat release, which brings the combustion process closer to a constant volume heat release versus typical SI combustion. The lower temperatures reduce heat transfer losses to the cylinder walls, and reduce NO_x emissions to very low levels. Low engine-out emissions mean that there is no need for expensive after-treatment systems, as opposed to lean stratified gasoline or diesel combustion [21]. CO and unburned HC emissions can be higher in HCCI than SI due to low temperature and higher dilution, but

these are easier / cheaper to take care of than NO_x. High compression ratios may be used with HCCI combustion, further increasing theoretical combustion efficiency. Innovative variable valve actuation strategies can be used to achieve what is called "internal de-throttling" [19]. This means that HCCI combustion can be run with the throttle kept wide open, hence reducing throttling losses and significantly improving fuel economy at part-load conditions. Thus, HCCI combustion promises higher fuel efficiency than conventional SI engines, with intrinsically low emissions.

Challenges of HCCI

There are several technical and cost-related challenges inherent in HCCI combustion that must be overcome before it can be commercially implemented.

HCCI combustion cannot be used over the entire engine load-speed operating region. The near instantaneous combustion event means that high rates of pressure rise at high load conditions may cause significant engine noise, and potential engine damage [22]. The use of HCCI combustion at low load levels is complicated by the need to prevent charge temperatures from dropping too low to sustain autoignition. Further, at low loads the peak burned gas temperatures are too low to complete the CO to CO_2 oxidation reaction [23], and combustion efficiency drops significantly. The use of HCCI is feasible over a limited load range, and is typically used as part of a multi-mode combustion strategy to cover the entire engine operating map, thus increasing cost and complexity. Further, the multi-mode combustion requirement of preventing engine knock when using SI at maximum load conditions forces the use of a lower compression ratio than is optimal for HCCI.

From a controls perspective, the primary challenge in HCCI combustion control is the lack of a direct ignition trigger, such as the spark in a spark ignition engine, or the fuel injection in a diesel engine. The nature and start of combustion is fixed by the temperature, pressure and composition of the in-cylinder charge. The mixture in the engine cylinder proceeds to combustion via an autoignition reaction [12]. Combustion can only be controlled indirectly, by carefully regulating the properties of the in-cylinder mixture. The significant cycle-to-cycle feedback through the retained exhaust gases in recompression HCCI, as discussed in Chap. 2, increases the difficulty of regulating the in-cylinder charge properties. The challenges faced in controlling HCCI combustion require the use of novel and innovative actuation strategies such as variable valve timing, variable injection timing, split injection, rebreathing, and intake air system heat exchangers. These add cost and complexity to the engine design, but

make control design more interesting and important.

1.2 Transient HCCI Control

Transitions in the HCCI operating region include a combination of load, speed, and reference combustion phasing changes. Combustion phasing must be maintained within a tightly controlled range at all time, and especially during transients, else ringing or stability limits can be violated. Since HCCI combustion is driven by thermally dominant autoignition reactions [24], combustion phasing control in recompression HCCI is achieved by carefully regulating the thermal conditions in the cylinder. This makes load-speed transitions in HCCI challenging, as load and speed variations can have a significant effect on in-cylinder thermal conditions, if they are not correctly compensated for. Engine load in HCCI, similar to other lean combustion modes, is a strong function of the injected fuel mass, which also has a strong effect on the charge temperature. Similarly speed variations can affect charge temperature through heat transfer and residual trapping effects. The transitions that are of greatest concern are load and speed reductions, as these tend to phase combustion later, and hence increase the risk of engine misfire. These concerns make transient HCCI combustion phasing control an interesting controls challenge.

1.2.1 HCCI Combustion Control in Literature

Several HCCI combustion control schemes have been proposed in literature. Basic solutions for HCCI combustion timing control involve single-input single-output controllers, see for example [25–27]. Olsson et al. [25] use three decentralized PID controllers for the inlet heater, fuel charge, and fuel composition to track inlet temperature, engine load, and combustion timing respectively. Agrell et al. [26] use a PID controller to actuate a variable valve system that regulates a filtered combustion timing signal. Souder et al. [27] use microphones and knock sensors to detect the location of combustion, and use a throttle in the exhaust to control it.

More complex multi-input multi-output control strategies have been proposed as well. Agrell et al. [28] control combustion timing using two PI controllers – one actuating valve overlap to affect the amount of trapped residuals, and the other actuating IVC timing to affect the effective compression ratio. Here only one controller is active at a time, with logic-based switching between them. State feedback controllers using

techniques such as LQG are seen in literature, for example [29–31]. Dynamic feedback linearization is used to synthesize a nonlinear tracking controller in [32] to control phasing, peak pressure and work output. Techniques such as extremum seeking have been used to tune gain scheduling parameters for more basic controllers in [33]. Mid-ranging, a two-input single-output control architecture used as the baseline controller in this work, has been applied to HCCI engine control problems, see [34, 35].

Solutions to the HCCI control problem using optimal control schemes have been proposed, see for example [36–38]. However, these involve the on-line solving of a nonlinear optimization problem where the stabilization, tracking and actuator constraint requirements have to be satisfied simultaneously. This problem is simplified in the current work through the implementation of the fuel governor, which reduces computation time compared to higher-dimensional optimal control schemes, at the cost of reduced flexibility in shaping the transient response.

1.3 Dissertation Contributions

The key contributions of this thesis are two low-order control-oriented models for recompression HCCI combustion, with two corresponding model-based control strategies that track combustion phasing during HCCI transient operation. The two controllers are presented as improved versions of a baseline controller adapted from literature. The first model and control strategy focus on the stable dynamical region of HCCI combustion, where HCCI operation is typically commanded for efficiency reasons. The second model and controller are capable of operating in the oscillatory, boundary regions of the HCCI operating regime. Typically one avoids operating in these regions at steady state, because they are characterized by high cyclic variability and lower efficiency. However, it is seen in this dissertation that identifying and controlling combustion in these regions can be very important during transient HCCI operation. The second controller demonstrates excellent transient combustion phasing tracking performance, and is proposed as a viable solution to the HCCI load-speed transition control problem. The contributions of the dissertation are summarized as follows:

1. Reference Governor Controller:
   (a) Development of a low-order control-oriented model for recompression HCCI combustion with two dynamic states representing thermal and composition dynamics. The model is validated across a range of loads and speeds, and for both steady state and transient conditions.
   (b) Implementation of the reference governor / fuel governor control strategy for HCCI load transition control. It is demonstrated that preventing actuator

saturation by intelligently filtering the desired load command can improve the performance of a sub-optimal baseline controller.

2. Load & Speed Transition Controller:
   (a) Augmenting the previously developed control-oriented model with a more physical combustion efficiency regression, and recompression heat release caused due to the presence of significant amounts of unburned and recycled fuel. By characterizing the onset of the high cyclic variability (CV) HCCI region across different fueling levels, this new combustion model is shown to predict mean combustion phasing as well as the nature of CV across low CV and high CV dynamical regions.
   (b) Design of a feedback gain scheduled controller that determines the nature of the system dynamics (damped or oscillatory) and applies appropriate control actions.
   (c) Experimental demonstration that this improved controller can track combustion phasing during load-speed transitions similar to those seen in a typical drive-cycle (FTP-75).

The research work presented in this dissertation was carried out as part of the ACCESS (Advanced Combustion Concepts – Enabling Systems and Solutions) project. This project, supported by the Department of Energy, aims to develop systems and control strategies that enable the use of, and the switching between, multiple high efficiency combustion concepts including HCCI, SACI (spark assisted compression ignition) and turbocharged SI (spark ignition). The goal of the project is to develop a downsized, turbocharged, multi-mode combustion engine that demonstrates a 25% fuel economy improvement compared to the baseline engine, while satisfying the SULEV emissions specification [39].

1.4 Dissertation Outline

The structure of the thesis is shown in Fig. 1.2. The HCCI actuation strategy used in this work, recompression, is discussed in Chap. 2. The actuators available for control and the outputs to be controlled are introduced. The experimental setup includes the multicylinder HCCI engine, the engine dynamometer, and the software and hardware toolchain.

A discrete-time, physics-based, control-oriented model for HCCI combustion with thermal and composition states is presented in Chap. 3. Steady state and transient validation results are presented. This model is used to develop a model-based reference or fuel governor in Chap. 4. In the first part of the chapter, a feedback-feedforward mid-ranging controller is adapted from literature that uses the fuel injection timings

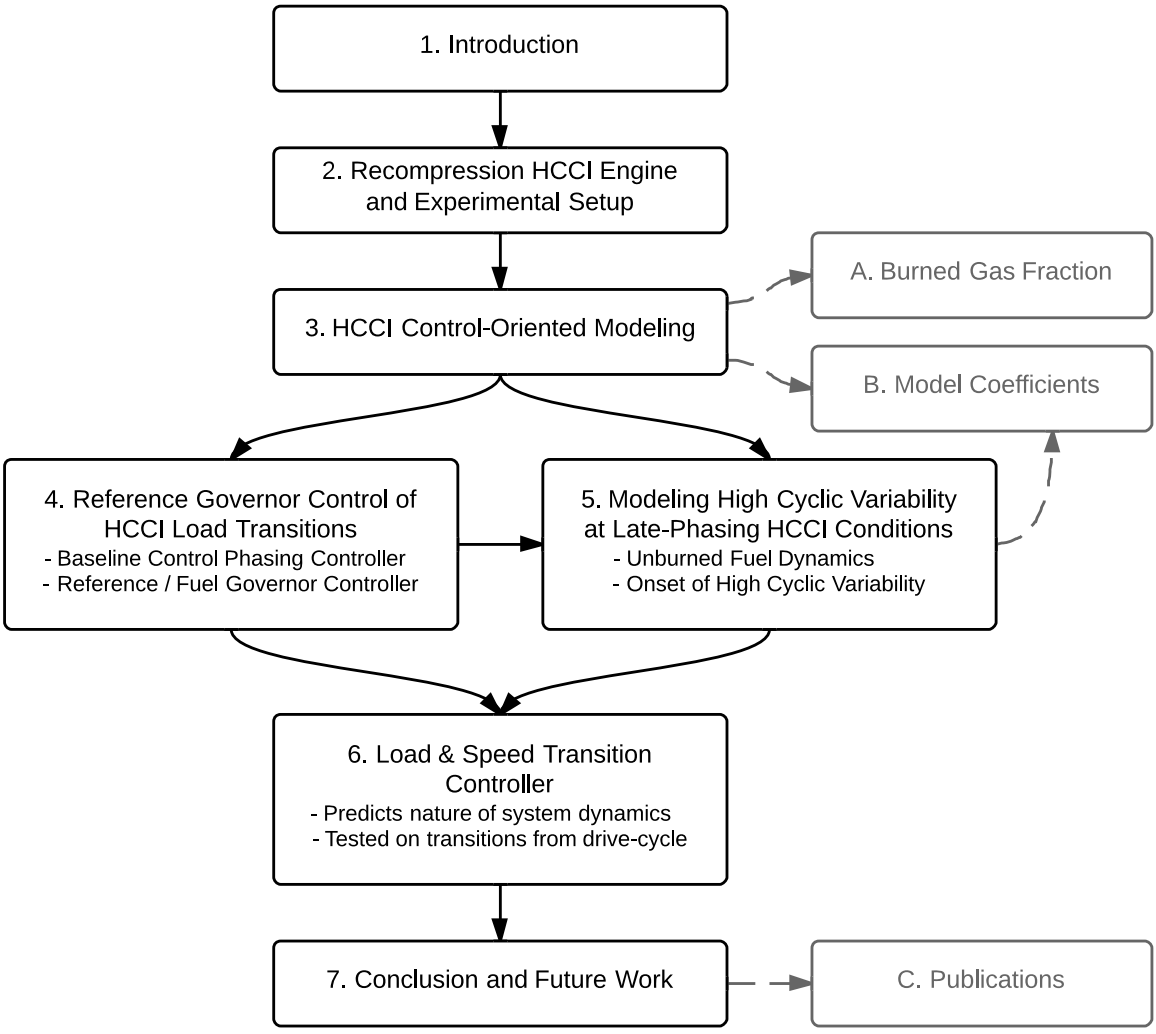

Figure 1.2: Outline of the dissertation.

and exhaust valve closing timing inputs to regulate the combustion phasing performance output. This controller serves as the baseline controller to compare other control strategies against. It is experimentally shown that the baseline controller regulates combustion phasing well for small HCCI load steps, but fails to prevent engine misfires during larger load steps, where the possibility of actuator constraint violations exists. The fuel governor is developed in the second part of the chapter to improve this performance. The governor is added to the compensated system and attenuates the desired fuel amount change when the possibility of future actuator constraint violations exists. Improvements in regulation performance are demonstrated experimentally. A computationally-cheap variant of the fuel governor is demonstrated that is suitable for implementation on commercially available ECU hardware.

In spite of the improved performance, it is experimentally seen in Chap. 5 that increased cyclic variability (CV) is observed at late phasing conditions or at low load conditions. This variability limits the range of load transitions that can be controlled by the fuel governor, since HCCI transitions can traverse regions of high CV, even if the steady state transition end points are stable with low CV. The physical cause of these cyclic variations is seen to be heat release from unburned fuel caused by the high amounts of recycled charge in recompression HCCI, coupled with low main combustion efficiency at these low load or late phasing conditions. Heat release results are used to determine the onset of the high cyclic variability at different operating points as a function of the peak cylinder temperature. These observations motivate the development of the second control-oriented model that can predict mean combustion phasing and the nature of variability in both low CV and high CV dynamical regions.

The physical insights into the cause and nature of high CV is used to develop a load and speed controller in Chap. 6. This controller integrates controller design work in both the low CV and high CV HCCI operating regions to develop a two-input single-output controller that uses valve and fuel injection timings to track combustion phasing in both dynamic regions. Novel aspects of the controller include nonlinear model-inversion based feedforward, and gain scheduled feedback that reduces transient CV. Linear analysis is used to discuss closed-loop stability, as well as the performance benefits of the gain scheduling strategy. Transitions tested on a multicylinder HCCI engine include load transitions at fixed engine speeds, engine speed ramps at fixed load conditions, simultaneous load and speed transitions, and select FTP75 drive-cycle transitions with high load slew rates. Good combustion phasing tracking performance is demonstrated, and misfires are prevented.

Finally in Chap. 7, the work presented in this thesis is summarized and future

work is discussed. There are three appendices in this work. Appendix A discusses the definition of the burned gas fraction dynamic state, and its relationship with the molar fraction of oxygen in the charge. Appendix B presents the numeric values of the model coefficients discussed in Chap. 3 and Chap. 5. Finally Appendix C lists the author's publications.

Chapter 2

Recompression HCCI Engine and Experimental Setup

2.1 Recompression HCCI

Auto-ignition in HCCI combustion is a thermally-driven chemical kinetic process [11]. To phase auto-ignition around top dead center (TDC), the thermal energy of the pre-combustion charge has to be significantly higher than that typically seen in conventional spark ignition (SI) combustion at the same engine load-speed operating point. Several different actuation strategies are seen in literature to supply this increased thermal energy.

One way to increase the thermal energy at TDC is to use engines with extremely high compression ratios. However in practice the maximum compression ratio of a multi-mode combustion engine is limited, due to knock considerations at higher load conditions in the SI combustion mode. An alternative strategy is to increase the temperature of the charge through intake air heating. Najt and Foster [16] used this method to achieve HCCI combustion in one of the original HCCI implementations. The slow response time of this method makes it unsuitable for cycle-to-cycle combustion phasing control. Some researchers improve the speed of response by mixing hot and cold air to modify the intake air temperature, but this strategy poses practical implementation concerns [40, 41]. Other researchers have used variable compression ratio as an actuation strategy for HCCI combustion [42, 43]. Novel valve actuation strategies such as rebreathing or recompression have also been used to actuate HCCI. In rebreathing HCCI, the exhaust valve is opened for a second time to reinduct some of the exhausted gas. The rebreathing lift is controlled to modulate the exhaust reinduction and increase the thermal energy of the charge. The strategy chosen in the current application is recompression, which is an efficient and relatively quick strategy for affecting the temperature of the pre-combustion charge that can be implemented with

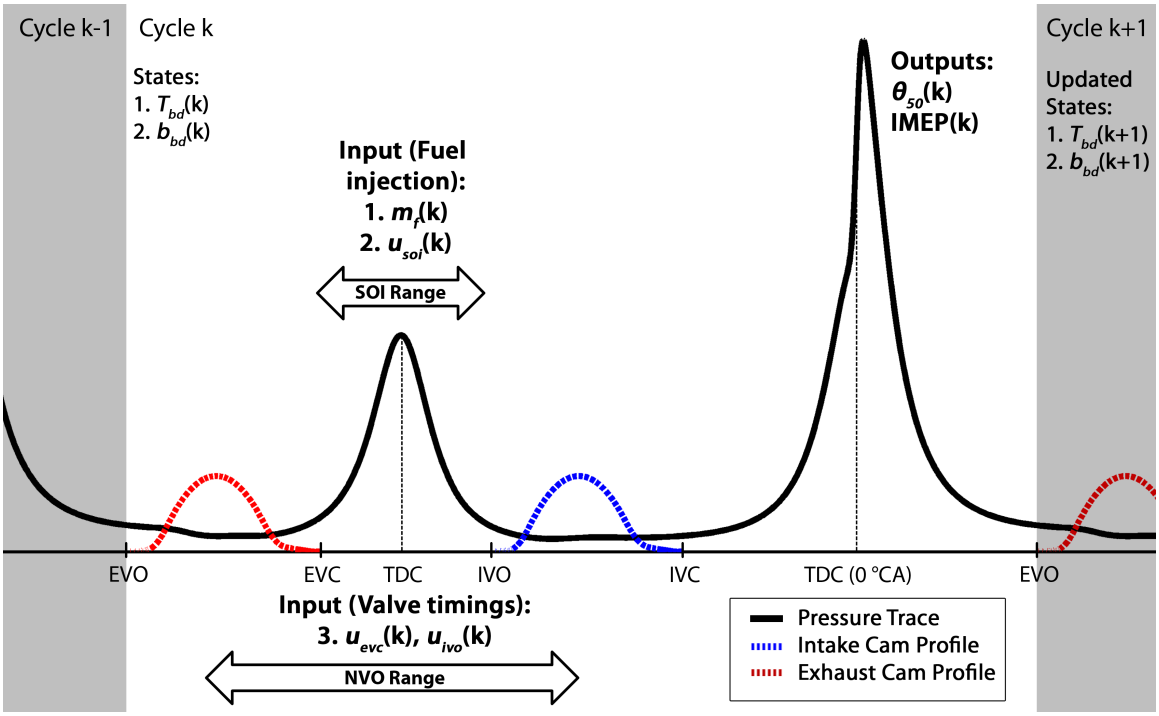

Figure 2.1: Typical recompression HCCI pressure trace, showing the relative locations of inputs, outputs and states. These quantities are defined in Sec. 2.3, Sec. 2.4 and Sec. 3.2 respectively.

production ready technology [19,44]. Further, it allows for fast and cylinder-individual combustion phasing authority through the timing of injection in the recompression region.

In recompression HCCI the exhaust valve is closed early and the intake valve is opened late, compared to typical spark ignition operation [19]. The resulting negative valve overlap (NVO) can be seen in the typical recompression HCCI in-cylinder pressure trace of Fig. 2.1. A large fraction of the in-cylinder charge is trapped before it can be exhausted. These hot residual gases that are retained between engine cycles have a significant impact on the temperature and composition of the in-cylinder charge of the subsequent cycle. This internal coupling between cycles is quantified by the residual gas fraction (x_r). This is defined as the mass fraction of the total charge that is trapped during NVO.

$$x_r(k) = \frac{\text{Mass of residuals}}{\text{Mass of charge}} = \frac{m_{res}(k)}{m_c(k)} \tag{2.1}$$

The residual gas fraction cannot be measured directly, but is estimated by pressure

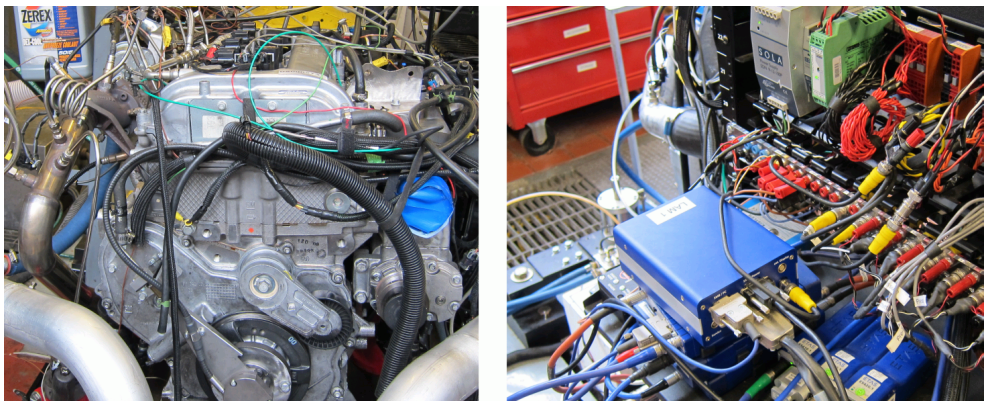

Figure 2.2: Picture of the experimental setup at the University of Michigan.

trace analysis to be very large in the current application, between 40% and 70%. Correctly predicting the amount, temperature and composition of these residual gases is key to modeling the recompression HCCI process.

2.2 Experimental Setup

A turbocharged, direct-injection, inline four cylinder GM LNF Ecotec engine with an engine displacement of 2.0 liters was used in this work, see Tab. 2.1 and Fig. 2.2. Premium grade indolene fuel was used for all experiments. Modifications to the engine for HCCI combustion included an increased geometric compression ratio of 11.25:1, and shorter duration and lower lift cam profiles to allow for unthrottled operation. In addition to the stock turbo charger, an Eaton M24 supercharger was used to boost intake manifold pressure. Most of the results presented in this work were run at slightly boosted conditions, approximately 1.1 bar intake manifold pressure. The relative air-fuel ratio λ varied between $1 \rightarrow 1.3$. Engine coolant temperature was controlled to a set-point of 90 °C for all tests. The spark was left on to prevent fouling, but was fixed at 40 °CA after top dead center (aTDC) to prevent interference with HCCI combustion.

In-cylinder pressure was sampled at a resolution of 0.1 °CA for offline pressure trace analysis, and at a resolution of 1 °CA for real-time estimation of combustion features. The offline analysis tool estimates the mass fraction burned curve, the work output, the in-cylinder temperature trace, the residual gas fraction and the cylinder mass flows. Details of the offline heat release analysis method can be found in [6,45,46]. Combustion phasing (θ_{50}) used in feedback control was estimated using the built-in functionality of the Bosch Motronic MED17 engine control unit (ECU). The θ_{50} and

Table 2.1: Experimental engine geometry

Parameter	Value	Parameter	Value
Displacement	2.0 L	Bore	86 mm
Number of cylinders	4	Stroke	86 mm
Compression ratio	11.25	Connecting rod length	145.5 mm
Wrist Pin Offset	0.8 mm		

IMEP predictions from the ECU were validated with values obtained from offline pressure trace analysis, and they differ only by fixed offsets.

The control strategies were implemented using C and Matlab code, and were tested in real-time using an ETAS ES910 rapid prototyping module. The module uses an 800 MHz Freescale PowerQUICC™ III MPC8548 processor with double precision floating point arithmetic and 512 MB of RAM.

The engine and air path hardware were not fully optimized for HCCI combustion – rather they were chosen to enable the usage of, and switching between, several different combustion modes. This affects design decisions such as the engine compression ratio, the choice of the turbocharger and supercharger, the crank angle offsets between the high lift and low lift cam profiles, and the shape of the cam profiles. The HCCI control strategy must be able to control HCCI combustion under these non-optimal conditions, if it is to be successfully implemented in commercial applications.

2.3 Control Actuators

The actuator inputs considered for control are the exhaust valve closing timing (u_{evc}), start of fuel injection timings (u_{soi}), and masses of fuel injected (m_f^{inj}). Of these actuators, u_{soi} and m_f^{inj} can be actuated on a cylinder-to-cylinder basis, while u_{evc} is fixed for all cylinders. Spark timing, which is an important phasing control actuator in SI combustion, has almost no effect on the phasing of the lean, highly dilute HCCI combustion. Environmental conditions such as the pressure and temperature of the intake and exhaust manifolds affect the combustion, but these are not controlled.

2.3.1 Exhaust Valve Closing Timing

During the negative valve overlap, the trapped residual gases undergo a secondary compression and expansion. Manipulating the exhaust valve closing timing (u_{evc})

changes the the mass fraction of hot residuals trapped in the cylinder. This affects the temperature of the subsequent pre-combustion gas mixture, thus significantly influencing the timing of combustion.

Valve timings in this study are controlled by a hydraulic cam phasing actuator that phases (moves) the intake or exhaust cams of all cylinders in the engine simultaneously. This means that the cam phasing actuator cannot be used for cylinder-individual control. The cam profiles are fixed, which means that the valve opening and closing timings cannot be changed independently. In this study the exhaust cam position is varied, while the intake cam position is fixed. The cam phasing actuator is slow and is subject to a rate constraint.

2.3.2 Start of Fuel Injection Timing

The timing of the start of fuel injection (u_{soi}) is recognized in literature as a important part of the control strategy for recompression HCCI engines [19, 35, 47]. As seen in Fig. 2.1, the entire fuel amount is injected in a single fuel injection, the timing of which can be varied within the recompression region. The start of fuel injection timing (u_{soi}) can be set independently for each cylinder, and is thus useful for cylinder-to-cylinder combustion phasing balancing. This is an important advantage of the recompression actuation strategy as compared to rebreathing. It can also be set independently from cycle-to-cycle, which makes u_{soi} a fast actuator with no rate constraints.

Injecting fuel into the hot residual gases has complex thermal and chemical effects [47]. Chemical reactions are initiated between the fuel and the hot excess air leading to possible heat release. The larger fuel molecules may also break down into smaller hydrocarbons. Finally, the specific heat capacity ratio $\left(\gamma = \frac{c_p}{c_v}\right)$ of the mixture changes after u_{soi}. The net effect of these complex interactions is earlier auto-ignition during the next combustion event. Injecting earlier in the recompression region leads to more time for these heat release and pyrolysis effects, and consequently earlier auto-ignition. Variable fuel injection timing shows promising results in HCCI combustion control [35, 48]. Varying u_{soi} does not have a large effect on the engine load in general. However, very early fuel injections can adversely affect pumping work and emissions [49].

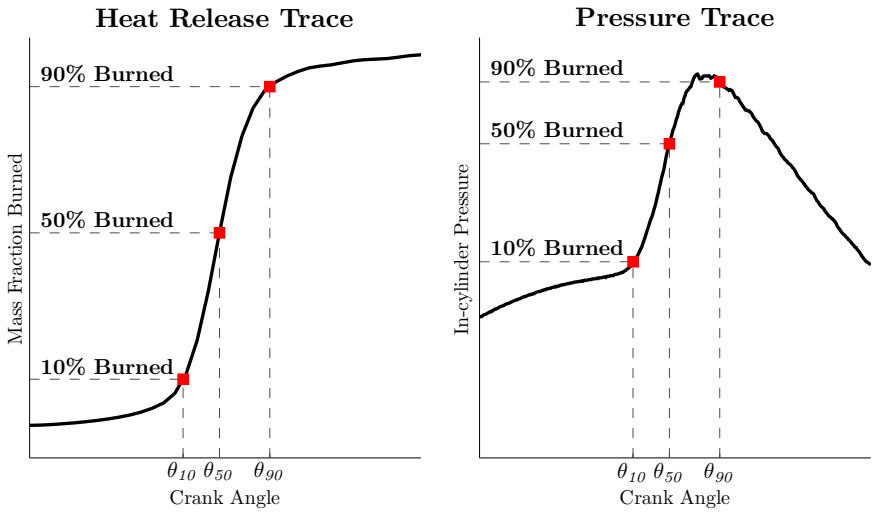

Figure 2.3: Engine crank angles where 10%, 50%, and 90% of the heat release occur.

2.3.3 Mass of Fuel Injected

The mass of fuel injected (m_f^{inj}) per cycle is typically used in multi-cylinder SI engines to regulate the air-fuel ratios of the individual cylinders to stoichiometric conditions. HCCI combustion does not need to be run at stoichiometric air-fuel conditions, and so m_f^{inj} can be used for other objectives. Fuel mass is strongly correlated with the load or work output (IMEP) of the cylinder, and is hence used to control the desired engine load. The mass of fuel injected can be varied independently for each cylinder, and so can be used for cylinder-to-cylinder load balancing. In Chap. 4, the m_f^{inj} transients will be shaped to smooth load transitions in HCCI engines.

As discussed in Chap. 1, varying the fuel mass has a significant effect on charge temperature, and consequently on combustion phasing. During load transitions, these undesirable changes in combustion phasing need to be compensated for by the other control inputs, namely u_{soi} and u_{evc}.

2.4 Performance Outputs

The primary performance output of the model is combustion phasing or timing. This is quantified by the location of θ_{50}, which is the engine crank angle at which 50% of the total heat release occurs. This angle has proven to be a reliable indicator of the location of combustion [25, 50]. In practice, the mass fraction burned curve is computed through heat release analysis of the in-cylinder pressure traces. It is preferable to use θ_{50} to characterize combustion as its location is relatively insensitive

to changes in the heat release analysis assumptions. Figure 2.3 shows the location of the engine crank angles where 10%, 50%, and 90% of the heat release occur. The mass fraction burned curve (left) is computed offline, from the measured in-cylinder pressure trace (right).

The work output, represented by the indicated mean effective pressure (IMEP), is another important output. It is defined [20] as the total pressure-volume work integrated over the entire engine cycle, normalized by the displacement volume (V_d):

$$\text{IMEP} = \oint p \frac{\text{dV}}{V_d} \tag{2.2}$$

where p and V are the in-cylinder pressure and volume respectively. IMEP is seen to be a very strong function of the mass of fuel injected (m_f^{inj}).

The final performance output of the model is the air-fuel equivalence ratio λ which relates to the mass flow through the engine. This is defined as the mass ratio of the air and the fuel in the cylinder, normalized by the stoichiometric air-fuel ratio (AFR_s):

$$\lambda = \frac{AFR}{AFR_s} = \frac{1}{AFR_s} \frac{m_{air}}{m_f}. \tag{2.3}$$

Chapter 3

HCCI Control-Oriented Modeling

To design a model-based combustion phasing controller for a multi-cylinder recompression HCCI engine, one needs to develop a control-oriented model that both captures important dynamics, and that is simple enough for controller development purposes. HCCI combustion models seen in literature are surveyed in Sec. 3.1. The structure of the control-oriented model used in this work is presented in Sec. 3.2. The dynamic state evolution in the cylinder is split into two phases. The first phase involves the coupling between the cycles, see Sec. 3.3, where the large mass fraction of trapped residual gases sets up significant thermal and composition couplings between engine cycles. The second phase models the behavior within the cycle, see Sec. 3.4. The evolution of the in-cylinder temperature and composition have a large influence on the model outputs such as the combustion phasing, see Sec. 3.5, and the cycle-averaged mass flows, see Sec. 3.6. The nonlinear model equations are summarized in Sec. 3.7, and a linearization around a nominal operating point is discussed in Sec. 3.8. This linearized model is used in controller gain tuning and development. Validation results are presented in Sec. 3.9 for both steady state and transient conditions. Finally, the model is summarized in Sec. 3.10.

This model is developed for operating regimes with low variability and near complete combustion. In general it is desired that combustion be maintained in these regions for driveability and fuel economy. Late phasing conditions with high cyclic variability are considered in Chap. 5.

3.1 HCCI Models in Literature

Higher fidelity simulation models incorporate complex chemical or air path dynamics into combustion prediction, and are useful in understanding the fundamentals of HCCI combustion. Bengtsson et al. [51] propose an HCCI model using the Shell model [52]

for combustion. This combustion model is a lumped chemical kinetics model using five representative species in eight generic reactions. Babajimopoulos et al. [44] develop a single-cylinder HCCI engine model augmented with 1-D engine gas flow dynamics. The predictive combustion model uses an Arrhenius integral to predict the start of combustion, and heat release correlations based on a CFD model coupled with a multi-zone detailed chemical kinetics solver. Misfire in HCCI engines in studied by Mayhew et al. [53] using a simplified eight state model. Other researchers have used system identification techniques to generate HCCI models, see for example [31].

Low-order, physics-based models are needed for combustion controller and observer design. In literature these models usually describe combustion using a few lumped states, and augment combustion with thermal feedback dynamics between cycles. Shaver and Gerdes [54] studied HCCI combustion controlled by re-inducted exhaust gases and presented a low-order model to control peak in-cylinder pressure. The model is formulated with the composition of the in-cylinder charge prior to combustion as an input. A cycle-resolved model that captures the effects of the rebreathing lift actuator and external EGR on rebreathing HCCI combustion was developed by Rausen et al. [55]. In this model, the cylinder is modeled as a pump with cycle-averaged mass flow. Chiang et al. [56] extend this model by improving the intermediate models for the combustion efficiency, and the flow and temperature of the reinducted exhaust gas. Blom et al. [57] develop a model emphasizing the thermal interaction between the combustion and the cylinder walls. The model proposed by Shahbakhti and Koch [58] for an HCCI engine with intake air heating and external EGR is validated for a range of fuels and engine speeds. Ravi et al. [35, 59] propose control-oriented models for recompression HCCI engines using multiple fuel injections. The effect of the earlier pilot injection is modeled as a change in the Arrhenius threshold, which is an analytical construct used to model combustion timing as a function of the thermodynamic state.

3.2 Model Structure

HCCI combustion is a chemical kinetics driven process. Correctly determining the temperature, pressure and composition of the in-cylinder charge is crucial to predict the combustion characteristics. The Input-Output representation of the discrete-time recompression HCCI model is shown in Fig. 3.1, and the relative locations in crank-angle space of the inputs, outputs and states can be seen in the typical recompression HCCI pressure trace of Fig. 2.1. There are two dynamic states – the temperature of

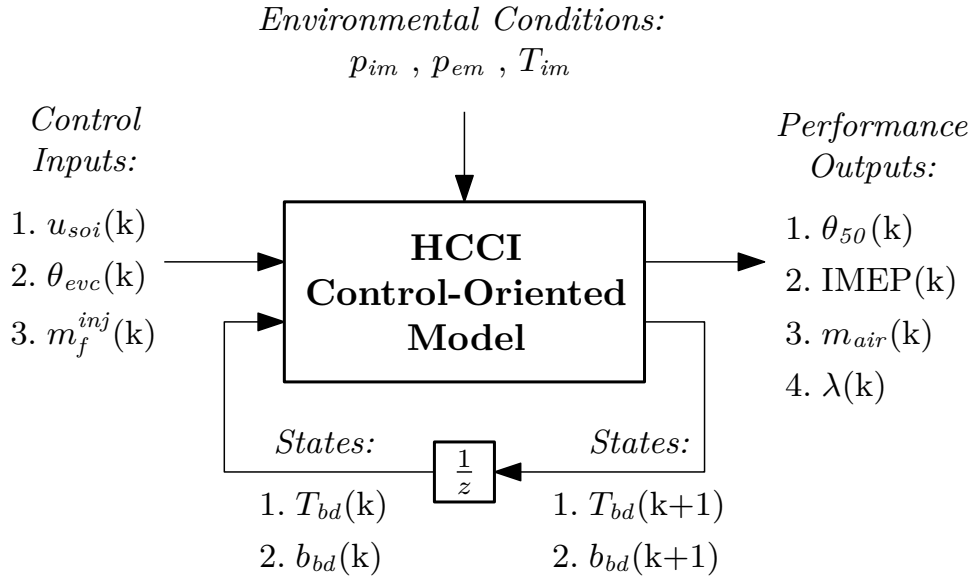

Figure 3.1: Model overview showing the inputs, outputs and states of the model.

the blowdown gases (T_{bd}) and the burned gas fraction of the blowdown gases (b_{bd}) – representing thermal and composition couplings between the cycles respectively. In this work, the cylinder charge is modeled as a mixture of three species – fuel, air and burned gases. Composition dynamics are represented by changes in the fraction of the burned gases. The burned gas fraction is the mass fraction of gases in the cylinder that are neither fuel nor air. For a more detailed discussion on the definition of burned gas fraction, and how it differs from residual gas fraction, please refer Appendix A.

The blowdown process in internal combustion engines occurs just after the exhaust valve is opened. It refers to the rapid equalization of the pressures in the cylinder and in the exhaust runners at exhaust valve opening (u_{evo}). As seen in Fig. 2.1, the states T_{bd} and b_{bd} are defined after the blowdown process, at u_{evo}. The main control inputs are the exhaust valve closing timing (u_{evc}), start of fuel injection timing (u_{soi}), and mass of fuel injected (m_f^{inj}). Environmental conditions such as the pressure and temperature of the intake and exhaust manifolds affect the combustion, but these are not controlled. The performance outputs considered are combustion phasing (θ_{50}), work output (IMEP), and mass flows (m_{air} and λ).

The sample time for the discrete model is one engine cycle (720° CA). Each engine cycle ends at exhaust valve opening (EVO). The combustion top dead center (TDC) is considered to be the 0° CA location.

The dynamic evolution of the states can be broken down into two phases – the

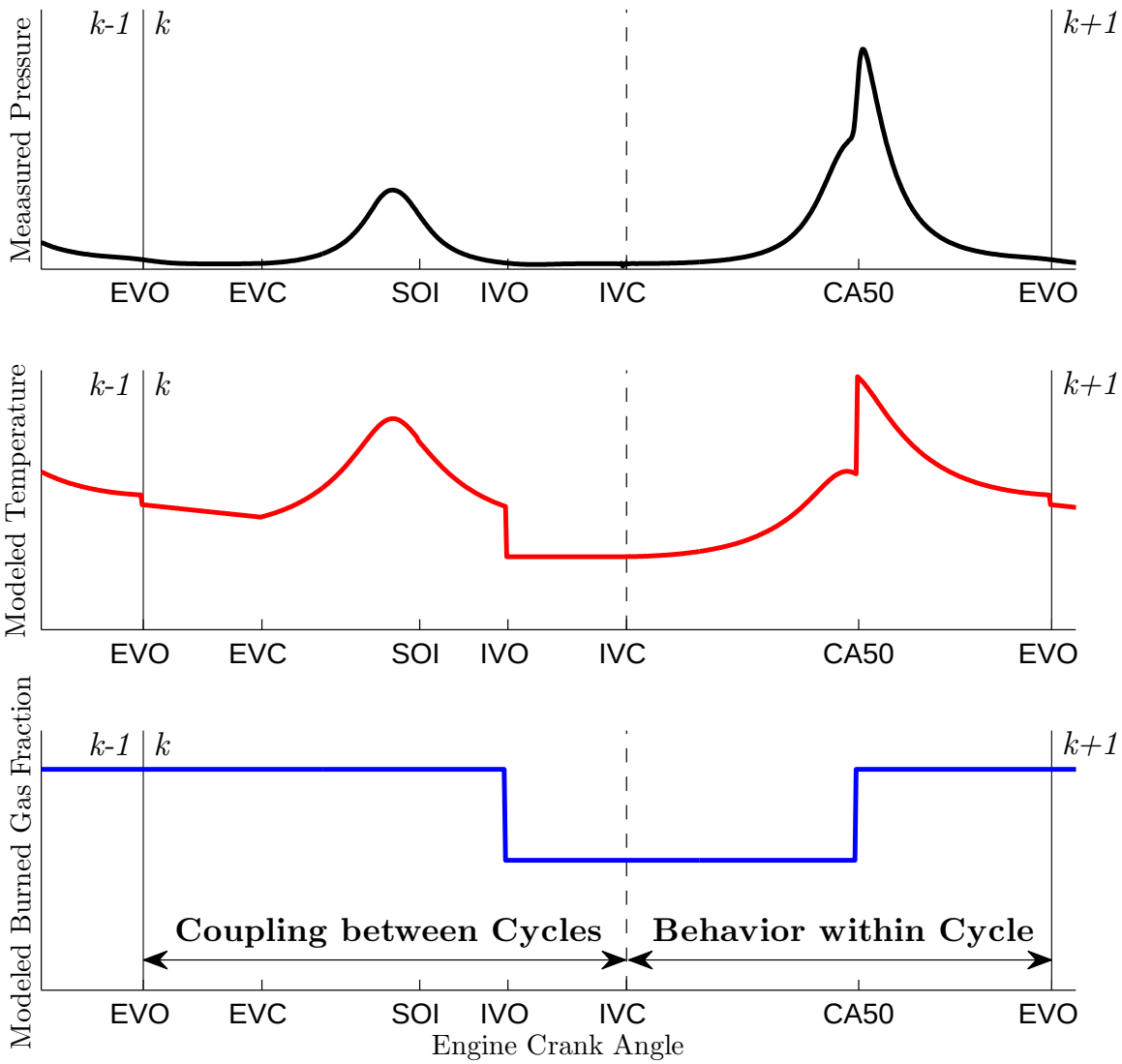

Figure 3.2: Evolution of the measured in-cylinder pressure, modeled charge temperature and modeled burned gas fraction. The thermal and composition coupling between cycles is modeled in the recompression region.

coupling between the cycles, and the the behavior within the cycle. An overview of this dynamic evolution is presented in Fig. 3.2. The model equations for these two phases are presented in Sec. 3.3 and 3.4.

3.3 Coupling between Cycles

This phase in the dynamic evolution of the states occurs between the exhaust valve opening (u_{evo}) and the intake valve closing (u_{ivc}) events. Both the intake and exhaust gas exchanges occur during this phase.

3.3.1 Trapping Residual Gas through Recompression

In recompression HCCI a large fraction of the in-cylinder charge is trapped before it can be exhausted. The hot residual gases retained between engine cycles have a significant impact on the temperature and composition of the in-cylinder charge of the subsequent cycle. This internal coupling between cycles is quantified by the residual gas fraction (x_r), which is defined as the mass fraction of the charge that is trapped during NVO, i.e.

$$x_r(k) = \frac{\text{Mass of residuals}}{\text{Mass of charge}} = \frac{m_{res}(k)}{m_c(k)}. \tag{3.1}$$

The residual gas fraction cannot be measured directly, but is estimated by pressure trace analysis to be very large in the current application, between 40% and 70%. Correctly predicting the amount, temperature, and composition of these residual gases is key to modeling the recompression HCCI process. For a given exhaust valve closing timing (u_{evc}), temperature of blowdown gases (T_{bd}), engine speed (ω), and pressure ratio across the engine (Π), the residual gas fraction is regressed as:

$$x_r(k) = 1 - (\alpha_0 + \alpha_1 u_{evc})\,\Pi^{\alpha_2} T_{bd}(k)^{\alpha_3} \omega(k)^{\alpha_4} \tag{3.2}$$
$$\text{where } \Pi = \frac{p_{im}(k)}{p_{em}(k)}.$$

Parameters $\alpha_{0,\ldots,4}$ are tuned to fit heat release analysis results.

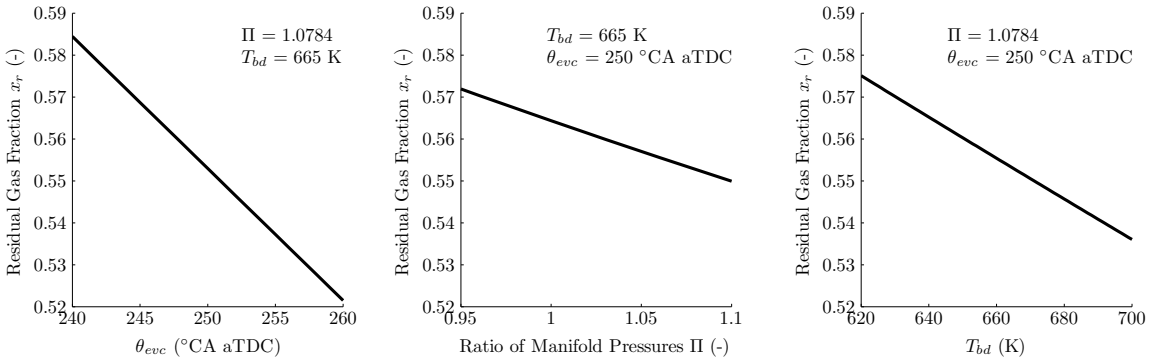

Figure 3.3: Residual gas fraction trends – three inputs (u_{evc}, Π, T_{bd}) to the x_r regression are swept, keeping all other inputs constant. Here $\Pi = \frac{p_{im}(k)}{p_{em}(k)}$. Validation results for the entire model are presented in Sec. 3.9.

Residual Gas Fraction Model Trends

The three sub-figures in Fig. 3.3 demonstrate typical x_r regression predictions for variations in the regression inputs. Three inputs (u_{evc}, Π, T_{bd}) to the regression are individually swept, keeping all other inputs constant. A later u_{evc} means a smaller negative valve overlap, and consequently in a smaller trapped residual fraction. An increased ratio of manifold pressures or higher blowdown temperatures lead to larger mass flows through the engine, or equivalently, in lower residual gas fractions. All three trends are physically intuitive.

Residual Gas Fraction Model Derivation

The x_r regression is an approximate form of the the orifice flow equation. The flow rate of ideal gases through an orifice with a ratio of orifice hole diameter to pipe diameter less that 0.25 for non-choked (subsonic) flow [60] is given by,

$$\dot{m} = CA_2P_1\sqrt{\frac{2M}{RT_1}\left(\frac{\gamma}{\gamma-1}\right)\left[\left(\frac{P_2}{P_1}\right)^{\frac{2}{\gamma}} - \left(\frac{P_2}{P_1}\right)^{\frac{\gamma+1}{\gamma}}\right]} \tag{3.3}$$

where

$\dot{m}$ = mass flow rate	C = orifice flow coefficient
A_2 = cross-sectional area of the orifice	γ = specific heat ratio (c_p/c_v)
P_1 = upsteam gas pressure	P_2 = downstream gas pressure
T_1 = upstream gas temperature	M = molecular mass.

The residual gas fraction can be related to the variable mass flow $\dot{m}$ through the exhaust valve, which is an orifice with a time-dependent cross-sectional area:

$$x_r = 1 - \frac{\int \dot{m}(t)\,\mathrm{dt}}{m_c}. \tag{3.4}$$

The variable mass flow can be rewritten as an averaged mass flow ($\dot{m}_{avg}$) through the exhaust valve that is constant over the valve open duration ($\Delta\theta$):

$$x_r = 1 - \frac{\dot{m}_{avg}\Delta t}{m_c} = 1 - \frac{\dot{m}_{avg}\Delta\theta}{\omega m_c}. \tag{3.5}$$

The averaged mass flow ($\dot{m}_{avg}$) through the exhaust valve is approximated using the orifice flow equation of Eq. (3.3). It is expressed as the mass flow through an averaged orifice cross-sectional area (A_{avg}), with averaged upstream and downstream pressures ($P_{1,avg}$ and $P_{2,avg}$), and an averaged upstream gas temperature ($T_{1,avg}$):

$$x_r = 1 - \frac{\Delta\theta C A_{avg}}{\omega V_{1,avg}} \sqrt{2MRT_{1,avg}\left(\frac{\gamma}{\gamma-1}\right)\left[\left(\frac{P_{2,avg}}{P_{1,avg}}\right)^{\frac{2}{\gamma}} - \left(\frac{P_{2,avg}}{P_{1,avg}}\right)^{\frac{\gamma+1}{\gamma}}\right]}. \tag{3.6}$$

Here the averaged upstream conditions are related to the temperature and pressure of the in-cylinder charge during the exhaust open period. The averaged downstream pressure is related to the exhaust manifold pressure.

A gross approximation of this rather complex equation can be arrived at by replacing the averaged upstream temperature during the exhaust process by a power of T_{bd}, the ratio of upstream and downstream pressures across the exhaust valve by a power of Π, and $\Delta\theta$ by a linear function of u_{evc}:

$$x_r \approx 1 - (\alpha_0 + \alpha_1 u_{evc})\,\Pi^{\alpha_2} T_{bd}(k)^{\alpha_3} \omega(k)^{\alpha_4}. \tag{3.7}$$

The model parameters are tuned using data, rather than being completely determined

by Eq.(3.6). The numerical values of the parameters are presented in Appendix B. This approximation works well for controls-oriented model development purposes.

3.3.2 Thermal Coupling

Sensitivity analysis suggests that temperature is the dominant factor in determining the start of combustion in HCCI combustion [24]. Thus modeling the thermal coupling between cycles is crucial in predicting combustion phasing.

After blowdown a portion of the charge exits the cylinder through the exhaust valve. The cooling of the rest of the charge between u_{evo} and u_{evc} is modeled by a scaling constant c_e. The trapped gases are polytropically compressed and expanded during the NVO region to obtain the residual gas temperature (T_{res}). Charge cooling due to the evaporation of the injected fuel (m_f^{inj}) can be modeled at the start of injection angle (u_{soi}):

$$T_{evc}(k) = c_e T_{bd}(k) \tag{3.8}$$

$$T_{soi}(k) = T_{evc}(k)\left(\frac{V_{evc}}{V_{soi}}\right)^{n-1} - \beta_0 m_f^{inj}(k) \tag{3.9}$$

$$T_{res}(k) = T_{soi}(k)\left(\frac{V_{soi}}{V_{ivo}}\right)^{n-1}, \tag{3.10}$$

where T_x and V_x are volumes and temperatures respectively at the specified engine event x. Model parameters c_e, β_0, and n are tuned using data.

The thermal mixing during the intake valve open period is modeled by an energy balance equation at u_{ivc}. The temperature of the hot residuals is assumed to be T_{res} while the rest of the charge is considered to be at the intake manifold temperature (T_{im}). Assuming constant specific heats, energy balance leads to:

$$T_{ivc}(k) = x_r(k) T_{res}(k) + (1 - x_r(k))\, T_{im}. \tag{3.11}$$

3.3.3 Composition Coupling

The burned gas fraction in the cylinder is modeled to change only during the combustion event, when the fuel combusts with a stoichiometric amount of air to form burned gases, or during the intake period, when the inducted air dilutes the mass fraction of the burned gases in the cylinder. Hence, the burned gas fraction can be at one of two levels – a value before (b_c) and after (b_{bd}) combustion. These are related

by assuming that an x_r portion of the burned gases is trapped between cycles:

$$b_c(k) = x_r(k) b_{bd}(k) \tag{3.12}$$

3.4 Behavior within the Cycle

This phase in the dynamic evolution of the states occurs between the intake valve closing (u_{ivc}) and the exhaust valve opening (u_{evo}) events. No gas exchange occurs during this phase. The in-cylinder charge is compressed, autoignition occurs, and the combusted gases are expanded.

3.4.1 In-cylinder Temperature

HCCI combustion is usually phased just after TDC, and heat release occurs fairly rapidly over a few crank angle degrees. Hence, the heat release is approximated as a constant volume process. The instantaneous heat release at θ_{50} occurs between a polytropic compression from u_{ivc} and a polytropic expansion to u_{evo}. In the equations below p_x, T_x, and V_x are pressures, volumes and temperatures respectively at the specified engine event x. In particular, V_{50} is the in-cylinder volume at θ_{50}. The charge temperature after combustion (T_{ac}) and the temperature rise due to combustion (ΔT) are given by:

$$T_{ac} = T_{ivc} \left(\frac{V_{ivc}}{V_{50}} \right)^{n-1} + \Delta T \tag{3.13}$$

$$\begin{aligned} \Delta T &= \eta_m(k) \frac{q_{lhv} m_f(k)}{c_v(k) m_c(k)} \\ &= \frac{\eta_m(k)\, q_{lhv} R}{c_v(k) p_{ivc} V_{ivc}} m_f(k) T_{ivc}(k). \end{aligned} \tag{3.14}$$

Here the polytropic exponent (n), lower heating value (q_{lhv}), and gas constant (R) are fixed constants. As seen in Fig. 3.4, the combustion efficiency (η_m) is roughly constant for most values of θ_{50}, and drops off sharply at late phasing conditions. The specific heat of combustion c_v varies as a function of composition (b_c) to capture variations in

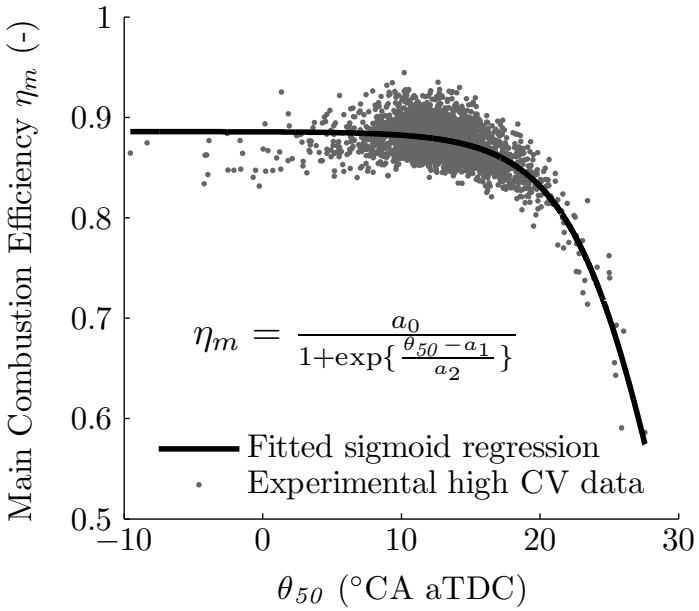

Figure 3.4: Combustion efficiency η_m is modeled as a function of θ_{50}, similar to [3]. Combustion efficiency drops off sharply at late phasing conditions. The values of η_m are obtained through heat release analysis. The quantity of unburned fuel is assumed to be negligible in this chapter.

mixture properties.

$$\eta_m(k) = \frac{\beta_1}{1+\exp\left\{\frac{\theta_{50}(k)-\beta_2}{\beta_3}\right\}}\left(\beta_4+\beta_5\omega(k)\right) \tag{3.15}$$

$$= \frac{0.89}{1+\exp\left\{\frac{\theta_{50}(k)-34.9}{4.9}\right\}}\left(\beta_4+\beta_5\omega(k)\right) \tag{3.16}$$

$$c_v(k) = 1+\beta_6 b_c(k) \tag{3.17}$$

The values of constants $\{\beta_1,\, \beta_2,\, \beta_3\} = \{0.89,\, 34.9,\, 4.9\}$ are obtained from experimental data, see Fig. 3.4. Parameters β_4, β_5 and β_6 are tuned to fit data. The effect of engine speed on heat transfer losses is lumped into combustion efficiency, as suggested by the model in [61].

Polytropic expansion after combustion and the ideal gas law give the temperature (T_{evo}) and the pressure (p_{evo}) of the charge at u_{evo} to be:

$$T_{evo}(k) = T_{ac}\left(\frac{V_{50}}{V_{evo}}\right)^{n-1} = T_{ivc}(k)\left(\frac{V_{ivc}}{V_{evo}}\right)^{n-1}\left[1+\frac{\eta_m\, q_{lhv} R {V_{50}}^{n-1}}{c_v p_{ivc} {V_{ivc}}^{n}} m_f(k)\right] \tag{3.18}$$

$$p_{evo}(k) = p_{ivc}(k)\frac{V_{ivc}}{V_{evo}}\frac{T_{evo}(k)}{T_{ivc}(k)}. \tag{3.19}$$

Expansion is followed by the blowdown process, which is modeled as a polytropic expansion from p_{evo} to the exhaust manifold pressure (p_{em}), with the polytropic exponent n. The temperature at blowdown (T_{bd}) of the next engine cycle is:

$$\begin{aligned} T_{bd}(k+1) &= T_{evo}(k) \left(\frac{p_{evo}}{p_{em}} \right)^{\frac{1-n}{n}} \\ &= T_{ivc}(k) \left(\frac{p_{ivc}(k)}{p_{em}} \right)^{\frac{1-n}{n}} \left[1 + \frac{\eta_m \, q_{lhv} R {V_{50}}^{n-1}}{c_v p_{ivc} {V_{ivc}}^n} m_f(k) \right]^{\frac{1}{n}}. \end{aligned} \tag{3.20}$$

3.4.2 In-cylinder Composition

Between u_{ivc} and u_{evo}, the in-cylinder composition is modeled to change only during combustion. During the combustion event, the fuel combines with a stoichiometric mass of air to form an equivalent mass of burned gases. The burned gas fraction before (b_c) and after (b_{bd}) combustion are related by the following algebraic relations:

$$\begin{aligned} b_{bd}(k+1) &= \frac{(\, AFR_s + 1)\, m_f^{inj}(k)}{m_c(k)} + b_c(k) \\ &= \frac{(\, AFR_s + 1)\, R}{p_{ivc} V_{ivc}} T_{ivc}(k) m_f^{inj}(k) + b_c(k). \end{aligned} \tag{3.21}$$

Here the stoichiometric air-fuel ratio ($\, AFR_s$) is a fixed constant. Also note that Eq. 3.21 assumes complete combustion of the fuel in the cylinder. This is a good assumption in the high efficiency region of HCCI combustion. In general one wishes to maintain the in-cylinder combustion in this region for best fuel economy and stability. It will be seen later in Chap. 5 that the model fidelity is improved if this assumption is relaxed in certain low efficiency regions of HCCI combustion.

3.5 Combustion Phasing

Combustion phasing, quantified by θ_{50}, is the primary performance output of the model. It needs to be carefully predicted and controlled within fixed bounds. Early combustion causes excessive pressure rise rates that mechanically stress the engine, and violate ringing and noise constraints. Late combustion leads to incomplete combustion and significant amounts of unburned fuel being carried from cycle to cycle. The resulting cyclic variability and torque fluctuations can be unacceptably high.

3.5.1 Autoignition Modeling in Literature

Autoignition in HCCI combustion can be modeled in a number of ways, with varying degrees of complexity and fidelity [51, 62]. The autoignition of gasoline is driven by complex chemical kinetics that are affected by the temperature, pressure, concentration and stratification of the in-cylinder mixture. Detailed chemical reaction mechanisms have been developed in literature that consist of thousands of intermediate chemical species and reactions, see for example [63] with 857 species and 3606 reactions. These computationally complex and slow reaction mechanisms are unsuitable for controller development. The Shell model [52] is a simpler alternative used in some higher-fidelity combustion models, see for example [51]. This model uses five representative species in a set of chemical reaction rate and energy balance differential equations.

The correlation for combustion used in this work is the integrated Arrhenius rate threshold model. The combustion of the hydrocarbon fuel is approximated as a single-step global reaction with an Arrhenius-type reaction rate [64]. The model is similar in form to the integral threshold method used to predict SI engine knock, which has been studied for over half a century. Livengood and Wu [65] discuss the concept of a critical concentration providing the limit for an integration process during which the concentration of reaction radicals builds up. This integration process is expressed in terms of the reaction rate, or the related ignition delay time τ, in the following manner:

$$\frac{(x)}{(x)_c} = \int_{t=0}^{t=t_e} \frac{1}{\tau}\,\mathrm{dt} = 1.0 \tag{3.22}$$

where ${}^{(x)}/_{(x)_c}$ is the relative concentration ratio, τ is the ignition delay time, and t_e is the predicted time of autoignition or knock.

Several different functional forms of the ignition delay τ are used in literature. Often these expressions are only valid for limited ranges of temperatures, pressures and compositions. Examples of these forms include Eq. (3.23) proposed by Livengood and Wu [65], which is dependent only on pressures, temperatures and empirical constants. He et al. [66] examined the autoignition of iso-octane using a rapid compression facility. The functional form of the expression proposed, see Eq. (3.24), includes concentration terms and works over a range of typical HCCI-like conditions. Shaver et al. [67] propose Eq. (3.24), an alternate functional form for the ignition delay that

also considers molar concentrations of the fuel and oxygen species.

$$\tau_{Livengood} = ce^{(b/T)p^n} \tag{3.23}$$

$$\tau_{He} = Ap^{n_p}\phi^{n_\phi}\chi_{O_2}^{n_{\chi_{O_2}}}e^{(b/T)} \tag{3.24}$$

$$\tau_{Shaver} = AT^{n_T}[C_3H_8]^{n_f}[O_2]^{n_O}e^{(b/T)} \tag{3.25}$$

where τ is the ignition delay, T is the mixture temperature, p is the mixture pressure, ϕ is the equivalence ratio, $\chi_\cdot$ is mole percent, $[\cdot]$ is molar concentration, and the remaining variables are empirical constants.

Standard values of the empirical constants for various fuels are presented in literature, for example [64]. These parameters have to be tuned to match data.

3.5.2 Arrhenius Rate Threshold Model

A version of the integrated Arrhenius rate threshold model of Eq. (3.22) is used in this work. The start of combustion (θ_{soc}) is given by the global Arrhenius integral of Eq. (3.26). All intermediate HCCI combustion reactions are aggregated into a single Arrhenius-type integral with a fixed activation temperature ($B = \frac{E_a}{R_u}$) and pre-exponential factor (A). The integration is carried out until the threshold (K_{th}) is hit at θ_{soc}. This Arrhenius threshold is modeled as a function of u_{soi}. Injecting earlier in the recompression region preceding combustion reduces the integration threshold. The model can be expressed as follows:

$$K_{th}(u_{soi}) = \int_{u_{ivc}}^{\theta_{soc}} \frac{A}{\omega} p_c(\theta)^{n_p} \exp\left(\frac{B}{T_c(\theta)}\right) \mathrm{d}\theta \tag{3.26}$$

$$K_{th}(u_{soi}) = k_0 - u_{soi} \tag{3.27}$$

where ω is the engine speed. The pressure (p_c) and temperature (T_c) of the charge in the cylinder are given by a polytropic compression with a polytropic exponent n:

$$p_c(\theta) = p_{ivc}\left(\frac{V_{ivc}}{V(\theta)}\right)^n, \quad T_c(\theta) = T_{ivc}\left(\frac{V_{ivc}}{V(\theta)}\right)^{n-1}. \tag{3.28}$$

In this work θ_{soc} is considered to be θ_{02}, the engine crank angle at which 2% of the total heat release occurs. The output θ_{50} is modeled as a linear function of θ_{soc}:

$$\theta_{50} = b_1\theta_{soc} + b_0. \tag{3.29}$$

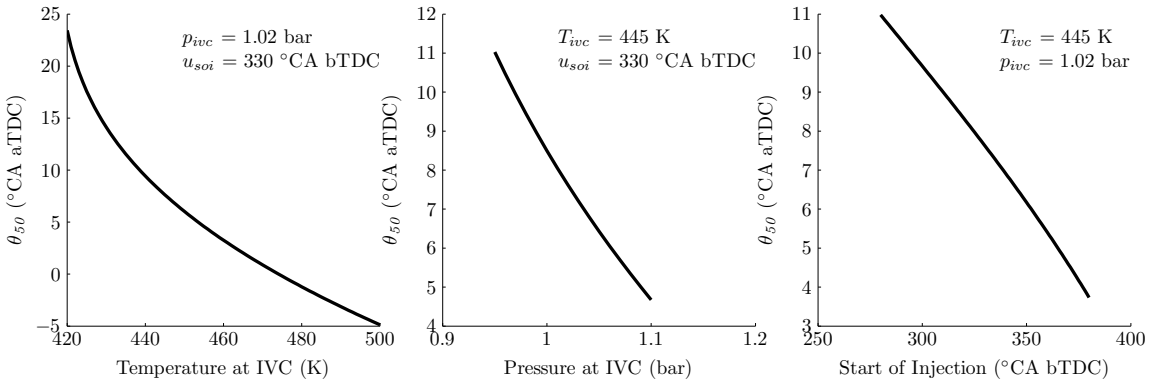

Figure 3.5: Arrhenius regression trends – three inputs (T_{ivc}, p_{ivc}, u_{soi}) to the Arrhenius integral are swept, keeping all other inputs constant. Validation results for the entire model are presented in Sec. 3.9.

Combustion Model Trends

The three sub-figures in Fig. 3.5 demonstrate typical Arrhenius integral predictions for variations in regression inputs. Three inputs (T_{ivc}, p_{ivc}, u_{soi}) to the Arrhenius integral are individually swept, keeping all other inputs constant.

The first sub-figure of Fig. 3.5 demonstrates that the combustion phasing θ_{50} is significantly affected by relatively small changes in temperature. This agrees with previous work postulating that HCCI combustion is thermally-driven [24]. The sensitivity of θ_{50} to T_{ivc} increases at lower temperatures and later combustion phasings.

In the second sub-figure of Fig. 3.5, the Arrhenius integral model predicts that higher intake pressures lead to earlier combustion phasing, if T_{ivc} were kept constant. This follows intuitively, as increased pressure should facilitate faster chemical reactions. However, this is the opposite trend to what is seen in experiments, and to what is predicted by the full nonlinear model with temperature dynamics (see Fig. 3.6). An increased intake manifold pressure results in more air flow through the cylinder, and consequently a lower T_{ivc}. This lowered T_{ivc} dominates the effect of increased p_{im} on the Arrhenius model, and phases combustion later.

The chemical effect of u_{soi} on combustion phasing is modeled by a lowered integration threshold K_{th} in Eq. (3.26). Physically this means that an earlier u_{soi} lowers the critical concentration threshold for autoignition in the global Arrhenius reaction. As seen in the final sub-figure of Fig. 3.5, an earlier u_{soi} causes an earlier auto-ignition.

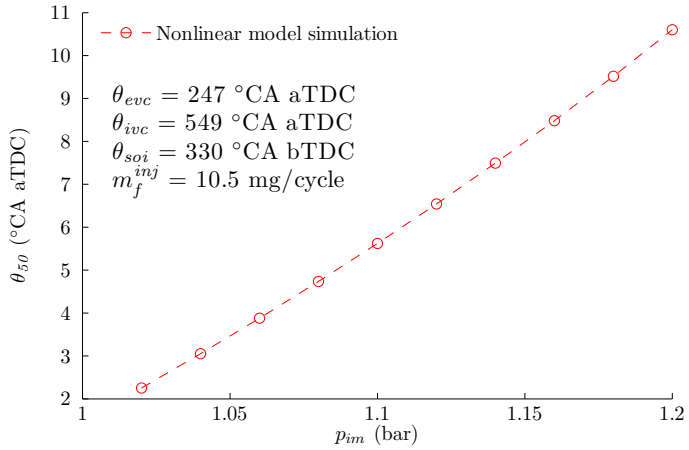

Figure 3.6: Nonlinear model predictions – augmenting the Arrhenius integral with thermal dynamics correct predicts later θ_{50} for increased p_{im}.

3.6 Cycle-averaged Mass Flows

In typical spark-ignition gasoline engines, the air-fuel equivalence ratio λ is regulated to unity to maintain emissions catalyst conversion efficiency. Since HCCI combustion is lean and NO_x conversion is not an issue, λ is typically greater than 1. However this means that there is a difference between the lambda that is measured outside the engine (λ_m) and the lambda actually in the cylinder (λ_c). The trapped residual gases contain air that does not leave the cylinder, and is subsequently not measured by the lambda sensors in the exhaust. Indeed, $\lambda_m \leq \lambda_c$.

The mass of air that is inducted in the cylinder (m_{air}^{meas}), and that is actually in the cylinder (m_{air}) are determined by considering the appropriate fractions of the total mass of charge. Here the mass of charge (m_c) is determined by the ideal gas law:

$$m_{air} = (1 - b_c)\, m_c - m_f \tag{3.30}$$

$$m_{air}^{meas} = (1 - x_r)\, m_c - m_f \tag{3.31}$$

$$m_c = \frac{p_{ivc} V_{ivc}}{R T_{ivc}}. \tag{3.32}$$

Finally the air-fuel equivalence ratios are given by,

$$\lambda_c = \frac{1}{AFR_s} \cdot \frac{m_{air}}{m_f} = \frac{1}{AFR_s} \cdot \left[(1 - b_c) \frac{m_c}{m_f} - 1 \right] \tag{3.33}$$

$$\lambda_m = \frac{1}{AFR_s} \cdot \frac{m_{air}^{meas}}{m_f} = \frac{1}{AFR_s} \cdot \left[(1 - x_r) \frac{m_c}{m_f} - 1 \right] \tag{3.34}$$

As can be seen from Eq. (3.33) and (3.34), $\lambda_m < \lambda_c$ as $x_r > b_c$ for lean combustion.

3.7 Summary of Model Equations

The nonlinear two-state HCCI combustion model state update equations can be summarized as follows:

$$\begin{aligned} T_{bd}(k+1) &= \left(\frac{p_{ivc}}{p_{em}}\right)^{\frac{1-n}{n}} \left[1 + \frac{\eta_m \, q_{lhv} Rm_f^{inj}}{c_v p_{ivc} V_{ivc}} \left(\frac{V_{50}}{V_{ivc}}\right)^{n-1}\right]^{\frac{1}{n}} T_{ivc} \\ b_{bd}(k+1) &= \frac{(\,AFR_s + 1)\, Rm_f^{inj}}{p_{ivc} V_{ivc}} T_{ivc} + x_r b_{bd}(k). \end{aligned} \tag{3.35}$$

Here the residual gas fraction (x_r), the specific heat (c_v), the combustion efficiency (η_m) and the temperature at IVC (T_{ivc}) are given by:

$$x_r = 1 - (\alpha_0 + \alpha_1 u_{evc}) \left(\frac{p_{im}}{p_{em}}\right)^{\alpha_2} \omega^{\alpha_4} T_{bd}(k)^{\alpha_3} \tag{3.36}$$

$$c_v = 1 + \beta_5 x_r b_{bd}(k) \tag{3.37}$$

$$\eta_m(k) = \frac{\beta_1}{1 + \exp\left\{\frac{\theta_{50}(k) - \beta_2}{\beta_3}\right\}} (1 + \beta_4 \omega(k)) \tag{3.38}$$

$$T_{ivc} = x_r c_e \left(\frac{V_{evc}}{V_{ivc}}\right)^{n-1} T_{bd}(k) + (1 - x_r)\, T_{im}. \tag{3.39}$$

The combustion phasing output is obtained by solving the Arrhenius type integral:

$$K_{th}(u_{soi}) = k_0 - u_{soi} = \int_{u_{ivc}}^{\theta_{soc}} \frac{A}{\omega} p_c(\theta)^{n_p} \exp\left(\frac{B}{T_c\,(\theta)}\right) \mathrm{d}\theta \tag{3.40}$$

$$\theta_{50} = \gamma_1 \theta_{soc} + \gamma_0. \tag{3.41}$$

Here model parameters $k_0, n_p, A, B, c_e, \alpha_i, \beta_j$, and γ_k ($i \in \{0, \ldots, 4\}$, $j \in \{1, \ldots, 5\}$, $k \in \{0, 1\}$) are tuned using steady state experimental data. The numerical values of the parameters are provided in Appendix B.

Quantity	Nominal point	Quantity	Nominal point
u_{evc}	254 °CA aTDC	T_{bd}	813 K
m_f^{inj}	10.8 mg/cycle	b_{bd}	0.80
u_{soi}	330 °CA bTDC	p_{im}	1.1 bar
θ_{50}	6.03 °CA aTDC	p_{em}	1.01 bar
ω	1800 rpm		

Table 3.1: Linearization operation point

3.8 Linearized Model

The nonlinear system of equations given by Eq. (3.1) to (3.34) is linearized about the nominal operating point specified in Table 3.1. The linearization point was chosen to be a typical HCCI operating point at a nominal engine speed (1800 rpm). The specific values of the inputs (m_f^{inj}, u_{soi}, u_{evc}) and the outputs (θ_{50} and IMEP) were chosen to be approximately in the middle of their observed usable ranges. The actuator settings were reasonably far away from the saturation constraints, and θ_{50} was chosen to be away from both the ringing and the high variability regions. This linearized model is used to develop the model-based feedforward controller and the state observer.

$$\begin{aligned} x(k+1) &= Ax(k) + \begin{bmatrix} B_{evc} & B_f & B_\omega & B_{soi} \end{bmatrix} u(k) \\ \theta_{50}(k) &= Cx(k) + \begin{bmatrix} D_{evc} & D_f & D_\omega & D_{soi} \end{bmatrix} u(k) \\ u(k) &= \begin{bmatrix} u_{evc}(k) & m_f^{inj}(k) & \omega(k) & u_{soi}(k) \end{bmatrix}^T \\ x(k) &= \begin{bmatrix} T_{bd}(k) & b_{bd}(k) \end{bmatrix}^T \end{aligned} \tag{3.42}$$

where

$$\begin{aligned} A &= \begin{bmatrix} 0.467 & -210.4 \\ -2.21 \times 10^{-4} & 0.475 \end{bmatrix} \\ B &= \begin{bmatrix} -1.11 & 31.1 & 0.0676 & -0.212 \\ -.004 & 0.039 & 7.86 \times 10^{-5} & 0 \end{bmatrix} \\ C &= \begin{bmatrix} -0.0887, 0 \end{bmatrix}, \; D = \begin{bmatrix} 0.72, 0, 4.77 \times 10^{-4}, -0.204 \end{bmatrix} \end{aligned} \tag{3.43}$$

For the chosen linearization point, both discrete eigenvalues of the model are stable and lie on the positive real axis within the unit circle (0.69 and 0.26). The location of

these eigenvalues move for different choices of the linearization point.

3.9 Model Validation Results

Model coefficients were determined using a least squares optimization process. Data to parameterize the control-oriented model was taken from the experimental setup described in Chap. 2. In-cylinder pressure was sampled at a resolution of 0.1 °CA. Three hundred engine cycles were recorded at each steady state operating point, and heat release analysis was performed on the mean pressure trace[1]. The analysis tool estimates the mass fraction burned curve, the work output, the in-cylinder temperature trace, the residual gas fraction and the cylinder mass flows. The control-oriented model predictions were compared to these results. Details of the offline heat release analysis method can be found in [6, 45, 68]. Validation results will be presented here for engine speeds between 1600 rpm to 2100 rpm, and engine loads between 2.5 bar to 3.2 bar. However the model is shown to work over a larger operating range, as seen in the model-based control results of Chap. 4 and Chap. 6.

3.9.1 Steady State Parameterization

Steady state parameterization results for various actuator sweeps are presented in Fig. 3.7 and Fig. 3.8. In these figures, data and model predictions of three performance outputs (θ_{50}, IMEP, and m_{air}) are compared for sweeps in four actuators (u_{evc}, u_{soi}, m_f^{inj}, and ω). Each column represents experiments in which a single actuator was varied, keeping the values of other actuators constant. Two u_{evc} sweeps at different fueling levels are presented. The most important output, combustion phasing θ_{50}, is plotted in the top row.

The θ_{50} trends are predicted well for all four actuator sweeps. For the overall dataset, θ_{50} is predicted with an RMS error of 0.48 °CA by the nonlinear model, which is considered to be good performance. The model satisfactorily predicts the other performance outputs, m_{air} and IMEP. The largest error in trend is observed for IMEP predictions at early injection timings. Injecting early in the NVO region increases pumping work and reduces IMEP. In the interest of reducing model parameters, this effect is not captured in the model. This does not affect the performance of the model for developing combustion phasing controllers.

[1]The author would like to thank J. Larimore (`larimore@umich.edu`) for the heat release analysis.

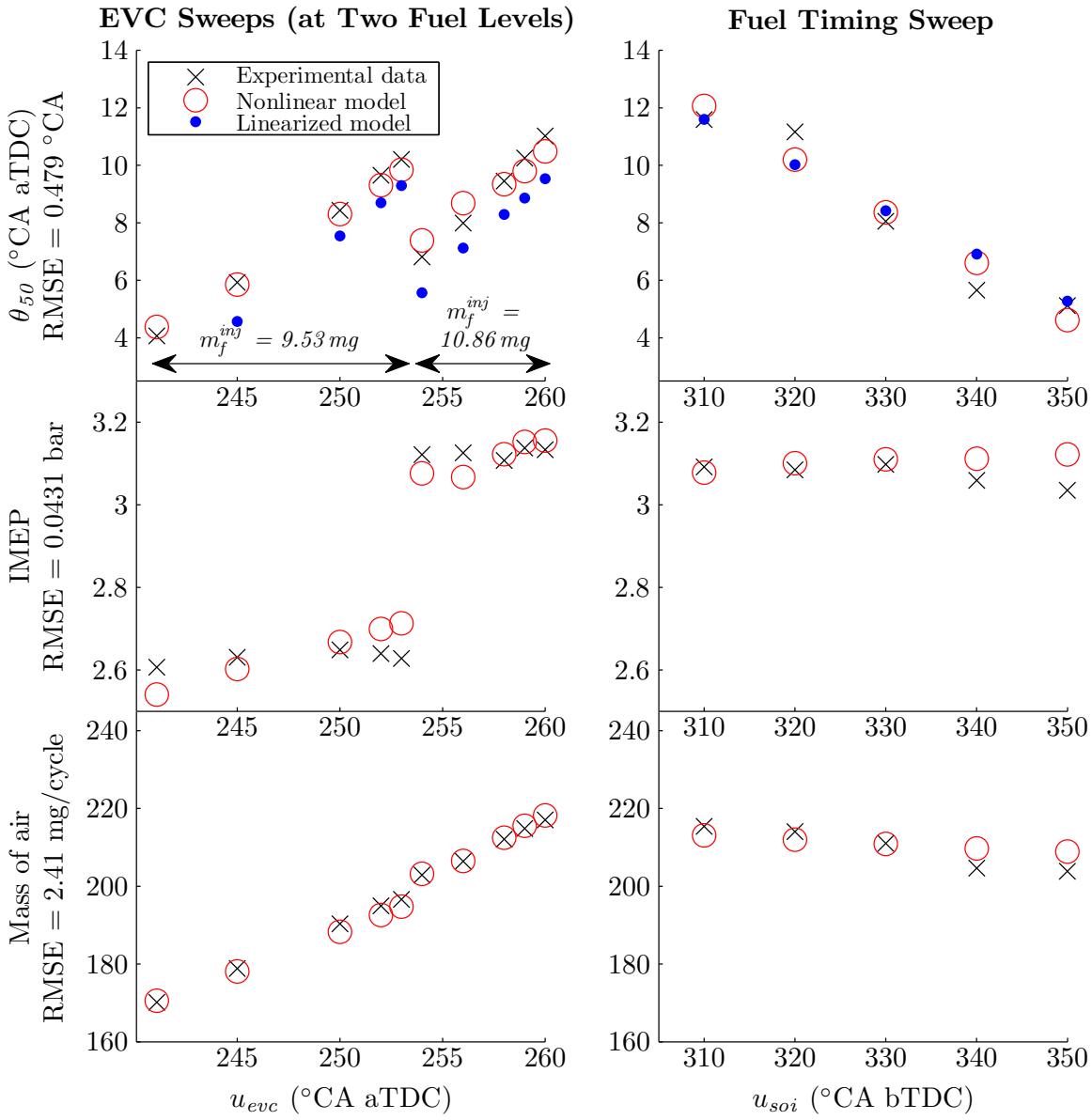

Figure 3.7: Steady state parameterization results of three performance outputs (θ_{50}, IMEP, and m_{air}) for sweeps in two actuators (u_{evc} and u_{soi}). Root mean square error (RMSE) values are presented for the nonlinear model predictions.

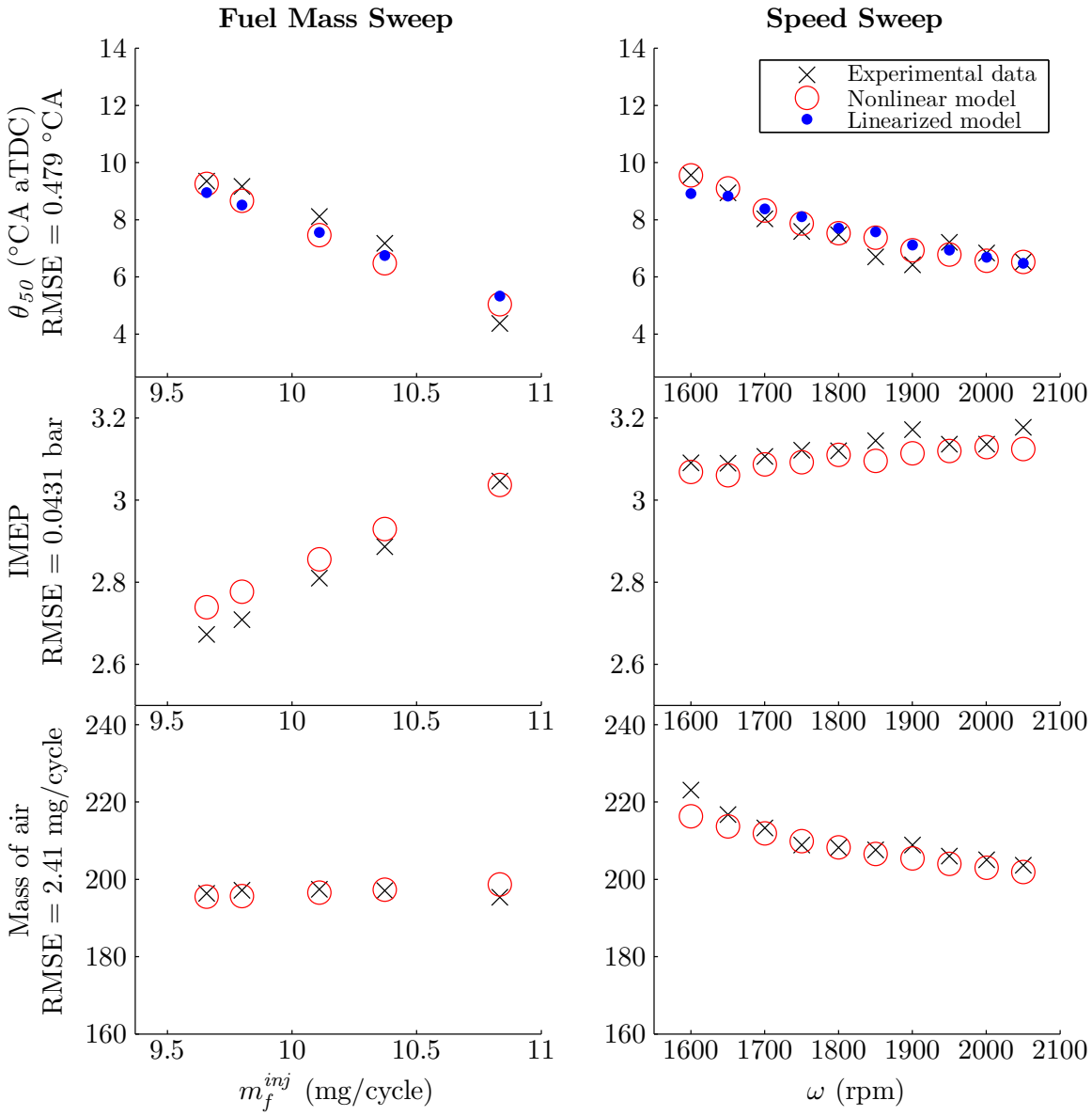

Figure 3.8: Steady state parameterization results of three performance outputs (θ_{50}, IMEP, and m_{air}) for sweeps in two actuators (m_f^{inj} and ω). Root mean square error (RMSE) values are presented for the nonlinear model predictions.

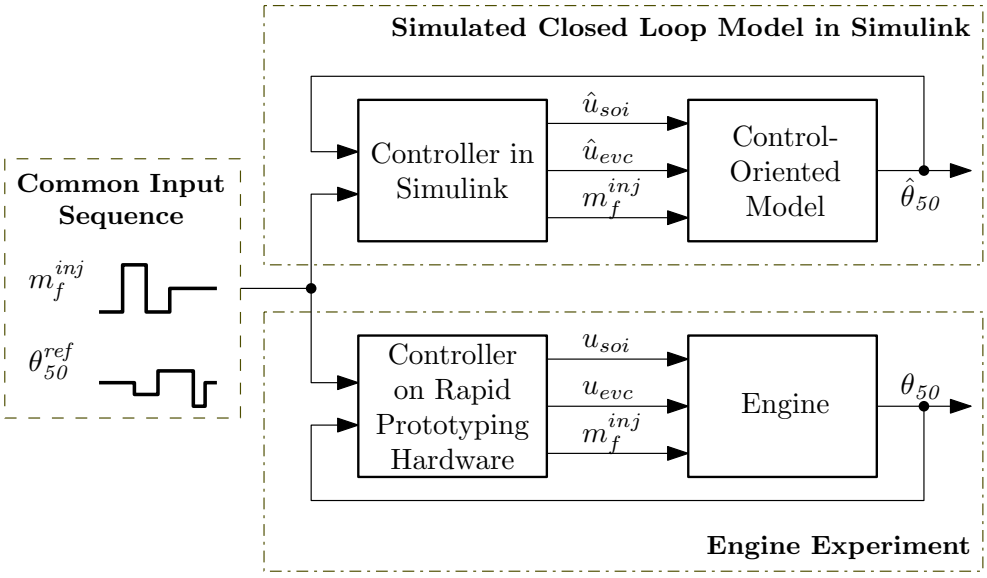

Figure 3.9: Transient validation setup – identical desired load and θ_{50}^{ref} steps are fed to the closed-loop model and the engine. The predicted and measured θ_{50}, u_{soi}, and u_{evc} traces are compared.

Steady state validation results for the θ_{50} output are presented for the linearized model as well. This variant of the nonlinear model is seen to predict actuator trends well. The errors in predicting absolute magnitudes of θ_{50} are attributed to linearization error caused when the engine operates at points outside the immediate neighborhood of the nominal operating point.

3.9.2 Transient Validation

The accuracy of the fuel governor control strategy presented in Chap. 4 depends on the control-oriented model correctly predicting the dynamic behavior of the engine. The setup outlined in Fig. 3.9 was used to test the model's closed-loop transient behavior. A mid-ranging feedback controller, see Sec. 4.1, was implemented both in simulation and on the rapid prototyping hardware. Identical desired load and θ_{50}^{ref} input steps were fed to both the model and the engine. Since constraints on future predicted actuator trajectories are used in the fuel governor control strategy, it is important to verify the transient validity of both the simulated actuator and output trajectories. The predicted θ_{50}, u_{evc} and u_{soi} traces were compared to engine measurements.

The results of this test, shown in Fig. 3.10, demonstrate satisfactory closed loop model validation of the model. These plots compare experimental transient results with model predictions. The predicted θ_{50} and u_{soi} traces match both the magnitude

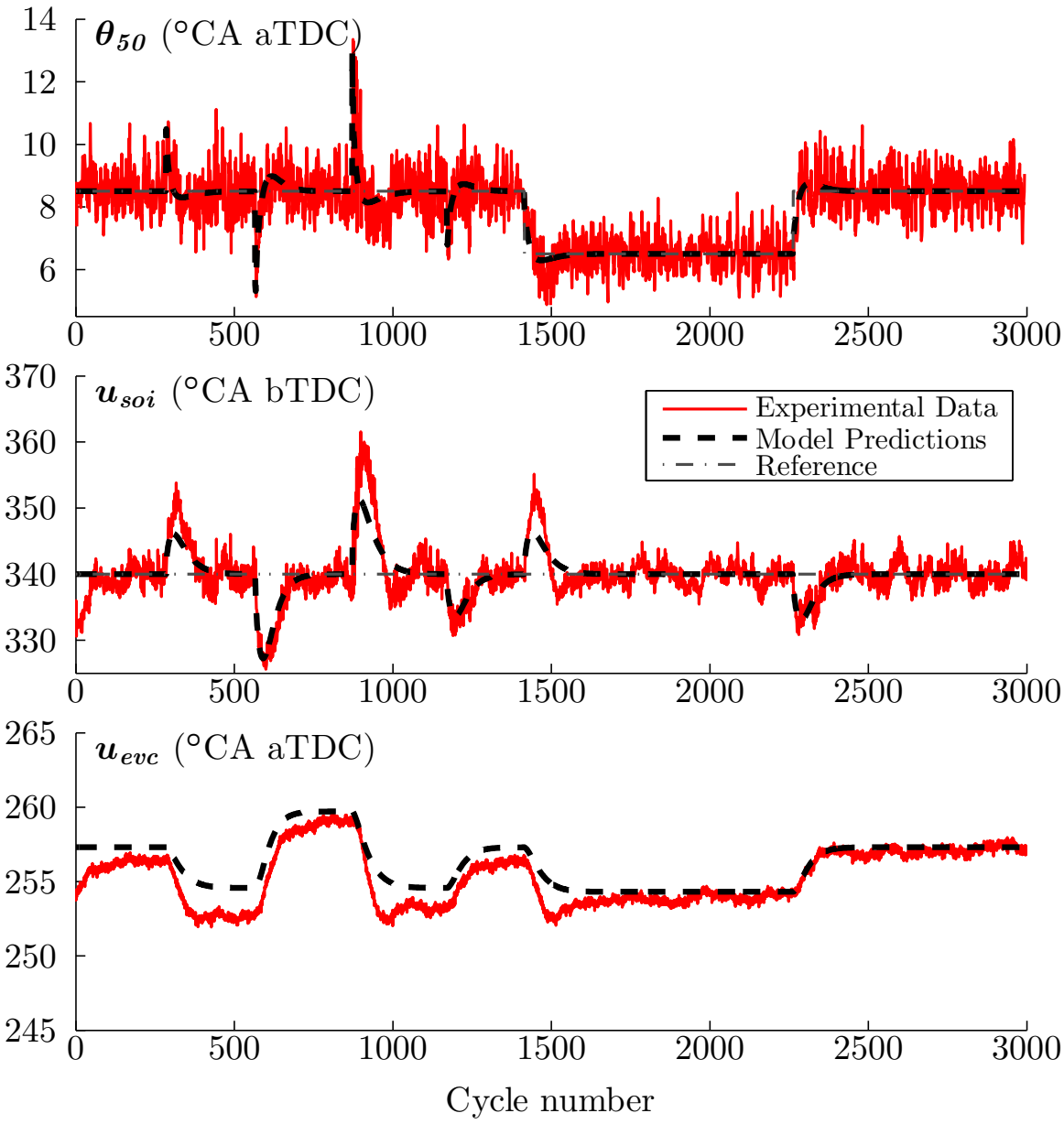

Figure 3.10: Transient validation of model – identical desired load and θ_{50}^{ref} steps are fed to the model and the engine, as in Fig. 3.9. The model correctly predicts the magnitude and dynamic behavior of the engine measurements.

and dynamic behavior of the engine measurements. These closed loop validation results support the use of this model for predictive model-based control.

The offset seen in the u_{evc} predictions in Fig. 3.10 is attributed to several months of engine ageing, and to unmodeled environmental factors. For example the coolant temperatures for the parameterization dataset and the experiments are different. Also, the feedback structure of the controller assigns any error in model prediction to u_{evc}. In spite of this offset, the dynamic behavior of the engine u_{evc} is reproduced correctly.

3.10 Summary

This chapter presents a low-order control-oriented model for recompression HCCI combustion. The coupling between cycles introduced through the retention of exhaust gases in the recompression region is modeled using discrete thermal and composition states. The steady-state and transient effects of actuators such as exhaust valve timing, fuel injection mass and timing, and engine speed on outputs such as combustion phasing and IMEP are validated. The validated nonlinear and linearized models are used for controller development in Chap. 4 and Chap. 6.

This model is developed for operating regimes with low variability and near complete combustion. In general it is desired that combustion be maintained in these regions for driveability and fuel economy. Experiments show that reducing x_r (for example by phasing u_{evc} later) results in later combustion phasing θ_{50}, and in the onset of oscillatory dynamics leading to significant cyclic variability (CV) [5, 45]. Chapter 5 focuses on correctly predicting both the onset and nature of this variability through an additional chemical coupling state introduced by the combustion of unburned fuel in the NVO region.

Chapter 4

Reference Governor Control of HCCI Load Transitions

This chapter presents the first of two HCCI combustion control strategies discussed in this dissertation. The proposed control strategy aims to regulate combustion phasing during HCCI load transitions, which is of specific concern as the phasing is constrained within a narrow acceptable range [6, 7]. Early combustion causes excessive pressure rise rates that violate noise and mechanical stress constraints. Late phasing leads to incomplete combustion, significant amounts of unburned fuel being retained between cycles, and unacceptably high cyclic variability and torque fluctuations.

Further, the transient response during load transitions in HCCI engines can violate the acceptable combustion phasing range, even if the steady state operating points lie within this range. This occurs as auto-ignition timing control in HCCI combustion requires careful regulation of the pre-combustion cylinder charge properties, and is especially sensitive to temperature changes [24]. Load transitions are primarily achieved through fuel mass changes, which have a significant effect on charge temperature. Further, combustion phasing regulation during large transients can lead to actuator saturation, and a subsequent loss in controller authority and regulation performance. This is most pronounced during load steps down, when reduced charge temperatures can cause excessively late combustion phasing and engine misfires. Misfires are unacceptable for emissions and driveability.

Figure 4.1 presents an overview of the proposed control strategy, which consists of a baseline controller augmented with a reference or fuel governor. The baseline controller is adapted from literature, and is a feedback-feedforward controller that uses u_{soi} and u_{evc} to regulate θ_{50} to a desired value (θ_{50}^{ref}). The desired mass of fuel to be injected (m_f^{des}) is computed as a static function of the desired engine load. The fuel governor is added on to the closed loop system and modifies the transient trajectory of the m_f^{inj} signal. The governor is used to improve the combustion phasing regulation

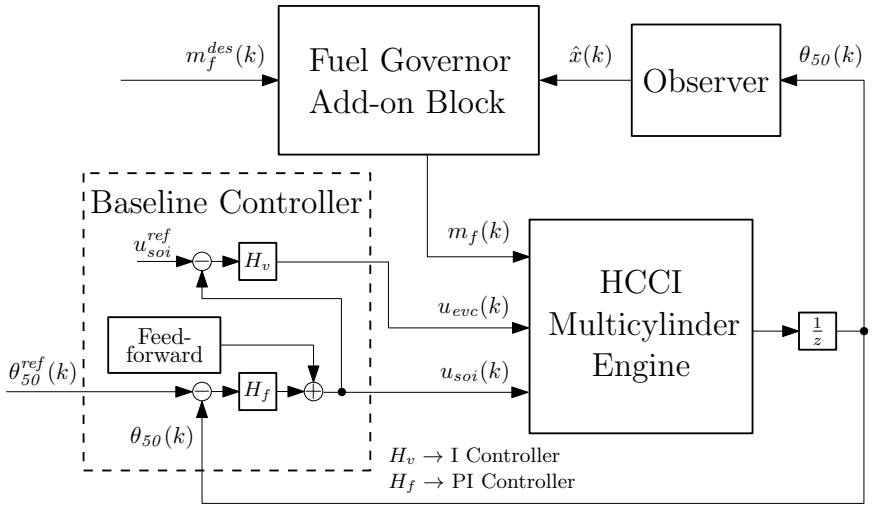

Figure 4.1: Reference governor control strategy overview – the reference or fuel governor is added on to the controller-augmented system. Estimated system states are obtained from the observer.

performance of the baseline controller during load transitions in the HCCI operating region. The governor is inactive at steady-state conditions.

The baseline controller is introduced in Sec. 4.1 and is shown to work well during small load transitions, but is shown to exhibit unsatisfactory transient performance during larger load transitions. To solve this problem a fuel governor add-on block is designed in Sec. 4.2. The governor modifies the transient m_f^{inj} command during large load transitions, when the possibility of future actuator constraint violations exists. This is shown to improve the combustion phasing and load responses. Three variants of the fuel governor are presented, each with differing complexity and fidelity. Experimental validation of these strategies are presented in Sec. 4.3. Finally, experimental runtime issues are considered in Sec. 4.4, and the fuel governor discussion is summarized in Sec. 4.5.

4.1 Baseline Controller

The baseline controller from Fig. 4.1 is presented in more detail in Fig. 4.2. The two performance outputs of the system are the engine load (IMEP) and the combustion phasing (θ_{50}). The engine load is primarily controlled by the mass of fuel injected (m_f^{inj}) in the cylinder. For a load transition m_f^{inj} is assumed to be externally specified, and is considered to be a disturbance for the baseline combustion phasing controller. The baseline controller regulates θ_{50} to a reference combustion phasing set-point (θ_{50}^{ref}),

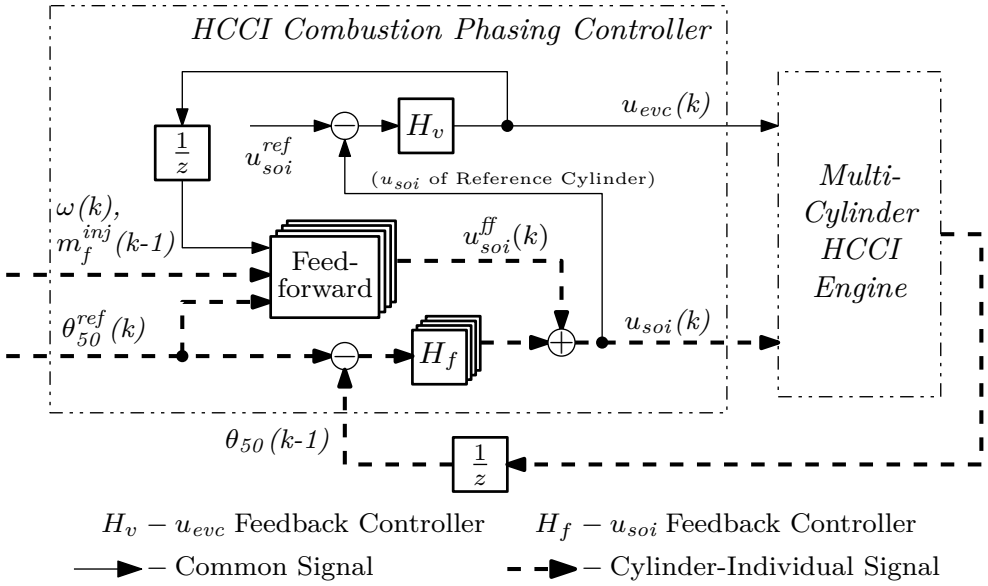

Figure 4.2: Baseline controller – two controlled inputs u_{soi} and u_{evc} in a mid-ranging feedback configuration, with a model-based feedforward for u_{soi}.

typically chosen to maximize fuel efficiency. This set-point is either determined offline, or is provided by a supervisory controller. Hence the baseline controller design problem reduces to using u_{soi} (four values, one for each cylinder) and u_{evc} (a single value for the engine) to regulate θ_{50} during a m_f^{inj} transition. The baseline controller comprises of a feedback loop and a model-based feedforward component of u_{soi}.

4.1.1 Feedback

The feedback loop consists of two PI controllers arranged in a mid-ranging control configuration, see Fig. 4.2. Mid-ranging is a control allocation strategy used in process control [69], and is used to allocate control actions between two actuators with different bandwidths. It has been used in HCCI engine control applications in literature, see for example [34, 70]. This configuration is useful when one actuator provides the required range but is slow, while the other actuator is fast but saturates easily. To provide high resolution over the entire operating range, the slow actuator returns the fast actuator to its reference set point at steady state.

In the current application, the u_{evc} and u_{soi} actuators act as the slow and the fast actuators respectively. The u_{evc} actuator has the larger range and greater authority, in terms of affecting θ_{50}. However, the hydraulic cam phasing actuator is relatively slow, and has a common value for all cylinders. In contrast, the effect of u_{soi} on θ_{50}

saturates easily, but u_{soi} can be set independently from cycle-to-cycle for each cylinder. The θ_{50} tracking error signal drives a PI controller (H_f in Fig. 4.2) that controls u_{soi}. The slower u_{evc} moves or mid-ranges u_{soi} back towards its reference set point. This is accomplished using a slow integral controller (H_v in Fig. 4.2) driven by the u_{soi} tracking error for a fixed reference cylinder, here cylinder 1.

Note that in a multi-cylinder engine with a single cam phaser this control strategy will regulate u_{soi} of only one cylinder (the reference cylinder) to its reference set point. The u_{soi} for other cylinders will be offset from the reference value to compensate for cylinder-to-cylinder variations in combustion phasing, as will be seen in the various experimental results presented in this work. These variations can be caused by manufacturing tolerances, unequal air charge distribution or engine cooling, non-uniform wear and tear, etc. Further note that large open-loop cylinder-to-cylinder variations in θ_{50} can lead to u_{soi} saturation.

Feedback Gain Selection

A nonlinear least-squares optimization was carried out on the closed loop system with actuator dynamics to determine the optimal feedback controller gains, as discussed in [71]. The three parameters that are optimized are the one proportional gain and two integral gains in H_v and H_f. A typical set of θ_{50}^{ref} and m_f^{inj} input steps was used in the optimization process. The ability of the controller to track θ_{50}^{ref} was evaluated using a cost function that balanced tracking error and controller effort. Gains were detuned on the engine to ensure that they were not overly aggressive. The feedback controller gains chosen are

$$K_p^{soi} = -1 \tag{4.1}$$

$$K_i^{soi} = -12\,\delta T_s \tag{4.2}$$

$$K_i^{evc} = 0.15\,\delta T_s \tag{4.3}$$

where δT_s is the sample time (the duration of one engine cycle). The negative signs for the u_{soi} gains are a result of the controller architecture chosen. It will be later seen in Chap. 5 that the K_p^{soi} gain changes sign for late phasing and low load conditions.

4.1.2 Feedforward

Model-based feedforward is used for u_{soi} to speed up transient responses. The linearized model from Sec. 3.8 is used to determine the steady state fuel injection timing input (u_{soi}^{ss}) needed to attain the desired combustion phasing output θ_{50}^{ref}, assuming that the current values of all other inputs (here u_{evc} and m_f^{inj}) persist at steady state. The linearized model at steady state is inverted as follows:

$$\begin{aligned}
\overline{x} &= A\overline{x} + B_{evc}u_{evc}(k) + B_f m_f^{inj}(k-1) + B_\omega \omega(k) + B_{soi}u_{soi}^{ss} \\
\theta_{50}^{ref}(k) &= C\overline{x} + D_{evc}u_{evc}(k) + D_f m_f^{inj}(k-1) + D_\omega \omega(k) + D_{soi}u_{soi}^{ss} \\
\therefore\ u_{soi}^{ss} = (u_{soi}^{ff}) &= [0 \quad 1] \begin{bmatrix} (A-I) & B_{soi} \\ C & D_{soi} \end{bmatrix}^{-1} \\
\cdot \begin{bmatrix} -B_{evc} & -B_f & -B_\omega & 0 \\ -D_{evc} & -D_f & -D_\omega & 1 \end{bmatrix} &\left[u_{evc}(k),\ m_f^{inj}(k-1),\ \omega(k),\ \theta_{50}^{ref}(k)\right]^T . \qquad (4.4)
\end{aligned}$$

Here $\overline{x}$ is the steady state value of the states. The feedforward component (u_{soi}^{ff}) is set to be u_{soi}^{ss}. Hence, the feedforward block in Fig. 4.2 is a fixed gain, and is computationally efficient to compute online. Since each cylinder can have distinct m_f^{inj} and θ_{50}^{ref} commands, and u_{evc} and ω vary continuously within the cycle, the controller generates four distinct values of the feedforward component of u_{soi} every cycle.

Note that the value of m_f^{inj} is delayed by one cycle before being used in the feedforward block. Varying the amount of fuel injected affects the steady state combustion phasing significantly through the subsequent variation in charge temperature. However, the charge temperature does not vary significantly for the first combustion event after the injection amount changes. Physically the change in temperature is only relevant after the first combustion event, through ΔT in Eq. (3.14). The controller is designed with a unit delay in the fuel amount feedforward path to account for this.

The accuracy of the model-based inversion reduces if the system is further away from the linearization point. This issue of linearization error is solved in the second control strategy presented in Chap. 6 where the nonlinear model is inverted to determine u_{soi} feedforward.

4.1.3 Stability of Closed Loop System

Stability of the closed loop system can be considered by using the linearized model of the plant, see Sec. 3.8, in place of the "Multi-Cylinder HCCI Engine" block of Fig. 4.2.

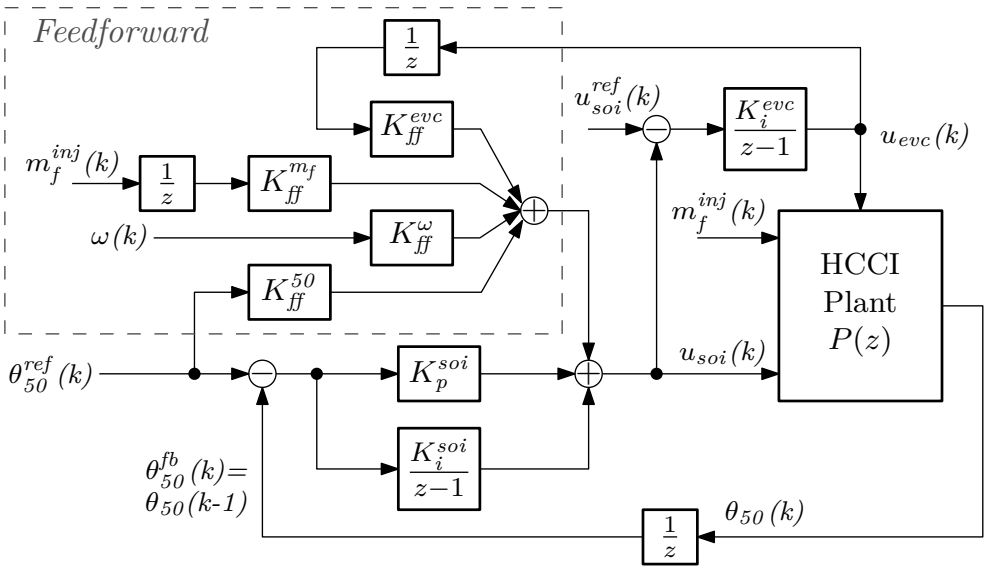

Figure 4.3: Representation of baseline controller for linear stability analysis. Here $P(z)$ is the linearized plant.

Controller Transfer Function Matrix

Using the system diagram outlined in Fig. 4.3, the controller transfer functions are:

$$U_{soi}(z) = \frac{z\,(z-1)}{z\,(z-1) + K_{ff}^{evc} K_i^{evc}} \begin{bmatrix} K_p^{soi} + K_{ff}^{50} + \dfrac{K_i^{soi}}{z-1} \\ -K_p^{soi} - \dfrac{K_i^{soi}}{z-1} \\ \dfrac{K_{ff}^{m_f}}{z} \\ K_{ff}^{\omega} \\ \dfrac{K_{ff}^{evc} K_i^{evc}}{z\,(z-1)} \end{bmatrix}^T \begin{bmatrix} \Theta_{50}^{ref}(z) \\ \Theta_{50}^{fb}(z) \\ M_f^{inj}(z) \\ \Omega(z) \\ U_{soi}^{ref}(z) \end{bmatrix} \tag{4.5}$$

$$U_{evc}(z) = \frac{K_i^{evc} z}{z\,(z-1) + K_{ff}^{evc} K_i^{evc}} \begin{bmatrix} -K_p^{soi} - K_{ff}^{50} - \dfrac{K_i^{soi}}{z-1} \\ K_p^{soi} + \dfrac{K_i^{soi}}{z-1} \\ -\dfrac{K_{ff}^{m_f}}{z} \\ -K_{ff}^{\omega} \\ 1 \end{bmatrix}^T \begin{bmatrix} \Theta_{50}^{ref}(z) \\ \Theta_{50}^{fb}(z) \\ M_f^{inj}(z) \\ \Omega(z) \\ U_{soi}^{ref}(z) \end{bmatrix}. \tag{4.6}$$

Here $\Theta_{50}^{ref}(z), M_f^{inj}(z), \Omega(z), U_{soi}^{ref}(z)$ are the z-transforms of $\theta_{50}^{ref}(k), m_f^{inj}(k), \omega(k)$ & $u_{soi}^{ref}(k)$ respectively. Also, $\Theta_{50}^{fb}(z)$ is the z-transform of the feedback output $\theta_{50}(k-1)$. Mathematically, $\theta_{50}^{fb}(k) = \theta_{50}(k-1)$ or $\Theta_{50}^{fb}(z) = \frac{\Theta_{50}(z)}{z}$.

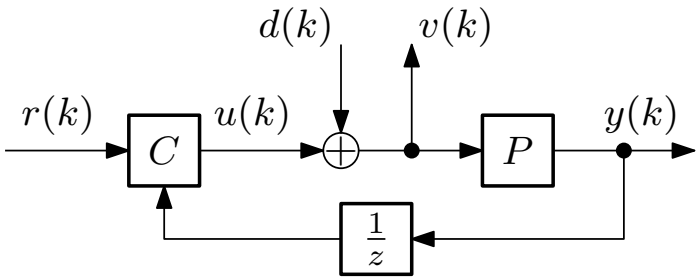

Figure 4.4: Feedback system overview for four transfer function analysis. Here C is the controller and P is the plant.

Note that in a traditional mid-ranging with feedforward architecture application, the feedforward term from the slow actuator to the fast actuator (here from u_{evc} to u_{soi}) is absent. This corresponds to the limiting condition $K_{ff}^{evc} = 0$ in Eq. (4.5) and Eq. (4.6). In this special case, the transfer functions would be significantly simpler, and the coupling from $u_{soi}^{ref}(k)$ to $u_{soi}(k)$ would not exist. However in this work, $K_{ff}^{evc} \neq 0$ to correctly account for the effects of u_{evc} variation when inverting the linearized model, as explained in Sec. 4.1.2.

In the current application, the numerical values of the controller transfer functions are:

$$U_{soi}(z) = \frac{1}{(z-0.9615)(z-0.03849)} \begin{bmatrix} -7.1825z(z-0.8886) \\ z(z-0.2) \\ -19.0439(z-1) \\ -0.041581z(z-1) \\ 0.037008 \end{bmatrix}^T \begin{bmatrix} \Theta_{50}^{ref}(z) \\ \Theta_{50}^{fb}(z) \\ M_f^{inj}(z) \\ \Omega(z) \\ U_{soi}^{ref}(z) \end{bmatrix} \tag{4.7}$$

$$U_{evc}(z) = \frac{z}{(z-0.9615)(z-0.03849)} \begin{bmatrix} \frac{0.071825(z-0.8886)}{(z-1)} \\ \frac{-0.01(z-0.2)}{(z-1)} \\ \frac{0.19044}{z} \\ 0.00041581 \\ 0.01 \end{bmatrix}^T \begin{bmatrix} \Theta_{50}^{ref}(z) \\ \Theta_{50}^{fb}(z) \\ M_f^{inj}(z) \\ \Omega(z) \\ U_{soi}^{ref}(z) \end{bmatrix}. \tag{4.8}$$

Four Transfer Function Theorem for Stability

The controller transfer functions are augmented with the linearized plant from Sec. 3.8, as shown in Fig. 4.4. The signals introduced in the figure are as follows:

$$\text{Reference:} \quad r(k) = \left[\theta_{50}^{ref}(k),\ m_f^{inj}(k),\ \omega(k),\ u_{soi}^{ref}(k)\right]^T \tag{4.9}$$

$$\text{Input:} \quad u(k) = \left[u_{soi}(k),\ u_{evc}(k),\ m_f^{inj}(k),\ \omega(k)\right]^T \tag{4.10}$$

$$\text{Disturbance:} \quad d(k) = \left[\Delta u_{soi}(k),\ \Delta u_{evc}(k),\ \Delta m_f^{inj}(k),\ \Delta\omega(k)\right]^T \tag{4.11}$$

$$\text{Input to Plant:} \quad v(k) = u(k) + d(k) \tag{4.12}$$

$$\text{Output:} \quad y(k) = \theta_{50}(k) \tag{4.13}$$

In Fig. 4.4, P and C are the plant and the controller respectively. From Eq. (4.7) to Eq. (4.13), P and C are represented as:

$$\text{Controller } (C): \quad U(z) = \begin{bmatrix} U_{soi}(z) \\ U_{evc}(z) \\ M_f^{inj}(z) \\ \Omega(z) \end{bmatrix} = C \begin{bmatrix} \Theta_{50}^{ref}(z) \\ \Theta_{50}^{fb}(z) \\ M_f^{inj}(z) \\ \Omega(z) \\ U_{soi}^{ref}(z) \end{bmatrix} \tag{4.14}$$

$$\text{Plant } (P): \quad Y(z) = \Theta_{50}(z) = P \begin{bmatrix} U_{soi}(z) \\ U_{evc}(z) \\ M_f^{inj}(z) \\ \Omega(z) \end{bmatrix} + PD(z) \tag{4.15}$$

To analyze stability of the closed loop system, the four transfer function matrix T_{4TF} [72] from inputs r and d to the outputs y and v is considered. It is given as:

$$\begin{bmatrix} Y \\ V \end{bmatrix} = T_{4TF} \begin{bmatrix} R \\ D \end{bmatrix}, \tag{4.16}$$

where Y, V, R, D are the z-transform representations of the y, v, r, d signals respectively. Further,

$$T_{4TF} = \begin{bmatrix} T_O & PS_I \\ S_I C & S_I \end{bmatrix}. \tag{4.17}$$

Here T_O is the output complementary sensitivity function (the transfer function from

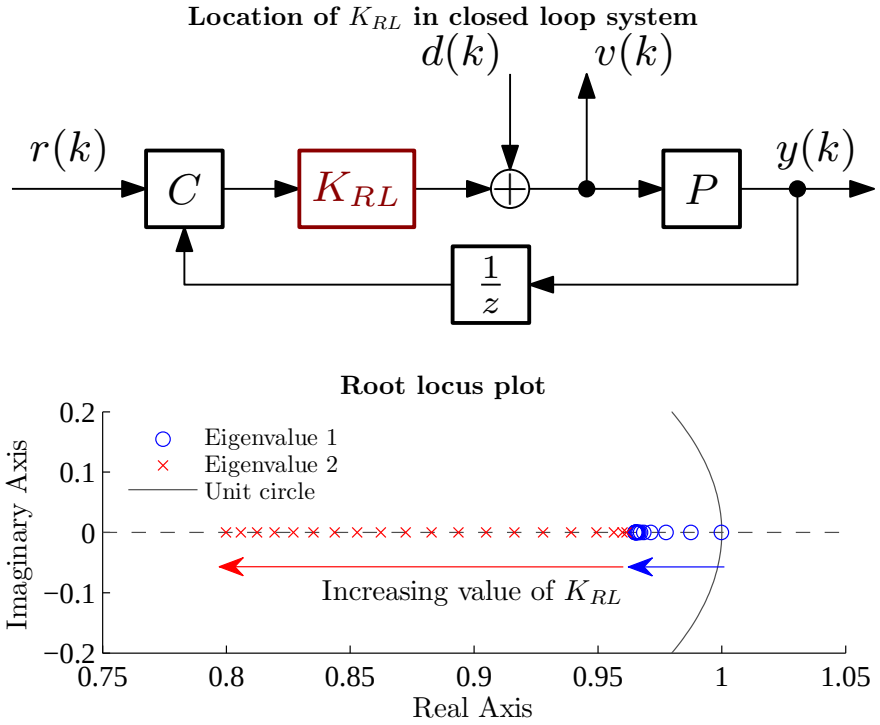

Figure 4.5: The root locus gain (K_{RL}) is swept from 0 to 2, with $K_{RL} = 1$ being the nominal closed loop system. The root locus plot focuses on the two poles closest to the unit circle.

r (reference) as input to y (plant output) as output), and S_I is the input sensitivity function (the transfer function from d (input disturbance) as input to v (plant input) as output).

The plant (see Sec. 3.8) and controller (see Eq. (4.7) and Eq. (4.8)) transfer functions have no unstable modes. Further, all poles of the four transfer function matrix T_{4TF} given by Eq. (4.16) and Eq. (4.17) are within the unit circle (closed loop poles $\in$ {0.9655, 0.8725, 0.6668, 0.2512, -0.01735}). Hence by the four transfer function theorem for multivariable systems [72], the closed-loop system is internally stable.

Root Locus Analysis

Two of the closed loop poles (0.9655 and 0.8725) are close to the unit circle. A simplified multivariate root locus analysis is performed in Fig. 4.5 to demonstrate that these poles correspond to the open loop poles closest to the unit circle (namely the integrator pole and the pole 0.9615 from the controller). Further, it is seen that the closed loop feedback pulls these open loop poles away from the unit circle, and thus away from instability. In this analysis, the controller output $u(k)$ is multiplied

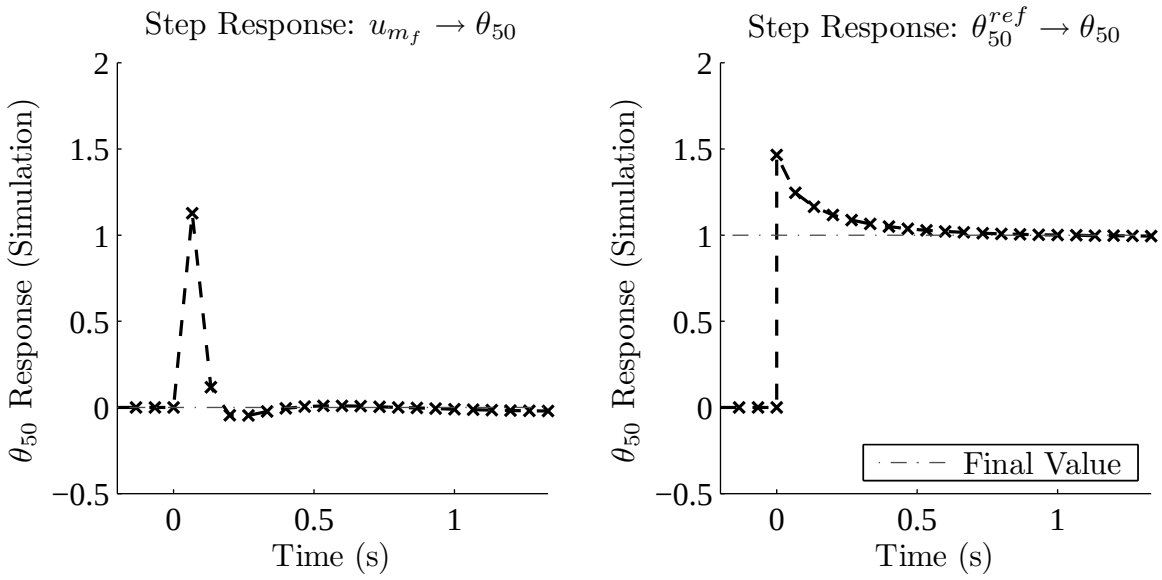

Figure 4.6: Closed-loop step responses for the system presented in Fig. 4.4. The responses of the output variable (θ_{50}) to steps in reference variables ($m_f^{inj}, \theta_{50}^{ref}$) are shown. Note that θ_{50} in this linear analysis is offset from its nominal linearization value, and so $\theta_{50} = 0$ here actually means $\theta_{50} = 6.03$ °CA aTDC, as defined in Tab. 3.1.

by the root locus gain (K_{RL}). This root locus gain is swept from 0 to 2 ($K_{RL} = 1$ is the nominal closed loop system). Finally note that the closed loop pole closest to the unit circle is attracted to a stable zero.

Closed Loop Step Responses

Figure 4.6 demonstrates that the closed-loop step response of the system is satisfactory. In this figure the two main closed-loop inputs ($m_f^{inj}, \theta_{50}^{ref}$) are stepped by unity. The responses of the simulated combustion phasing output are plotted. The closed-loop system rejects the m_f^{inj} disturbance in a few cycles. The closed-loop system tracks the step in reference combustion phasing well, again in a few engine cycles.

4.1.4 Experimental Validation during Small Load Transitions

The baseline controller works well for small to mid load transitions, as seen in Fig. 4.7 where m_f^{inj} is stepped from 10.5 to 8.8 mg/cycle at cycle number 30. The torques for all four cylinders step smoothly from the initial to the final values without any spikes

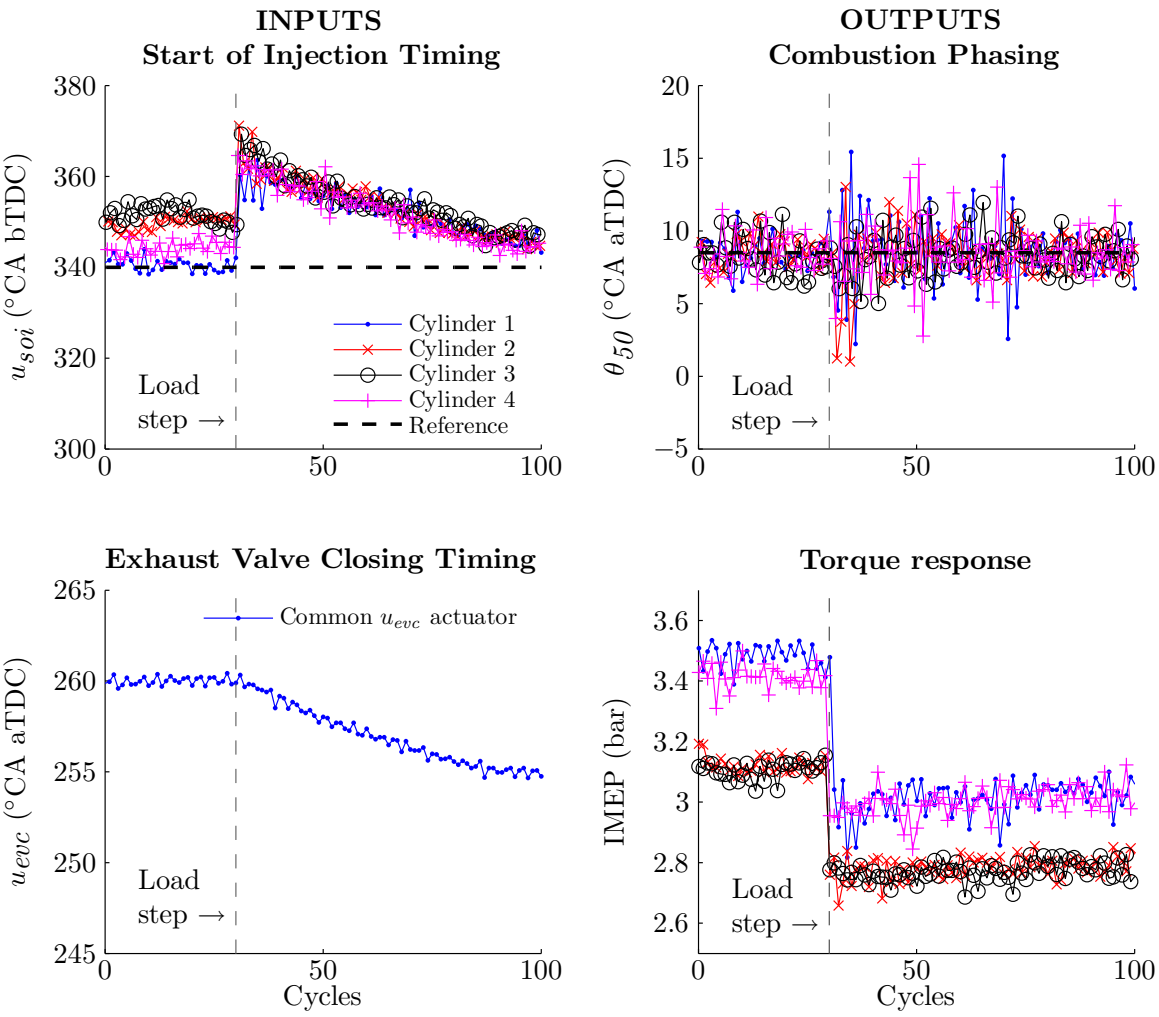

Figure 4.7: Baseline controller – satisfactory transient response for small load steps (m_f^{inj} : 10.5 → 8.8 mg/cycle). The controller inputs (u_{soi} and u_{evc}) are presented to the left and the performance outputs (θ_{50} and IMEP) are to the right.

or dips. Note that the cylinder torques differ due to cylinder-to-cylinder variability in a multi-cylinder engine. The combustion phasing output θ_{50} is regulated to the set-point of 8.5 °CA aTDC, and stays within reasonable bounds during the load transition.

The controller outputs u_{soi} and u_{evc} in Fig. 4.7 demonstrate the typical response of the fast and the slow actuators in a mid-ranging based control strategy. The initial transient response to the load transition lasts for a few engine cycles, and is almost entirely compensated for by u_{soi}. The sudden initial change in u_{soi} at cycle number 30 is due to the model-based feedforward of Sec. 4.1.2. The fast actuator u_{soi} then compensates for deviations of θ_{50} from its reference value θ_{50}^{ref}, here 8.5 °CA aTDC. The slower actuator u_{evc} slowly returns u_{soi} to its reference set-point, which is roughly in the middle of its range of authority. The reference set-point here is 340 °CA aTDC. This mid-ranging of u_{soi} happens over many tens of cycles.

Note that only u_{soi} of cylinder 1 mid-ranges correctly to the reference set-point of 340 °CA aTDC. This is because there is only one u_{evc} actuator for the entire engine, and it is controlled by an integral controller driven by the u_{soi} tracking error for a fixed reference cylinder, here cylinder 1.

Equal amounts of fuel are commanded in each cylinder. Cylinder-to-cylinder variations result in different load levels for each cylinder. Although these imbalances can be compensated for by a feedback loop from m_f^{inj} to IMEP, this was not implemented in the current study to avoid disturbances from this loop.

4.1.5 Poor Performance during Larger Load Transitions

Large HCCI load transitions lead to large changes in the charge temperature, and potentially to large undesired variations in combustion phasing. The baseline controller is unable to reject these variations in θ_{50}. This is seen in Fig. 4.8, where the baseline controller exhibits poor θ_{50} and IMEP tracking performance after a large load step down (m_f^{inj} : 11.4 $\rightarrow$ 8.8 mg/cycle).The baseline controller tries to compensate for the large charge temperature drop caused when m_f^{inj} is stepped over a single cycle. After m_f^{inj} is stepped down at cycle 30, the IMEP suddenly drops to nearly zero, indicating an engine misfire. The θ_{50} response after the load step down is poor. Note that the high cyclic variability is seen to persist several tens of cycles after the transition. This behavior is discussed in Chap. 5. The fuel governor add-on block, developed in the Sec. 4.2, is developed to improve the poor performance during larger transitions.

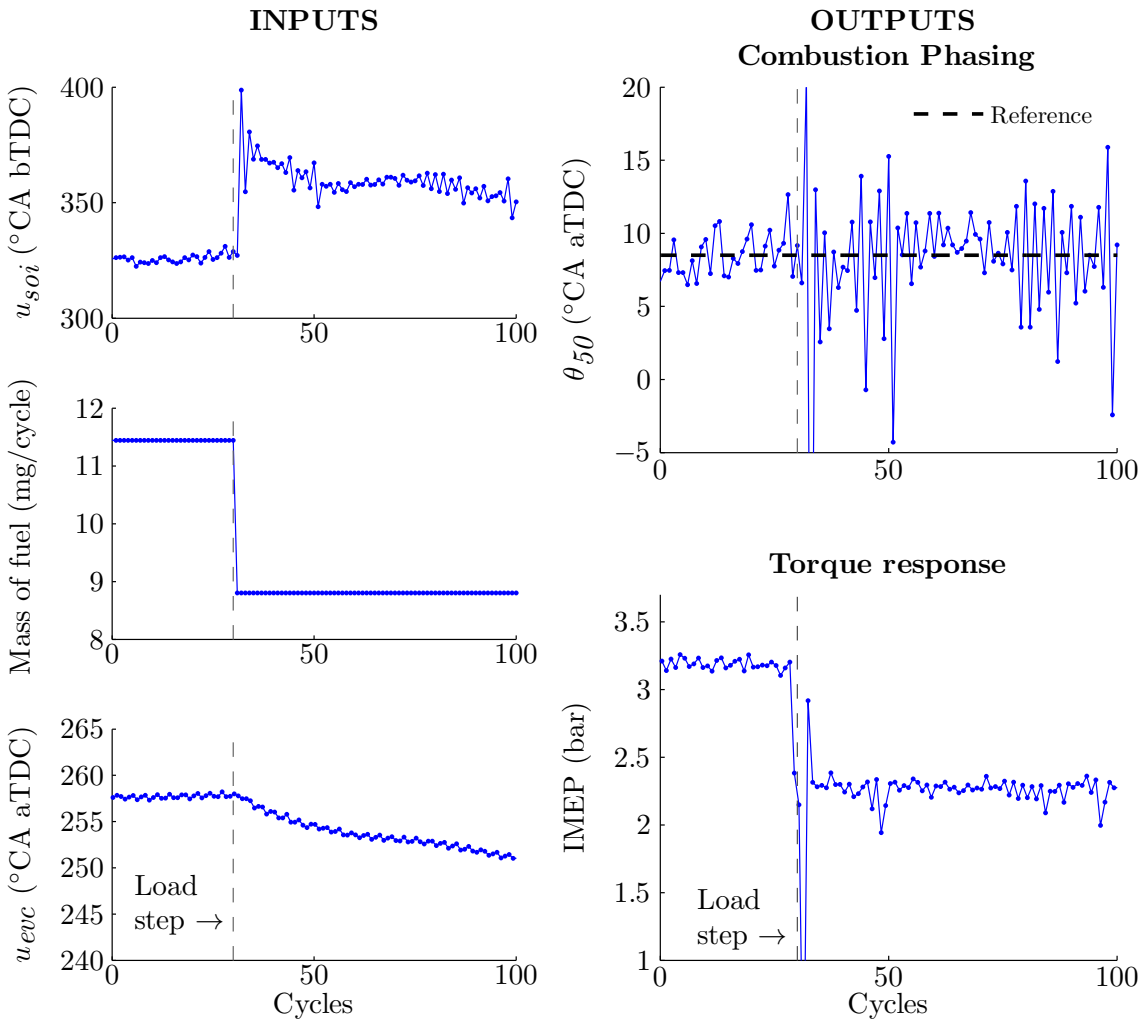

Figure 4.8: Baseline controller: Poor transient response for a larger load step (m_f^{inj} : 11.4 → 8.8 mg/cycle) than Fig. 4.7. The engine load drops suddenly after the transition, and the θ_{50} response is highly oscillatory. Results are presented for a single cylinder for clarity.

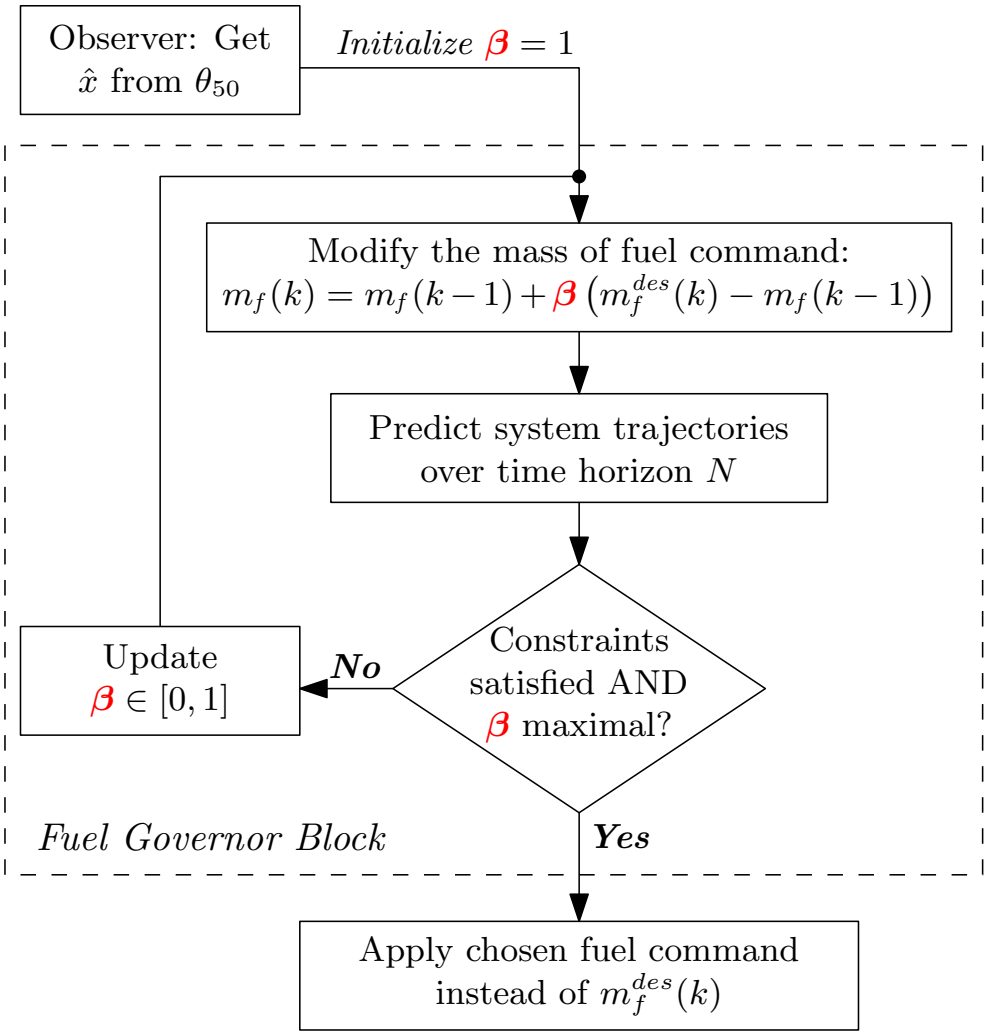

Figure 4.9: Fuel governor methodology flowchart. The parameter β is optimized.

4.2 Fuel Governor

The fuel governor is a type of reference governor that modifies the desired fuel mass command ($m_f^{des}(k)$) by enforcing pointwise-in-time actuator constraints. This is shown to improve the transient response of combustion phasing and load during large load transitions, when the possibility of future constraint violations exists. As seen in Fig. 4.1, the fuel governor is added on to the controller-augmented system.

A general overview of the fuel governor control strategy is presented in Fig. 4.9. The fuel governor utilizes the receding horizon principle to check for actuator constraint violation. Note that the governor requires a model of the plant to calculate future trajectories, and a state observer to estimate the current system state ($\hat{x}(k)$). The performance of the governor thus depends on the fidelity of the plant model and the

accuracy of the state observer.

There are three important characteristics of the fuel governor control strategy. First, the fuel governor is an add-on block that augments existing control architectures, and doesn't completely replace them. This enables separation of control tasks, which makes the overall control design easier. For example, in the current application, the combustion phasing regulation problem is handled by the baseline controller using u_{soi} and u_{evc}, while the actuator constraint enforcement task is handled by the fuel governor that modifies m_f^{inj}. Second, the fuel governor problem optimizes a single variable (m_f^{inj}) to find the largest fuel mass change that will not violate actuator constraints. Optimizing a single variable is less complex, easier to implement, and computationally cheaper than other online optimization schemes such as model predictive control of all actuators. Finally, the overall effect of the governor is to act as a model-based filter with a variable time constant that slows down large m_f^{inj} steps. Compared to fixed-constant filters or other heuristic solutions, the governor has the advantage of being model based. This means that the slowing down of m_f^{inj} is not too slow (which would lead to overly slow transitions) or too fast (which could lead to degraded performance and excessive θ_{50} variation).

Actuator Constraints: The actuator constraints considered in this work are saturation constraints on u_{soi} and u_{evc} and rate constraints on u_{evc}. It was observed that u_{soi} saturation was the only active constraint in experiments, and it was always violated before the u_{evc} constraints. This is a result of the mid-ranging feedback gains chosen for the inner controller.

Fuel Governor Variants: In this work, three different fuel governor designs are proposed. They vary in design complexity, computational load, and ease of implementation:

1. Nonlinear Fuel Governor, refer Sec. 4.2.2. Here the prediction model is the full nonlinear model.
2. Linearized Fuel Governor, refer Sec. 4.2.3. Here the prediction model is a linearized version of the nonlinear model .
3. Analytical Fuel Governor, refer Sec. 4.2.4. Here the linearized close loop model is used to derive analytical expressions for constraint violation. Constraint enforcement over a time horizon of N cycles is expressed analytically as the intersection of N permissible fuel subsets.

Two of these strategies, the nonlinear and linearized fuel governor have been validated experimentally. The third strategy, the analytical fuel governor, is tested in simulations.

4.2.1 Reference Governor Control in Literature

Fuel governors are based on the reference governor concept which separates the closed loop design from the constraint enforcement requirement. Reference governors can be defined as nonlinear devices which are added to a primal compensated linear system in order to modify, when necessary, the reference signal in such a way the constraints are enforced and the compensated system maintains its linear behavior [73].

One of the first mentions of reference governors was by Kapasouris et al. [74, 75]. The authors introduce the concepts of "error governor" and "reference governor" that modify exogenous signals that can potentially cause future control saturation. The problem is formulated as maximization of a gain parameter or an alternative rate parameter. Gilbert et al. [76] present a discrete-time modification of the continuous-time error governor scheme presented in [74]. Output admissible sets O_∞ are computed and, at each time instant, the state is driven into these sets. By working with discrete time O_∞, instead of continuous time O_∞, significant runtime savings were achieved. Bemporad et al. [73, 77, 78] are influenced by model predictive control, and define parametrically expressed virtual reference inputs based on the reference command. They also discuss the receding horizon, closed loop prediction method used in this work. A class of virtual constant reference input signals parameterized by scalar β are introduced where $w(kT + \sigma, \beta) = r(kT) + \beta\,[w((k-1)T) - r(kT)]$.

Several theoretical advances involving stability analysis, extensions to nonlinear models and constraints, extensions to discrete and continuous time, and prototypical examples can be found in reference governor literature, see for example [73–82]. Reference governors have been applied widely in literature, for example to prevent fuel cell oxygen starvation [83–86], in hydroelectric power generation [87, 88] and in turbocharged diesel engine supplemental torque control [89]. Close to 100 papers have been published on different aspects of reference governor theory and applications.

4.2.2 Nonlinear Fuel Governor Design

The nonlinear fuel governor uses the full nonlinear HCCI combustion model presented in Chap. 3 to predict future variable trajectories. It modifies m_f^{inj} if future actuator constraint violations are predicted, as summarized in the algorithm below. Similar to [83], a bisectional search is carried out on the desired change in m_f^{inj} until the optimal change is found. This involves the optimization of a single parameter (β):

$$m_f^{inj}(k) = m_f^{inj}(k-1) + \beta \cdot (m_f^{des}(k) - m_f^{inj}(k-1)). \tag{4.18}$$

Ideally β is set to 1, in which case the fuel governor has no effect, and the desired fuel step is applied unmodified.

Algorithm: Bisectional search to maximize β in (4.18)

Input: Time horizon $N \geq 1$, tolerance $\epsilon \in [0, 1]$
Output: β in (4.18)

$i \leftarrow 1$, $\beta_0 \leftarrow 1$, $\beta_1 \leftarrow 1$, $\overline{\beta} \leftarrow 1$, $\underline{\beta} \leftarrow 0$
loop
  $m_f^{inj} \leftarrow m_f^{inj}(k-1) + \beta_i \cdot (m_f^{des}(k) - m_f^{inj}(k-1))$
  Simulate system over time horizon $\{k, \ldots, k+N\}$, initialized with current state of system $\hat{x}(k)$
  if Constraints are satisfied **then**
    if $(|\beta_i - \beta_{i-1}| \leq \epsilon)$ **then**
      return $\beta \leftarrow \beta_i$
    else
      $\underline{\beta} \leftarrow \beta_i$
    end if
  else
    $\overline{\beta} \leftarrow \beta_i$
  end if
  $i = i + 1$, $\beta_i = \frac{\underline{\beta}+\overline{\beta}}{2}$
end loop

At every time step, the system is initialized at the current system states ($\hat{x}(k)$), which are determined from a Luenberger observer designed using the linearized model presented in Sec. 3.8. The closed loop system is simulated over a fixed future time horizon (N) with the fuel level maintained at $m_f^{inj}(k)$ calculated in (4.18). The parameter β is reduced if constraint violations are detected, and is increased if all constraints are satisfied. The optimal value of $\beta \in [0, 1]$ is obtained subject to a predetermined convergence tolerance (ϵ). This process ensures that the tracking error between the desired and actual fuel levels is reduced.

Further, the saturation of β ensures that the applied fueling trajectory will remain bounded within the range defined by the initial and the desired fueling levels, and that this trajectory will be monotonic. If the fuel governor determines that the desired fuel step is infeasible, then a value of $\beta = 0$ (or $\beta \leq \epsilon$, depending on the configuration of the system) is determined. This means that the fueling level is left unchanged (or changed by a very small value). This situation persists till feasibility is determined by the governor.

4.2.3 Linearized Fuel Governor Design

The nonlinear fuel governor can be computationally expensive. The optimization of β in Eq. (4.18) must be run in real-time four times a cycle, to determine the m_f^{inj} input for every cylinder. Depending on the engine speed, the values of the time horizon N, and the convergence tolerance ϵ from the previously discussed algorithm, the nonlinear prediction model may have to be run several thousand times every second. The nonlinear fuel governor code was optimized and it ran in real-time on the experimental hardware described in Chap. 2. However using the nonlinear prediction model in the governor may be infeasible on less computationally powerful commercial engine control hardware.

To reduce computational load, the nonlinear prediction model is linearized about a chosen operating point. The computational procedure remains the same. Experimental results in Sec. 4.3 demonstrate that this strategy improves runtime significantly, with little loss of performance. Alternative schemes to speed up reference governor computation times are discussed in literature, see for example [80, 84].

4.2.4 Analytical Fuel Governor Design

Another scheme to reduce computation time is the analytical fuel governor, which has been tested in simulation. The linearized closed-loop model (combustion plant model augmented with the baseline controller) can be used to analytically derive expressions for constraint violation. The online portion of the fuel governor is then reduced to evaluating a set of simple algebraic equations with pre-computed scalar coefficients. This significantly reduces the computation time required, at a slight cost of fuel governor performance.

The linearized combustion model developed in Sec. 3.8 is augmented with the baseline controller developed in Sec. 4.1. The state space representation of this closed loop system with inputs being mass of fuel m_f^{inj} and θ_{50}^{ref} and outputs being u_{evc} and u_{soi} is given by (4.19):

$$\begin{aligned} x_{CL}(k+1) &= A_{CL}x_{CL}(k) + B_f m_f^{inj}(k) + B_{ref}\theta_{50}^{ref}(k) \\ u_{evc}(k) &= C_1 x_{CL}(k) + D_{f,1} m_f^{inj}(k) + D_{ref,1}\theta_{50}^{ref}(k) \\ u_{soi}(k) &= C_2 x_{CL}(k) + D_{f,2} m_f^{inj}(k) + D_{ref,2}\theta_{50}^{ref}(k) \end{aligned} \tag{4.19}$$

where x_{CL} is the state vector of the closed loop system, which is the union of the

combustion model states and the controller states.

The fuel governor checks if the desired mass of fuel m_f^{des} is permissible in the following manner. The initial state $x_{CL}(0)$ of the closed loop system is estimated by the observer. Assuming that the inputs m_f^{inj} and θ_{50}^{ref} stay constant over the time horizon $N \geq 1$ considered, algebraic closed form solutions are derived for the evolution of u_{evc} and u_{soi} over future cycles $1, \ldots, N$. For example, u_{evc} n cycles into the simulation is given by (4.20):

$$\begin{aligned} u_{evc}(n) &= C_1 A_{CL}^n x_{CL}(0) \\ &+ \left(C_1 \left(A_{CL}^{(n-1)} + \ldots + A_{CL} + I \right) B_{ref} + D_{ref,1} \right) \theta_{50}^{ref} \\ &+ \left(C_1 \left(A_{CL}^{(n-1)} + \ldots + A_{CL} + I \right) B_f + D_{f,1} \right) m_f^{inj}. \end{aligned} \tag{4.20}$$

This is then inverted to give (4.21), where m_f^{inj} is expressed as a linear function of $u_{evc}(n)$, and γ_x are fixed scalars that can be calculated offline:

$$m_f^{inj}(n) = \gamma_1(n) u_{evc}(n) + \gamma_2(n, x_{CL}(0), \theta_{50}^{ref}). \tag{4.21}$$

Let $S_{evc}^{sat}(n)$ be the range of fuel amounts permissible for the u_{evc} saturation constraint to be satisfied in cycle n. Since (4.21) is linear, this can be characterized by plugging in the maximum and minimum actuator limits u_{evc}^{max} and u_{evc}^{min}:

$$\begin{aligned} m_f^{min}(n) &= \gamma_1(n) u_{nvo}^{max} + \gamma_2(n, x_{CL}(0), \theta_{50}^{ref}) \\ m_f^{max}(n) &= \gamma_1(n) u_{nvo}^{min} + \gamma_2(n, x_{CL}(0), \theta_{50}^{ref}) \\ S_{nvo}^{sat}(n) &= \left[m_f^{min}(n), m_f^{max}(n) \right]. \end{aligned} \tag{4.22}$$

This process is repeated over the time horizon N and a family of subsets $S_{evc}^{sat}(k)$, $k \in \{1, \ldots, N\}$ is generated. The intersection of all of these subsets gives $\overline{S_{evc}^{sat}}$, which is the permissible fuel range for the u_{evc} saturation constraint to be satisfied over the entire time horizon:

$$\overline{S_{evc}^{sat}} = \bigcap_{k=\{1,\ldots n\}} S_{evc}^{sat}(k). \tag{4.23}$$

The other actuator constraints in Sec. 4.2 can be handled similarly to obtain $\overline{S_{evc}^{rate}}$ and $\overline{S_{soi}^{sat}}$, which are the permissible fuel ranges for the u_{evc} rate constraint and the u_{soi} saturation constraint respectively to be satisfied over the entire time horizon. The overall minimum (m_f^{min}) and maximum (m_f^{max}) fuel masses that satisfy all constraints

are given in (4.24). Finally the fuel mass injected ($m_f(k)$) is given by (4.25):

$$\left[m_f^{min}, m_f^{max}\right] = \overline{S_{evc}^{sat}} \cap \overline{S_{evc}^{rate}} \cap \overline{S_{soi}^{sat}} \tag{4.24}$$

$$m_f^{inj}(k) = \begin{cases} m_f^{min} & \text{if } m_f^{des}(k) < m_f^{min}, \\ m_f^{max} & \text{if } m_f^{des}(k) > m_f^{max} \\ m_f^{des}(k) & \text{otherwise.} \end{cases} \tag{4.25}$$

The coefficients in all of these equations are known and can be calculated offline. The fuel governor is reduced to solving a set of algebraic equations with known coefficients.

4.3 Experimental Fuel Governor Results

The nonlinear fuel governor and the linearized fuel governor strategies developed in Sec. 4.2.2 and Sec. 4.2.3 were implemented on the rapid prototyping hardware and used to regulate θ_{50} during load transitions. The main advantages of the fuel governor strategy validated by experiments are:

1. Improved θ_{50} and IMEP transient responses during load transitions, when the possibility of constraint violations exists, see Sec. 4.3.1.
2. The enabling of larger load transitions than were possible with the baseline controller alone, see Sec. 4.3.2.

The performance of the nonlinear and linearized fuel governors are compared. The governor strategy is validated at different engine speeds and boost pressures.

4.3.1 Improved Performance during Larger Load Transitions

Figure 4.10 compares the performance for the baseline controller and the nonlinear fuel governor for a larger load transition considered in Fig. 4.8. Here m_f^{inj} is stepped from 11.4 to 8.8 mg/cycle at cycle number 30. The baseline controller tries to compensate for the large charge temperature drop caused when m_f^{inj} is stepped over a single cycle. Significant variability in θ_{50} and IMEP responses is seen in the first few cycles after the load transition. The combustion phasing response is rough and oscillatory. The torque output drops sharply, indicative of incomplete combustion and misfire. The engine continued to run in the experimental dynamometer environment, but this could cause an unacceptable engine stall in a vehicle.

In contrast, the nonlinear fuel governor demonstrates significantly improved θ_{50} and IMEP transients. The combustion phasing response is smoother, while engine

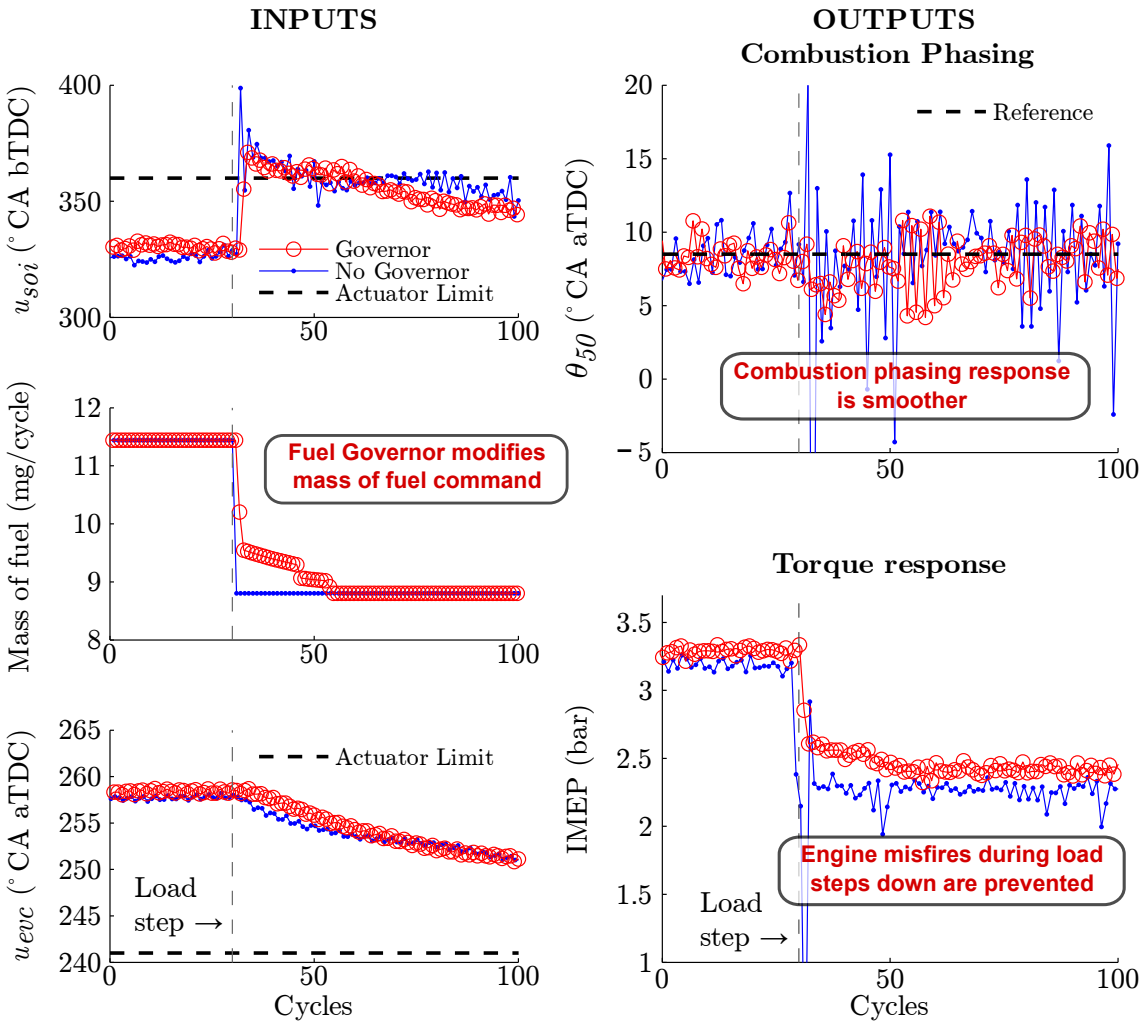

Figure 4.10: Comparison between baseline controller and nonlinear fuel governor – improved θ_{50} and IMEP transient responses during load transitions, when the possibility of constraint violations exists. Compare with Fig. 4.8.

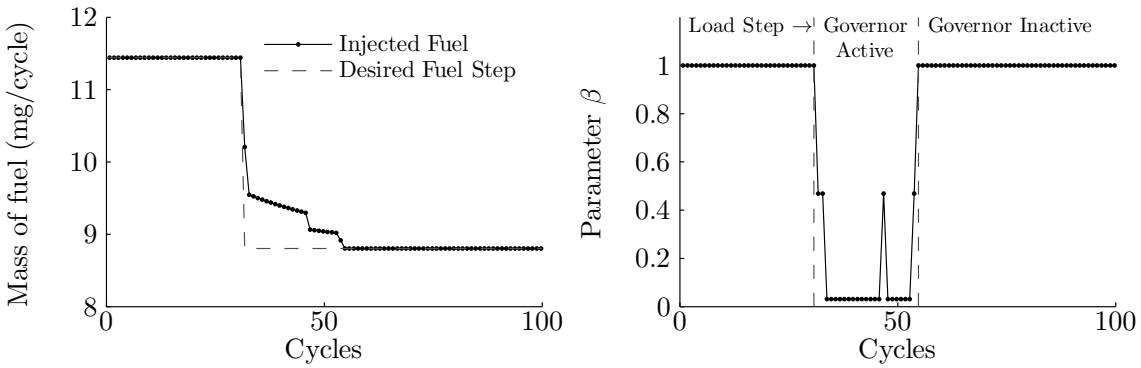

Figure 4.11: Variation in fuel governor parameter β during a typical load transient.

misfires are prevented. The result is a smoother torque transition during the load step down. The fuel governor achieves these improvements by slowing down the m_f^{inj} command when the possibility of future actuator constraint violations exist. In this particular case the actuator constraint that is active is the u_{soi} saturation constraint.

It is seen that u_{soi} slightly exceeds the actuator limit. Some of the design choices made to reduce complexity increase errors in the actuator position predictions. The simplified prediction model developed in Chap. 3 does not fully represent engine dynamics. Further, the nonlinearities inherent in the system cause increased errors in the state estimated by the linear observer away from the nominal operating point. The constraints have to be made more conservative to account for this.

Given the desired m_f^{des} and actual m_f^{inj} trajectories, the value of parameter β in the fuel governor is given by

$$\beta(k) = \frac{m_f^{inj}(k) - m_f^{inj}(k-1)}{m_f^{des}(k) - m_f^{inj}(k-1)}. \tag{4.26}$$

Figure 4.11 shows a typical fuel governor m_f^{inj} transient and the associated β plot. A large portion of the step happens in the first cycle. The size of this step is limited by the active constraint (here u_{soi} saturation). The optimal value of $\beta \in [0, 1]$ is obtained subject to the convergence tolerance (ϵ).

In general, tip-in responses are not as challenging as tip-out responses. The increased fuel amount and temperatures lead to earlier combustion phasing. This can cause ringing without the governor, but not combustion failures or misfires. Hence the potential improvement shown by the governor is less dramatic.

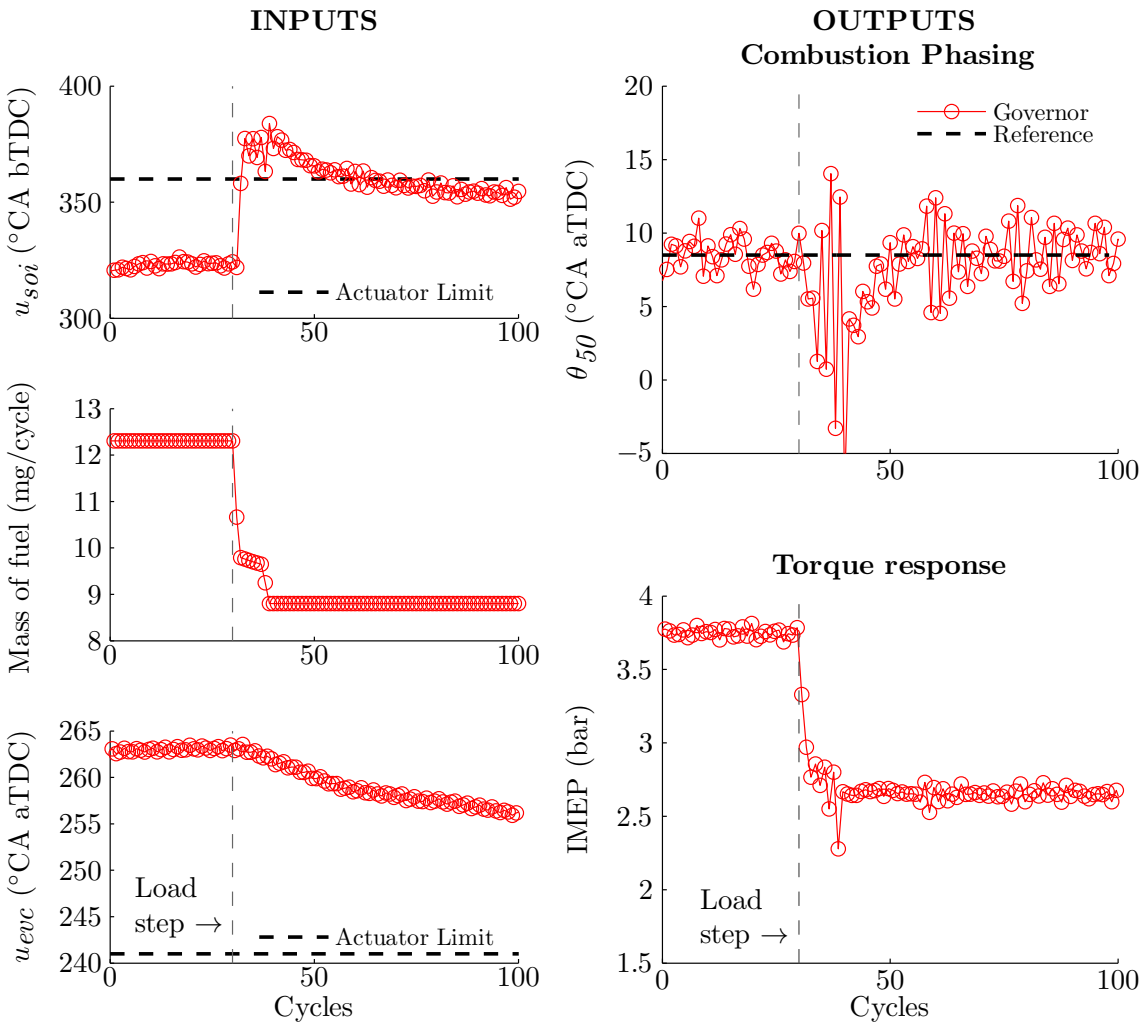

Figure 4.12: Nonlinear fuel governor – larger load transitions than were possible with the baseline controller alone. Here m_f^{inj} : 12.3 to 8.8 mg/cycle.

4.3.2 Extending Load Transition Range

The nonlinear fuel governor enables larger load transitions than were possible with the baseline controller. An example of this is demonstrated in Fig. 4.12 for a m_f^{inj} transition from 12.3 to 8.8 mg/cycle at cycle number 30. Instead of m_f^{inj} stepping in a single cycle, the transition occurs over a few cycles, leading to smooth torque and combustion phasing responses. As discussed in the previous section, the actuator constraints have to be made more conservative than their actual values. At these operating conditions, a commanded u_{soi} maximum limit of 360 °CA bTDC corresponds to an experimentally observed limit of 375 °CA bTDC.

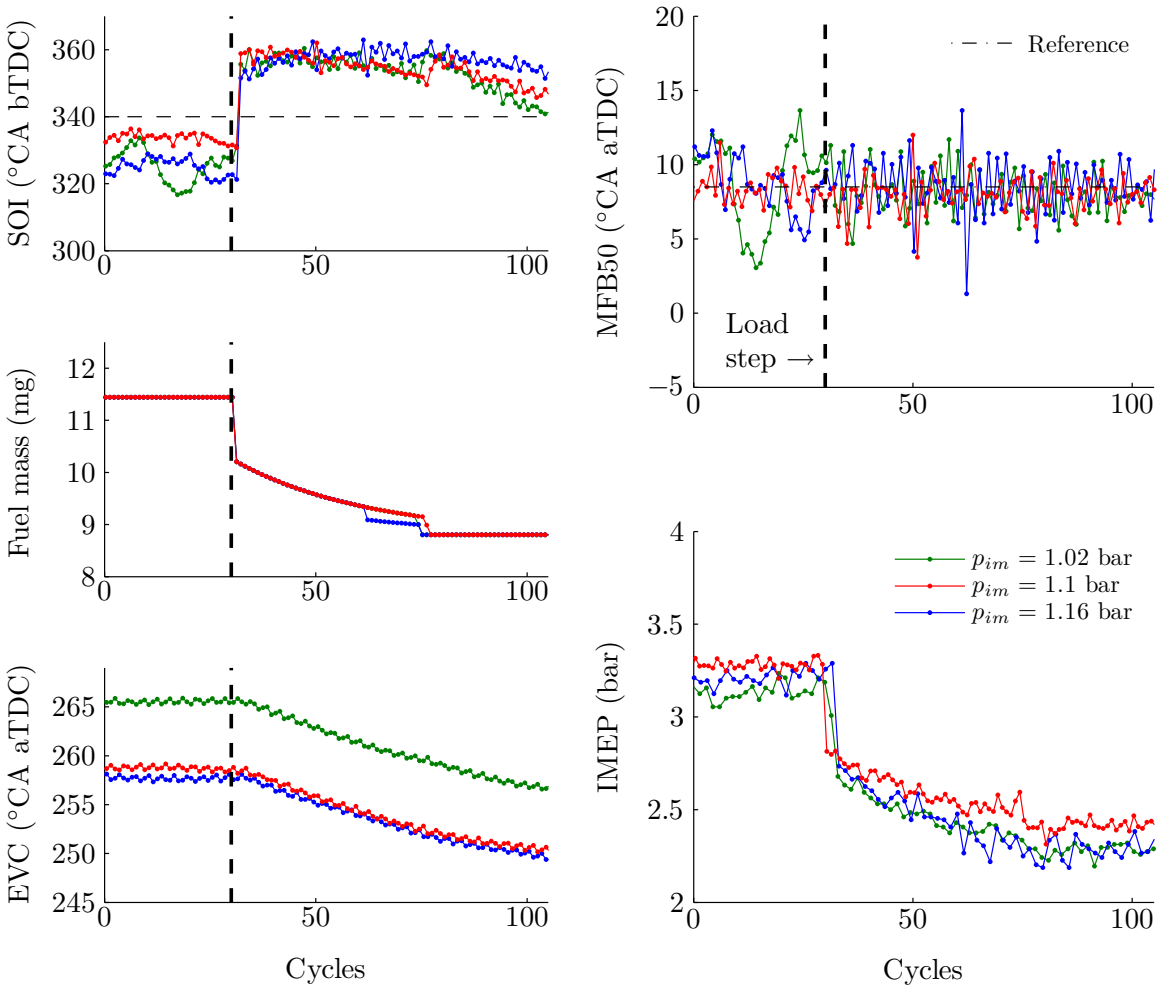

Figure 4.13: Nonlinear fuel governor – the boost pressure is varied from the nominal $p_{im} = 1.1$ bar.

4.3.3 Variation in Boost Pressure

In Fig. 4.13 the same m_f^{inj} transition from 11.4 to 8.8 mg/cycle is carried out for three intake manifold pressure conditions around the nominal value of p_{im} =1.1 bar. The nonlinear fuel governor performs satisfactorily for the small variation in boost pressure. As discussed in the previous section, the actuator constraints have to be made more conservative than their actual values. At these operating conditions, a commanded u_{soi} maximum limit of 350 °CA bTDC corresponds to an experimentally observed limit of around 360 °CA bTDC.

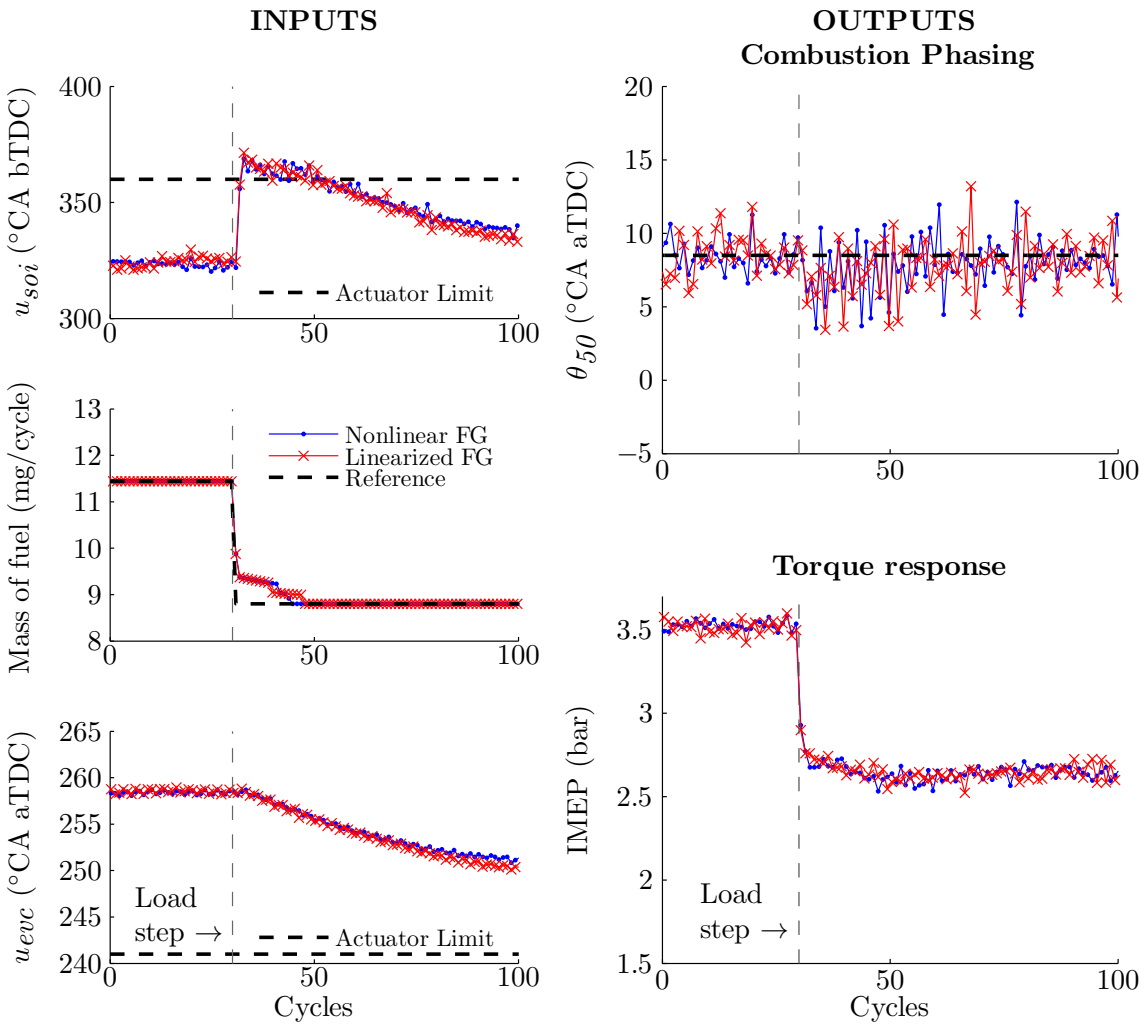

Figure 4.14: Comparison between nonlinear and linearized fuel governor. The performance of both governors is very similar. Here m_f^{inj} : 11.4 → 8.8 mg/cycle.

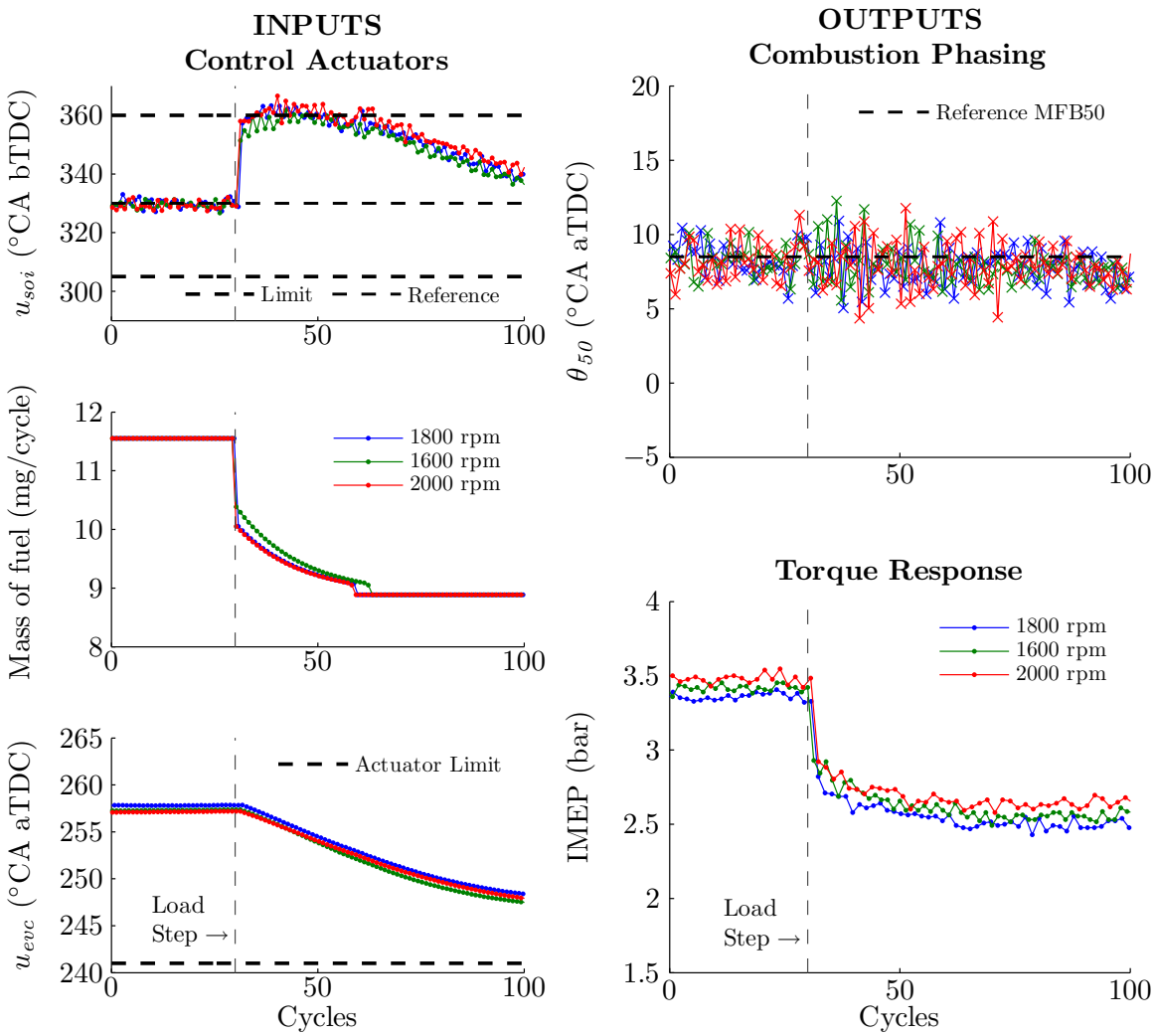

Figure 4.15: Linearized fuel governor – results for different engine speeds.

4.3.4 Comparing Nonlinear and Linearized Fuel Governors

The linearized fuel governor developed in Sec. 4.2.3 aims to improve the computational runtime of the nonlinear fuel governor by linearizing the nonlinear prediction model at a chosen operating point. In Fig. 4.14 the same m_f^{inj} transition from 11.4 to 8.8 mg/cycle is carried out for the nonlinear and the linearized fuel governors. The performance of both governors is very similar. The torque transition is smooth and there are no undue fluctuations in θ_{50} during the transition.

4.3.5 Variation in Engine Speed

As is shown in Sec. 4.4, the linearized fuel governor is very attractive from a computational runtime perspective. It is important to verify that the linearized fuel governor performs well for a range of speeds and loads. The same m_f^{inj} transition from 11.55 to 8.9 mg/cycle is carried out at 1600 rpm, 1800 rpm, and 2000 rpm, with results presented in Fig. 4.15. The nominal engine speed for the linearized model is 1800 rpm. The governor performs well for this variation in engine speed. The torque steps smoothly from the first operating point to the next, and there are no significant oscillations in the combustion phasing response.

4.4 Experimental Runtime Considerations

All fuel governor variants presented in this dissertation run in real-time. However, the nonlinear fuel governor can be computationally expensive. The optimization of β in Eq. (4.18) must be run in real-time four times a cycle, to determine the m_f^{inj} input for every cylinder. Depending on the values of the time horizon N, and the convergence tolerance ϵ, the nonlinear prediction model may have to be run several thousand times every second. Profiling the nonlinear fuel governor determined that the Arrhenius integral from Eq. (3.26) was the most computationally expensive part of the model. Replacing the Arrhenius integral with a lookup table leads to an appreciable runtime improvement. Similarly the cylinder volume calculation is replaced by a lookup table. The linearized fuel governor shows a further drastic reduction in runtime.

Table 4.1 shows the typical maximum runtimes for different control strategies for a standard series of load transitions. The typical additional computational overhead of augmenting the baseline controller with the linearized fuel governor is only 4%. Implementing the linearized fuel governor on less computationally powerful commercial engine control hardware should be feasible, and is planned in future work.

4.5 Summary

The fuel governor control strategy presented in this chapter is proposed as a solution to the load control problem in HCCI. It is shown that the fuel governor can improve combustion phasing and load responses during large load transitions, when the possibility of future actuator constraint violations exists. Further, the fuel governor extends

Control Strategy	**Maximum Runtime**	**Normalized Maximum Runtime**
Nonlinear Fuel Governor (Arrhenius integral)	8.916 ms	7315%
Nonlinear Fuel Governor (lookup table)	2.315 ms	1900%
Linearized Fuel Governor	0.1271 ms	104%
Baseline Controller	0.1219 ms	100%

Table 4.1: Comparison of experimentally recorded maximum runtimes. A standard series of load transitions were run for each control strategy.

the range of load transitions that can be controlled by the baseline controller. The linearized fuel governor is proposed as a computationally efficient variant of the load governor, and is shown to have similar θ_{50} regulation performance as the nonlinear variant. The linearized fuel governor is tested at engine speeds other than the nominal operating speed of the linear model.

Issues with θ_{50} regulation by the fuel governor during late phasing conditions or low load conditions are discussed in Chap. 5. Understanding the nature of the high cyclic variability seen in these conditions allows for the development of an improved load and speed controller in Chap. 6.

Chapter 5

Modeling High Cyclic Variability at Late-Phasing HCCI Conditions

This chapter explores how the magnitude of cyclic variability (CV), as measured by variance of θ_{50}, changes at different HCCI operating conditions, and the the effect that this has on transient θ_{50} control[1]. Experimental evidence of the onset of high CV at different loads, values of θ_{50}, and for different cylinders is presented in Sec. 5.1. The physical phenomena causing the increased cyclic variation is determined in literature to be the presence of significant amounts of unburned and recycled fuel in the NVO region, and these findings are summarized in Sec. 5.2. This understanding is used to analyze heat release data in Sec. 5.3 and link the onset of high cyclic variability with low peak cylinder temperatures. The model of Chap. 3 is augmented with an additional state (mass of unburned fuel) and with NVO heat release in Sec. 5.4. The resulting control-oriented model predicts mean θ_{50} as well as the nature of θ_{50} variability in both low CV and high CV dynamical regions. The discussion is summarized in Sec. 5.5. The CV model and the insights developed in this chapter are used in Chap. 6 to design an improved load and speed transient controller.

5.1 High Cyclic Variability (CV) in HCCI

It is well established in literature, see for example [6, 45, 56, 90–92], that late phasing HCCI combustion dynamics are qualitatively different from the dynamics seen at early to mid combustion phasings. Experimentally observed cyclic variability (CV), as measured by variance of θ_{50}, increases significantly after a certain threshold value of θ_{50}, while combustion stability as well as efficiency drop sharply soon after this threshold, see Fig. 5.1. This threshold value (θ_{50}^{thresh}) varies with engine load and speed,

[1] The author would like to acknowledge the contributions of Jacob Larimore (`larimore@umich.edu`) and Erik Hellström (`erikhe@umich.edu`) to the work presented in this chapter.

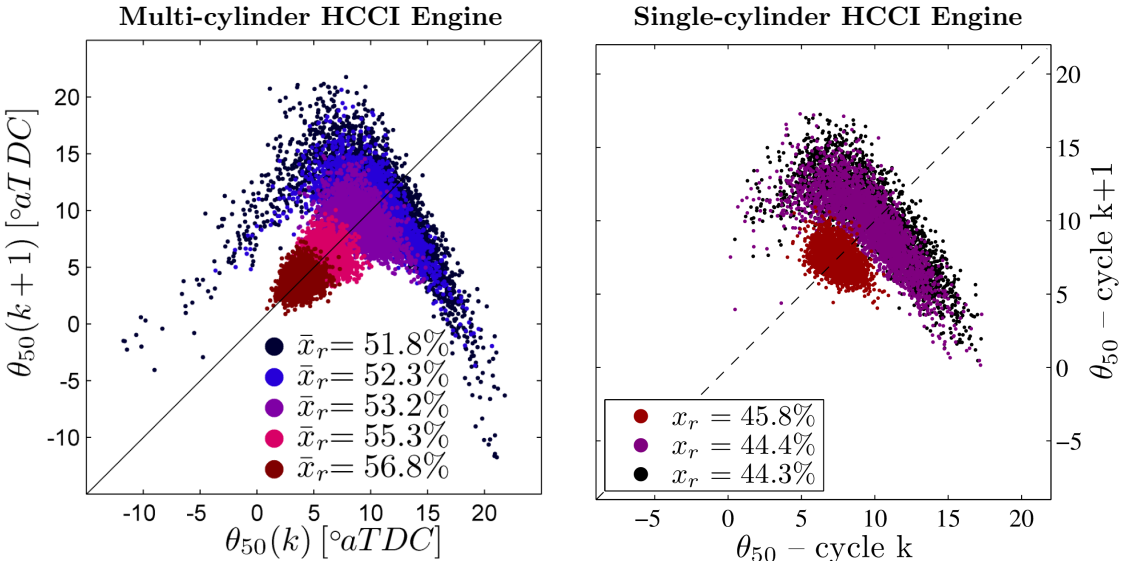

Figure 5.1: Return maps from both multi-cylinder and single-cylinder HCCI engines of measured θ_{50} for operating conditions that differ only in the value of NVO. Smaller NVO values are associated with lower residual gas fractions, later phasing, and high CV. Adapted from [4, 5].

and divides the HCCI operation into two dynamically distinct regions – a late phasing, high CV region and a normal phasing, stable region.

Characterizing and understanding this increased θ_{50} CV is important as steady state controllers designed to regulate combustion phasing in the late phasing high CV region have been shown to be destabilizing in the normal phasing stable regions, and vice-versa, see for example [5, 92, 93]. This fact is also demonstrated analytically in the current application, see Sec. 6.1.3. Hence it is important for the controller to know the current nature of the combustion dynamics while determining the control input to be applied in the next cycle. This is especially important during HCCI transitions, as transient combustion phasing variation can cause the cylinder combustion to switch between the high CV and low CV regions, even if the two steady-state end points of the transition exist in the stable low CV region. Incorrectly determining the nature of combustion can limit the magnitude of transitions possible.

5.1.1 High CV at Late Phasing Conditions

As discussed earlier, the magnitude of the CV increases significantly after a threshold value of θ_{50}. The onset of the high CV region is depicted in Fig. 5.1 for both single cylinder and multi-cylinder HCCI engines. In this experiment, several thousand cycles

of data were recorded at various steady state points. The plots in the figure present θ_{50} return maps for the datapoints that are recorded at the same load and speed, and only vary in the value of NVO. The return maps depict couplings between cycles by representing how the value of θ_{50} at cycle (k) depends on the value of θ_{50} at cycle (k-1). A return map that is tightly clustered around the mean on the diagonal suggests low CV system dynamics that have been perturbed by noise, while a return map with a distinct shape suggests deterministic relationships between cycles. Thus from Fig. 5.1 one can see that the level of CV increases sharply as the NVO is reduced, and θ_{50} is phased later.

5.1.2 Cylinder to Cylinder Variation at Low Load Conditions

It is observed that the fuel governor displays significant cylinder-to-cylinder variation for some load transitions. An example of this is seen in Fig. 5.2, which shows the nonlinear fuel governor response of different cylinders for the same load step down studied in Fig. 4.10. It illustrates that while the transient response of some cylinders can be excellent, other cylinders sometimes exhibit high cyclic variability in θ_{50}. The initial IMEP and θ_{50} response just after the load transition is satisfactory for both cylinders, which indicates that the fuel governor improves transition performance for all cylinders. However, a few cycles after the load transition, the θ_{50} of cylinder 3 enters an oscillatory region, causing noticeable dips in IMEP.

This behavior is attributed to the baseline controller applying destabilizing control to cylinder 3 at low IMEP conditions. As shown in [3, 45], late phasing HCCI combustion dynamics are oscillatory. The onset of the oscillatory dynamics varies with load and with cylinder, as seen in Fig. 5.2. During this load transition, cylinder 3 enters the oscillatory region while cylinder 2 does not. As seen in [94], gains designed for stable HCCI dynamics are destabilizing when applied in the oscillatory region. Thus the performance gains of the fuel governor can be further improved with a baseline controller that globally stabilizes the engine phasing. It is important to predict the onset of the cyclic variability (CV) associated with these oscillatory dynamics, and develop controllers for it.

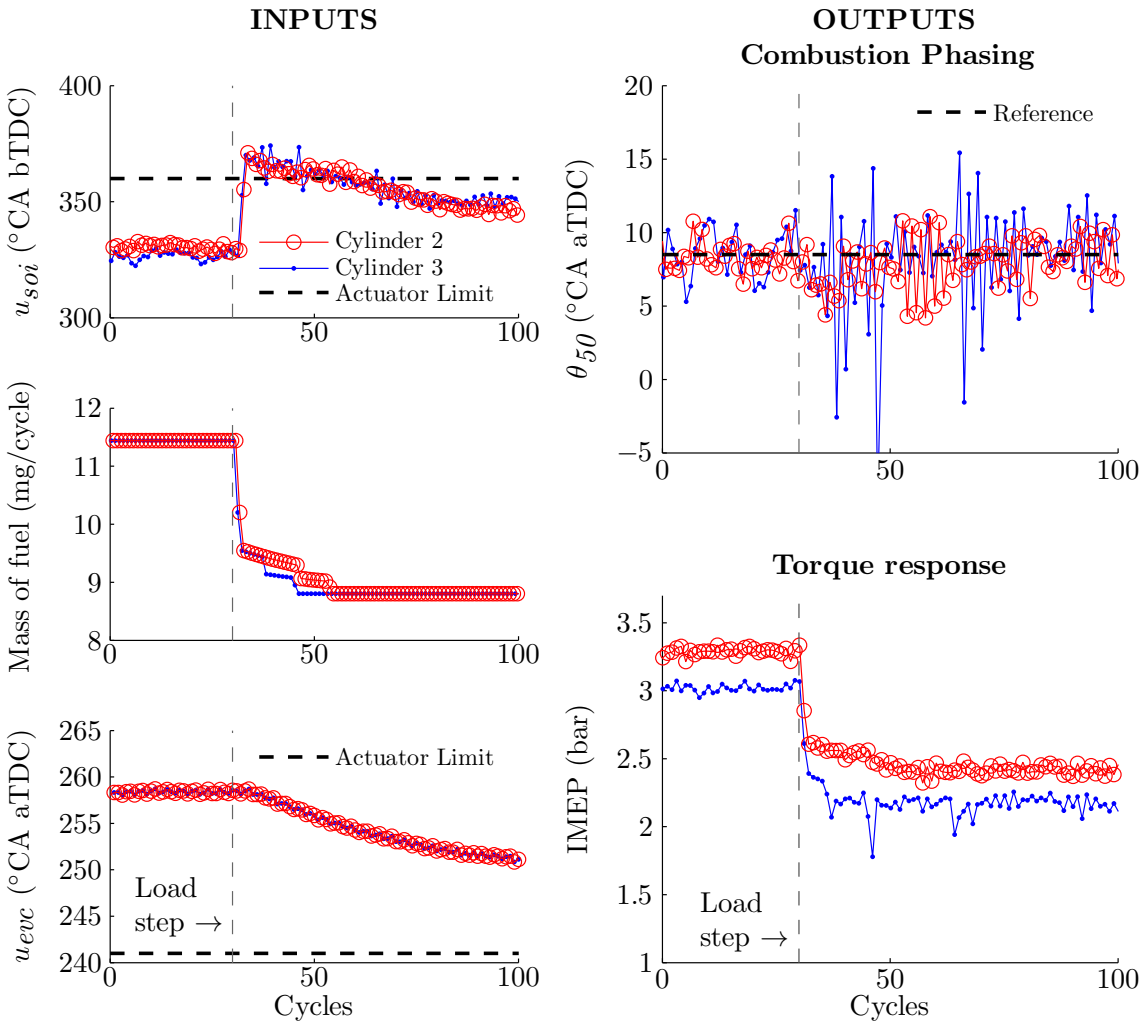

Figure 5.2: Nonlinear fuel governor – differences between cylinders. A few cycles after the load transition, the θ_{50} of cylinder 3 enters an oscillatory region, causing noticeable fluctuations in IMEP.

5.2 Physical Cause of High CV HCCI Dynamics

In low-order control-oriented HCCI models, see for example [5, 56, 92, 93], the high CV dynamic behavior at late-phasings manifests itself as a negative discrete eigenvalue, which is associated with oscillatory dynamics. Researchers differ on the physical explanation for this negative eigenvalue. Chiang et al. [56] demonstrated that a single temperature state can model the existence of multiple equilibria for rebreathing HCCI through a bowl-shaped $T_{ivc} - T_{bd}$ combustion curve. Later, similar analysis was performed by Liao et al. [92] for recompression HCCI, where they hypothesize that the negative eigenvalue is caused by increased heat transfer around TDC.

While heat transfer may be a factor, experimental and modeling works by Koopmans et al. [95], by Wagner et al. [90, 96] and by Hellström et al. [3, 4] suggest that heat release during the NVO region resulting from unburned fuel dynamics is the primary cause of increased late-phasing oscillations seen in autoignition combustion modes. Through the use of statistical analysis tools in [3, 4], it is shown that incomplete combustion during the main combustion event leads to a secondary heat release during the NVO region that sets up the characteristic late-early-late oscillatory behavior seen in both single-cylinder and multi-cylinder recompression HCCI engines.

A experimental demonstration of the heat release during NVO due to unburned fuel is seen in Fig. 5.3, which compares the measured pressure traces and heat release analysis results for two steady state HCCI operating points. These points only differ in the u_{evc} position, with all other actuators kept constant. The figure presents 3000 engine cycles of data measured at each operating point. The point with the later u_{evc} has a lower estimated residual gas fraction of about 5%. The resulting lower charge temperatures, and later combustion phasings push this point into the high CV region. The increase in θ_{50} variance can be clearly seen in the figure. It is observed that cycles with extremely late θ_{50} demonstrate poor main combustion efficiency and low heat release during main combustion. These specific engine cycles show clearly observable heat release behavior in the NVO region. Since the NVO heat release occurs before the fuel injection event, this demonstrates that unburned fuel in the recycled charge both exists and participates in exothermic reactions. The increased temperature of the retained charge leads to very early phasing for the subsequent combustion, thus setting up an oscillatory late-early-late behavior. For more detailed analysis, refer to [6, 45].

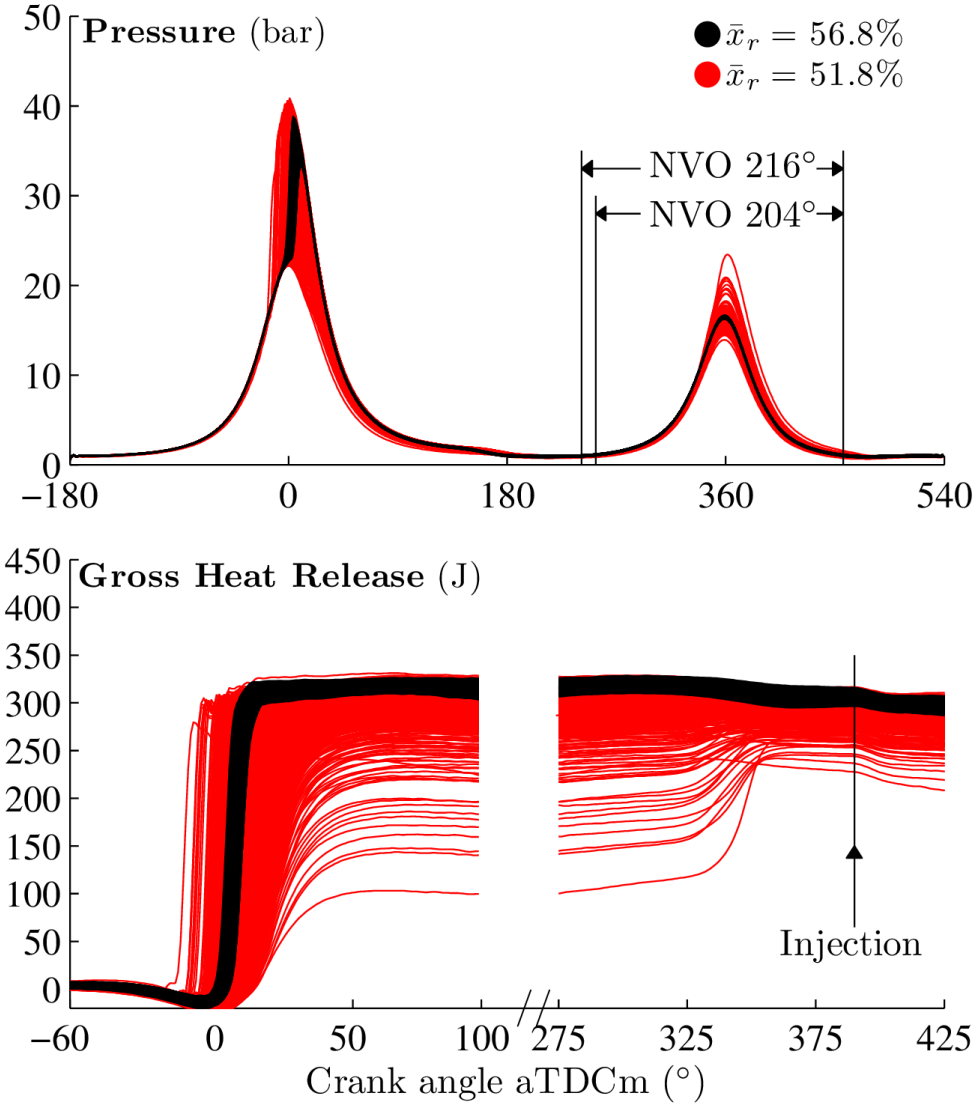

Figure 5.3: Comparison of pressure and gross heat release traces for a low CV and high CV NVO heat release and unburned fuel for late-phasing HCCI.

5.3 Predicting Mass of Unburned Fuel

The primary cause of the late-phasing oscillatory behavior is thus understood to be unburned fuel dynamics, which manifests itself through secondary thermal effects observed in [56, 92]. Predicting the presence of unburned fuel mass after main combustion is used as a proxy for determining whether the cylinder combustion is in either the low CV or the high CV region. Heat release analysis of pressure traces from the multicylinder HCCI engine at different fueling levels is presented in Fig. 5.4. In this figure estimated combustion efficiency is plotted versus θ_{50} and estimated peak combustion temperature. Tens of thousands of engine cycles are recorded at several different values of u_{soi} and u_{evc} to get a large spread in θ_{50} at each fueling level. As seen in the figure, the combustion efficiency drops from its nominal value at later phasings – which suggests that incomplete combustion. This leads to increased amounts of unburned fuel after the main combustion event, and the onset of CV.

The onset of high CV occurs at earlier combustion phasings for lower versus higher m_f^{inj} values. An example of this can be seen in the single cylinder experiments presented in Fig. 5.5. This effect can be explained by the peak combustion temperature in the cylinder falling below 1500 K, a temperature threshold below which the CO to CO_2 conversion efficiency is known to drop significantly, see [97]. At lower m_f^{inj} values this threshold temperature is reached at earlier combustion phasings, and hence the onset of CV occurs at earlier θ_{50} values. Note that temperatures presented in Fig. 5.4 are estimates from the heat release analysis, as the actual in-cylinder temperature cannot be measured. Further, the estimated temperature is a mean cylinder temperature that averages temperature gradients caused by phenomena such as inhomogeneous mixing and increased heat transfer near cylinder walls and crevices. These uncertainties, assumptions and noise lead to a spread in the estimated peak combustion temperature threshold below which the combustion efficiency drops.

The data fits presented in Fig. 5.4 are sigmoids, of the following form:

$$y = \frac{a_1\left(m_f^{inj}\right)}{1 + \exp\left\{\frac{x - a_2\left(m_f^{inj}\right)}{a_3}\right\}} \tag{5.1}$$

where a_i, $i \in \{1, \ldots 3\}$ are parameters. Note that the shape parameter a_3 was kept constant for both fueling levels.

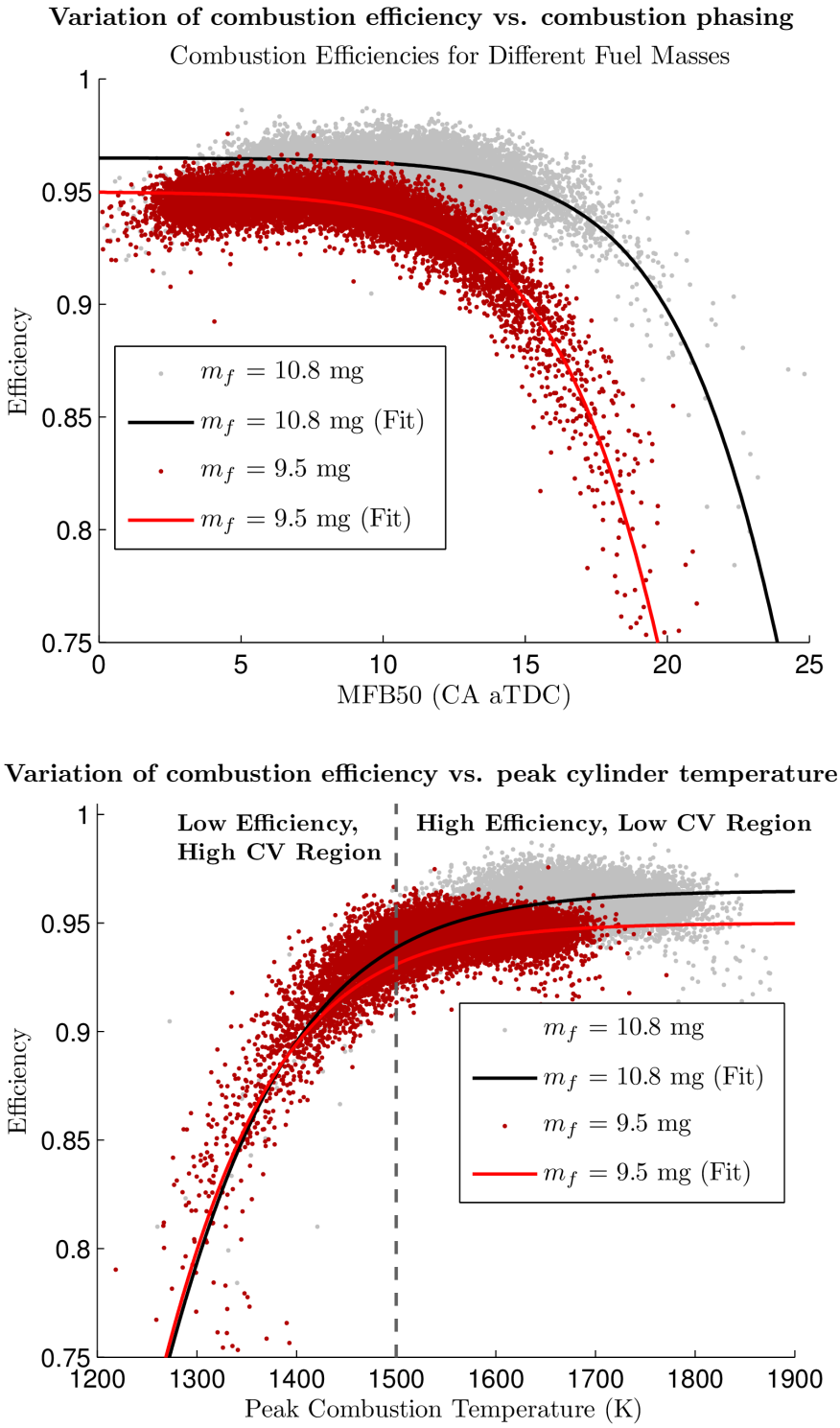

Figure 5.4: Estimated combustion efficiency at two fueling levels, plotted versus combustion phasing and peak cylinder temperature. Low peak combustion temperature $\Longrightarrow$ Low combustion efficiency $\Longrightarrow$ Significant amounts of unburned recycled fuel. The curve fits are sigmoids, similar to Eq. (3.16).

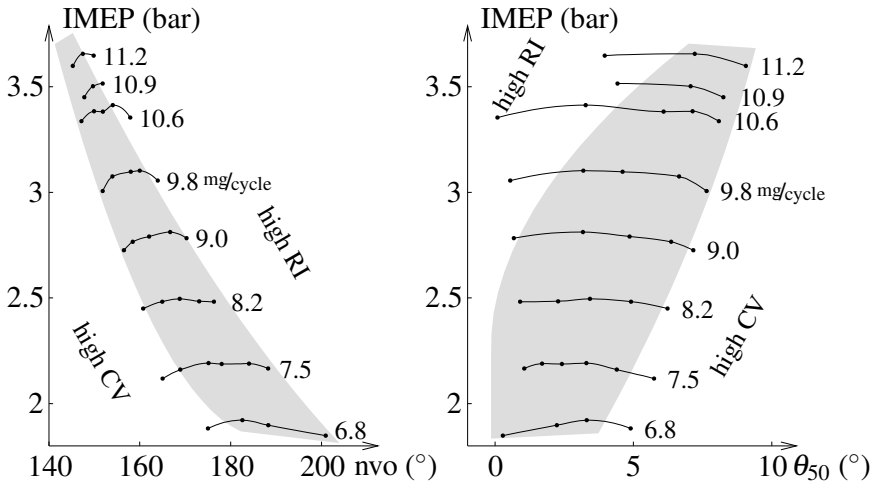

Figure 5.5: Single cylinder engine experiments for the usable HCCI operating region at 2000 rpm. The acceptable combustion phasing range, represented by θ_{50}, is limited by ringing intensity (RI) and cyclic variability (CV) constraints. Adapted from [6, 7].

5.4 Modeling Onset of High CV Dynamics

The insights into the nature and cause of high CV dynamics in HCCI combustion can be used to develop a control-oriented, low-order model that predicts HCCI combustion behavior in both the low CV and the high CV regions. Predicting the change in HCCI dynamics from damped to oscillatory is of specific interest. An example of such a model is presented in this section, along with validation results. The model is based on the low CV model presented in Chap. 3, and is augmented with NVO heat release following a low efficiency burn, similar to models for single operating points presented in [6, 45]. The novelty of the work presented here is that the model is, to the best of the author's knowledge, the first HCCI combustion model that predicts predicts the nature and magnitude of CV in both low CV and high CV regions.

5.4.1 CV Model Equations

The CV model augments the model discussed in Chap. 3. Only the equations that change are presented in this section. The summary of all changes made to convert the model of Chap. 3 to the high CV capable model is as follows:

1. As suggested by heat release analysis, linear dependence on m_f^{inj} is introduced in two parameters in the combustion efficiency regression.
2. The mass of unburned fuel (m_f^{ub}) as a result of inefficient combustion, and the subsequent mass of recycled fuel in the NVO region (m_f^{res}) are calculated.
3. An extra state – $m_f^{ub}(k)$ – is introduced to exchange information between

consecutive engine cycles. This state is a unit delay with no dynamics.

4. A extra parameter (μ) is introduced and tuned to scale the heat release during NVO due to combustion of the recycled fuel.

These changes are discussed in detail in this section.

Combustion Efficiency

The combustion efficiency is lowered when the peak cylinder temperature falls below the threshold value needed to complete the $CO \rightarrow CO_2$ conversion reaction. This peak cylinder threshold is difficult to estimate on-line, and is hence correlated to θ_{50}, which is calculated on-line. Thus, the onset of high CV is predicted to occur when the combustion phasing is later than a threshold value (θ_{50}^{thresh}), which varies as a function of load and cylinder.

Based on the heat release analysis results presented in Fig. 5.4, the parameters β_1 and β_2 in the combustion efficiency regression of Eq. (3.16) are modified to be linear functions of m_f^{inj}, as follows:

$$\eta_m(k) = \frac{\beta_1\left(m_f^{inj}\right)}{1 + \exp\left\{\frac{\theta_{50}(k) - \beta_2\left(m_f^{inj}\right)}{\beta_3}\right\}} \tag{5.2}$$

where,

$$\beta_1\left(m_f^{inj}\right) = \beta_{1a} + \beta_{1b} m_f^{inj} \tag{5.3}$$

$$\beta_2\left(m_f^{inj}\right) = \beta_{2a} + \beta_{2b} m_f^{inj} \tag{5.4}$$

This increases the number of model parameters by 2. However all of β_x, $x \in \{1a, 1b, 2a, 2b, 3\}$, are obtained from experimental data, and can be seen in Fig. 5.4. The shape parameter β_3 is kept constant.

Unburned and Recycled Fuel

The onset of high CV in HCCI combustion is understood to be caused by the presence of significant amounts of unburned fuel after main combustion, which leads to heat release in the NVO region. The unburned fuel after main combustion (m_f^{ub}) is

calculated as follows:

$$m_f^{ub}(k+1) = (1-\eta_m(k))\, m_f^{inj}(k) \tag{5.5}$$

$$\approx 1 - \frac{\beta_1}{1+\exp\left\{\frac{\theta_{50}(k)-\beta_2\left(m_f^{inj}(k)\right)}{\beta_3}\right\}} m_f^{inj}(k) \tag{5.6}$$

Note the approximation made in Eq. (5.6). The numerator (β_1) is assumed to be constant and independent of the mass of fuel (m_f^{inj}). This helps the fit of the model.

The unburned fuel is assumed to be uniformly distributed in the exhaust gases. Some of it is exhausted during the exhaust valve open period, while an x_r fraction of it is retained in the NVO region. Hence the residual mass of fuel that is recycled in the recompression region (m_f^{res}) is given by:

$$m_f^{res}(k) = x_r m_f^{ub}(k) \tag{5.7}$$

Some of the recycled fuel, given by the fraction η_r, exothermically reacts during recompression. The resultant heat release is modeled by adding a NVO heat release term ($\Delta T_{NVO,HR}$) at u_{evc} to the thermal coupling equation of Eq. (3.8):

$$\begin{aligned} T_{evc}(k) &= c_e T_{bd}(k) + \Delta T_{NVO,HR} \\ &= c_e T_{bd}(k) + \frac{\eta_r\, q_{lhv}}{c_v m_c^{nvo}} m_f^{res}(k) \\ &= c_e T_{bd}(k) + \frac{\eta_r\, q_{lhv}}{c_v p_{em} V_{evc}} R T_{evc} m_f^{res}(k) \\ &= c_e T_{bd}(k) \left(1 + \eta_r \mu \frac{x_r m_f^{ub}(k)}{p_{em} V_{evc}}\right) \end{aligned} \tag{5.8}$$

Here μ is the single scaling parameter that is tuned to obtain the validation results presented in this chapter. The mass of charge in the NVO region (m_c^{nvo}) is evaluated using the ideal gas law at u_{evc}. The efficiency of burn during NVO is assumed to be 100%, which is supported by the vast majority of the heat release traces recorded on the experimental multicylinder engine. An example of this is seen through the pressure traces of the high CV case in Fig. 5.3. If the efficiency of burn during NVO were substantially less than 100%, then the heat release during the main combustion event of the subsequent early phasing cycle would be noticeably larger than the mass of injected fuel times the lower heating value of the fuel ($m_f^{inj} \cdot q_{lhv}$). This is seen in the figure not to be the case. Note however, that single cylinder HCCI experiments

suggest that η_r can be less than 100% for other experimental setups, see [6].

Third Discrete State – Mass of Unburned Fuel (m_f^{ub})

Finally, note the introduction of a new discrete state – the mass of unburned fuel (m_f^{ub}). Low combustion efficiency in cycle (k) leads to NVO heat release in cycle ($k+1$), and the new state facilitates information exchange between cycles. Since all recycled fuel is assumed to burn in the NVO region, this new state is a unit delay with no dynamics, and it shows up in pole-zero maps as a pole at origin. Some HCCI models in literature define engine cycles to begin at u_{ivc}. In these cases, the mass of unburned fuel would not be a state.

5.4.2 CV Model Validation

Model predictions from the CV model are compared to experimental results, with the model being evaluated for the following criteria:

1. Prediction of mean θ_{50} in both low CV and high CV regions.
2. Prediction of the onset of high CV during an actuator sweep, where one actuator, say u_{evc}, is varied while keeping all other actuators constant.
3. Verification of these results at different loads and speeds.

Return Maps Comparison during u_{evc} Sweep

HCCI combustion demonstrates a non-zero level of variability, even if all control actuators are kept fixed. An underlying level of stochastic disturbances and measurement noise always exist, even in the low CV dynamical region. In addition to the ignition event itself being stochastic, at steady state conditions the air flow through the cylinders can vary slightly from cycle to cycle, which results in variations in mass of residuals, the charge temperature and the charge composition. Indeed, these variations are more pronounced in the high CV region, where the combustion dynamics are closer to instability and hence more sensitive to external disturbances.

These stochastic disturbances can be simulated by augmenting the residual gas fraction regression given by Eq. (3.2) with an additive factor (Δx_r) as follows:

$$x_r(k) = \left[1 - (\alpha_0 + \alpha_1 u_{evc})\,\Pi^{\alpha_2} T_{bd}(k)^{\alpha_3} \omega(k)^{\alpha_4}\right] + \Delta x_r \tag{5.9}$$

Following the methodology outlined in [4, 6], Δx_r is modeled to be zero-mean Gaus-

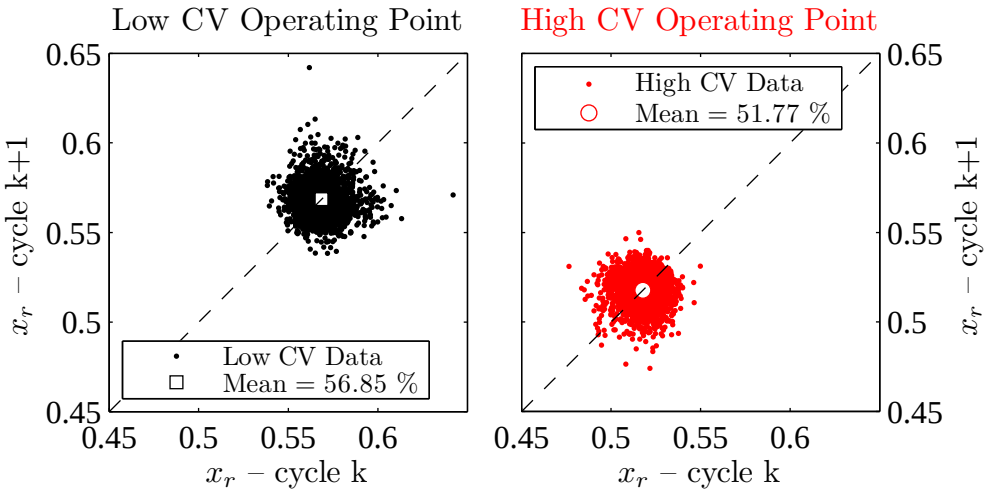

Figure 5.6: Cycle-by-cycle residual gas fractions are estimated from experimental data, and are compared using return maps. Here 3000 engine cycles are measured at each operating point.

sian noise. This is a reasonable assumption, as seen in Fig. 5.6 which compares the estimated residual gas fractions for a low CV operating point (higher x_r) and a high CV operating point (lower x_r)[2]. Each plot is obtained by processing 3000 cycles of experimental measurements. The figure visualizes the time series data in terms of return maps. Return maps or lag-1 maps are graphical tools useful in studying how a discrete variable evolves between time-steps. In the current application, the return map shows the relationship between consecutive values of the combustion phasing θ_{50}. Return maps reveal low-order deterministic features even when these are nonlinear [45]. An asymmetric pattern implies an asymmetry in time which means that the evolution of θ_{50} is due to nonlinear dynamics or non-Gaussian noise, or both [45, 98]. The symmetrical patterns in Fig. 5.6 suggest that the additive x_r noise is Gaussian.

Modeling the Gaussian additive x_r noise in this manner allows the comparison between experimental results and the model presented in Fig. 5.7. In this experiment, u_{evc} sweeps at two fueling levels were carried out – a sweep at $m_f^{inj} = 10.8\,\text{mg}$ to the left of the figure, and a sweep at $m_f^{inj} = 9.5\,\text{mg}$ to the right. Each sweep consists of five operating points. The u_{evc} is swept from an early position to a late position, and consequently the nature of the combustion transitions from a low CV dynamical region to a high CV dynamical region. The standard deviation of the Gaussian x_r additive noise was tuned so that the standard deviations of the experimental and modeled θ_{50} plots are similar. Each experiment and simulation was run for 3000 engine cycles to

[2]The numerical values of the estimated x_r are post-processed via heat release analysis of the recorded pressure traces. Please refer [6, 45] for details of the heat release algorithm.

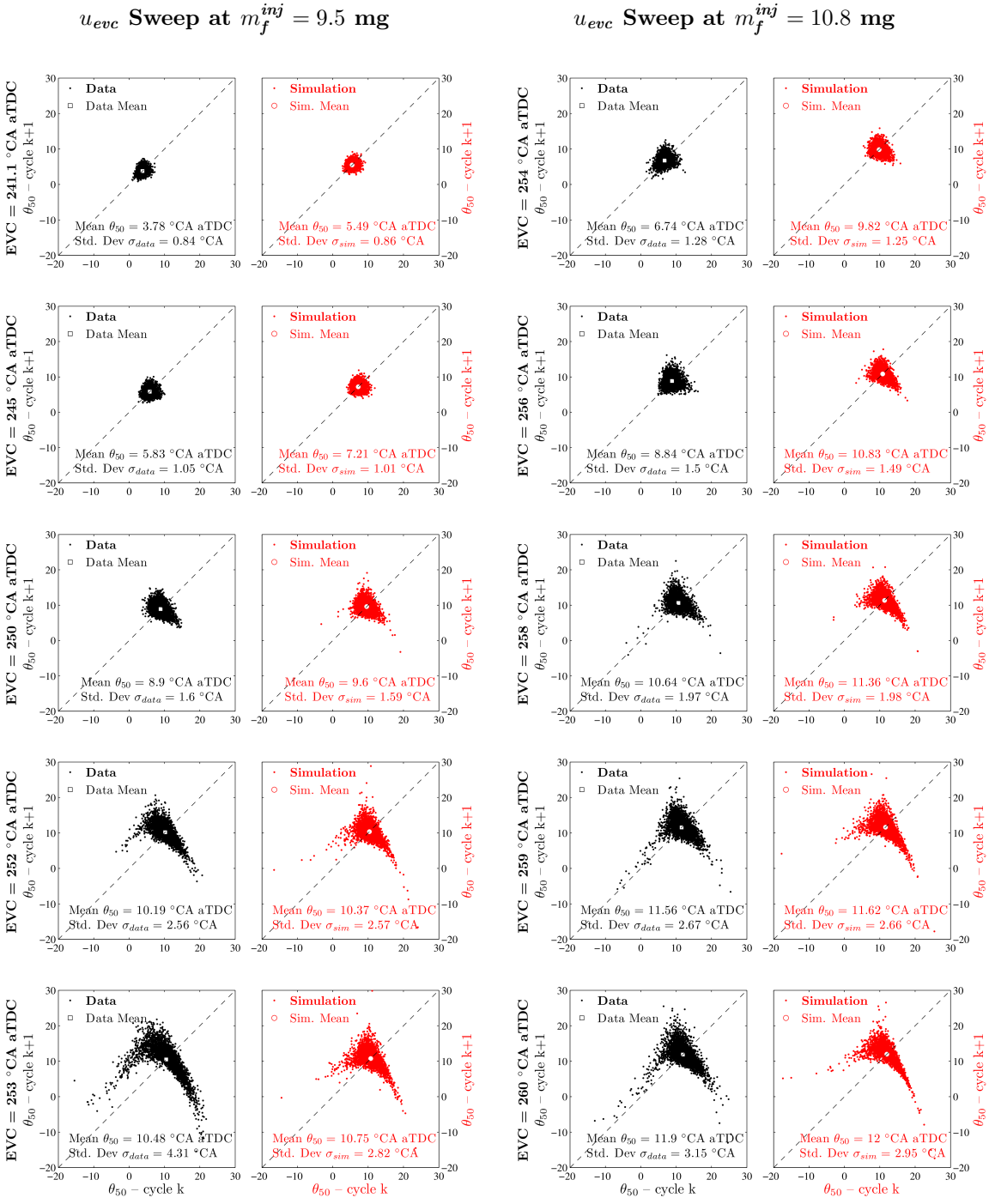

Figure 5.7: Comparison of measured (**black**) and simulated (**red**) combustion phasing (θ_{50}) return maps for u_{evc} sweeps at two fueling levels. Each simulation consists of 3000 engine cycles. The value of u_{soi} is kept constant at 330°CA bTDC. The onset of high CV conditions at late phasing can be seen.

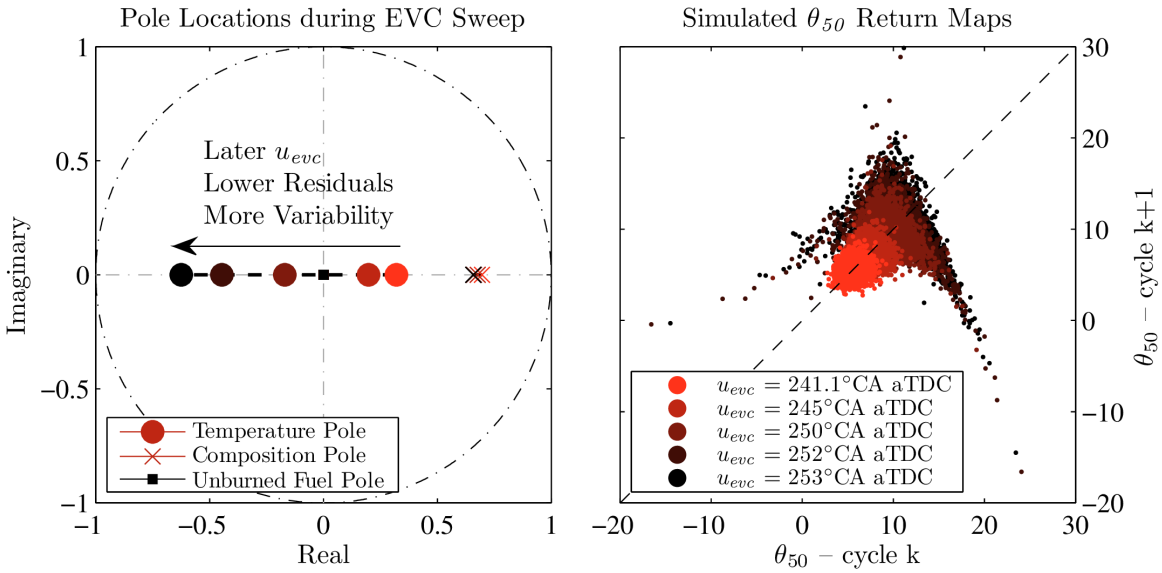

Figure 5.8: A u_{evc} actuator sweep at $m_f^{inj} = 9.5\,\text{mg}$ is visualized through the location of the poles of the linearized CV model (left), and by comparing return maps of the predicted θ_{50} at each operating point. Later u_{evc} values result in lower residuals, oscillatory dynamics, and increased variability.

allow the test to be statistically significant, and to allow deterministic patterns to emerge.

The figure shows that the model can successfully predict the qualitative shape of the return maps, as well as the mean θ_{50}, as the combustion transitions into the high CV dynamical region. Note that the qualitative shape, and not the actual time series, of the modeled and experimental θ_{50} are compared. This is because the actual time series of disturbances to the experiments are unknown. For early values of u_{evc}, both experimentally measured and model predicted θ_{50} return maps resemble Gaussian distributions. As u_{evc} is phased later, the increasing mass of unburned fuel sets up increased variability in the modeled θ_{50} that evolves in deterministically similar patterns to those observed in the measurements.

Onset of High CV Dynamics

The transition from low CV to high CV dynamics can be visualized in Fig. 5.8 which considers the locations of the poles of the linearized model during a u_{evc} actuator sweep. During this sweep all other control actuators are held constant. At each u_{evc} level the nonlinear CV model is linearized and the pole locations are plotted. As

u_{evc} is swept from its early position (here 241.1°CA aTDC) to its late position (here 252°CA aTDC), the discrete temperature eigenvalue moves from the right half plane to the left half plane. This clearly demonstrates how and when the nature of the model's dynamic response switches from damped to oscillatory. The location of the composition eigenvalue does not move much. The location of the third eigenvalue introduced in the CV model is seen to be fixed at origin. This behavior is expected as the m_f^{ub} state is used solely for information exchange between engine cycles, and as such is a unit delay with no dynamics.

The model predictions are also visualized in the return maps plotted to the right of Fig. 5.8. Here the nonlinear model is run at the five operating points that comprise the u_{evc} sweep. Variability is introduced via Gaussian x_r additive noise. Later u_{evc} values result in lower residuals, oscillatory dynamics, and increased variability.

Scope and Limitation of CV Model

The location of the onset of high CV can be described as the operating point in an actuator sweep when the nature of the CV qualitatively transitions from stable and damped to oscillatory. In terms of the model just described, it occurs when the temperature pole transitions to the negative real axis. This location of onset of high CV is very sensitive to environmental conditions and engine ageing. Results can vary from day to day. Hence specifying the exact θ_{50} at which the onset occurs is of limited use. This makes modeling the onset and nature of CV a difficult task. In the current application all validation and parameterization data was taken in a single engine experiment, so that the effect of engine ageing was minimized.

The model introduced in this chapter is relatively simple, with a single scaling parameter (μ) that is tuned to get the results presented here. A more sophisticated modeling of the recompression heat release can be implemented in future work to further improve modeling results. Slowly adapting the value of the scaling parameter over time can be implemented to counteract the effects of engine ageing.

5.5 Summary

Understanding the nature of the increased HCCI cyclic variability at late phasing and low load conditions is seen to be important in controlling HCCI combustion, and in enabling larger transitions in the HCCI operating region.

The onset of high CV in HCCI combustion is understood to be caused by the presence of significant amounts of unburned fuel after main combustion, which leads to heat release in the NVO region. This lowering of combustion efficiency occurs when the peak cylinder temperature falls below the threshold value needed to complete the $CO \rightarrow CO_2$ conversion reaction. This peak cylinder threshold is difficult to estimate on-line, and so is correlated to θ_{50}, which is calculated on-line. Thus, the onset of high CV is predicted to occur when the combustion phasing is later than a threshold value (θ_{50}^{thresh}), which varies as a function of load and cylinder.

The HCCI control-oriented model developed in Chap. 3 is augmented with a more physically-based combustion efficiency regression, and with NVO heat release of the unburned and recycled fuel. These modifications are shown to enable the new CV-capable model of predicting the nature and magnitude of the cyclic variability in both low CV and high CV dynamic regions. It is shown that an actuator sweep can cause a linearized model eigenvalue to transition from the right half plane to the left half plane, thus predicting oscillatory dynamics. These insights and modeling results are used in the next chapter to develop an improved HCCI controller.

Chapter 6

Load & Speed Transition Controller

Figure 6.1 represents the load-speed operating map of the multi-mode combustion engine. The HCCI operating map is seen to be a small subset of the larger SI operating map. Nevertheless, HCCI's fuel economy benefits make maximizing the length of stay in the HCCI region a key practical goal of the control strategy. To ensure this, it is important to demonstrate successful and stable control of HCCI transitions. The inset demonstrates some sample HCCI transitions from an FTP75 drive-cycle simulation presented in [8]. These transitions involve variations in engine load, engine speed or both load and speed. Poor θ_{50} and IMEP tracking during the transitions would require an excessive number of combustion mode switches (HCCI to SI before the transition, and vice-versa after it) to maintain satisfactory performance. The fuel economy penalty associated with combustion mode switches would then reduce the overall efficiency benefit. This chapter presents a control strategy that successfully tracks θ_{50} and IMEP during HCCI transitions.

The chapter is organized as follows. The improved load and speed transient controller is designed in Sec. 6.1. This is an improved version of the baseline controller of Chap. 4. The improvements in the controller are a nonlinear model inversion based u_{soi} feedforward, and a gain scheduled feedback that modifies the control signal depending on the nature of the HCCI dynamics of the previous engine cycle. The CV model developed in Chap. 5 is used to demonstrate the stability of the algorithm within the low CV and high CV regions. It is also used to demonstrate how gain scheduling can improve θ_{50} step responses. Section 6.2 then presents the experimental validation of this control scheme. Successful output tracking is demonstrated for load steps, speed ramps, and simultaneous load and speed transients. Sample transitions with high load slew rates from an FTP75 drive cycle simulation are experimentally tested with the controller.

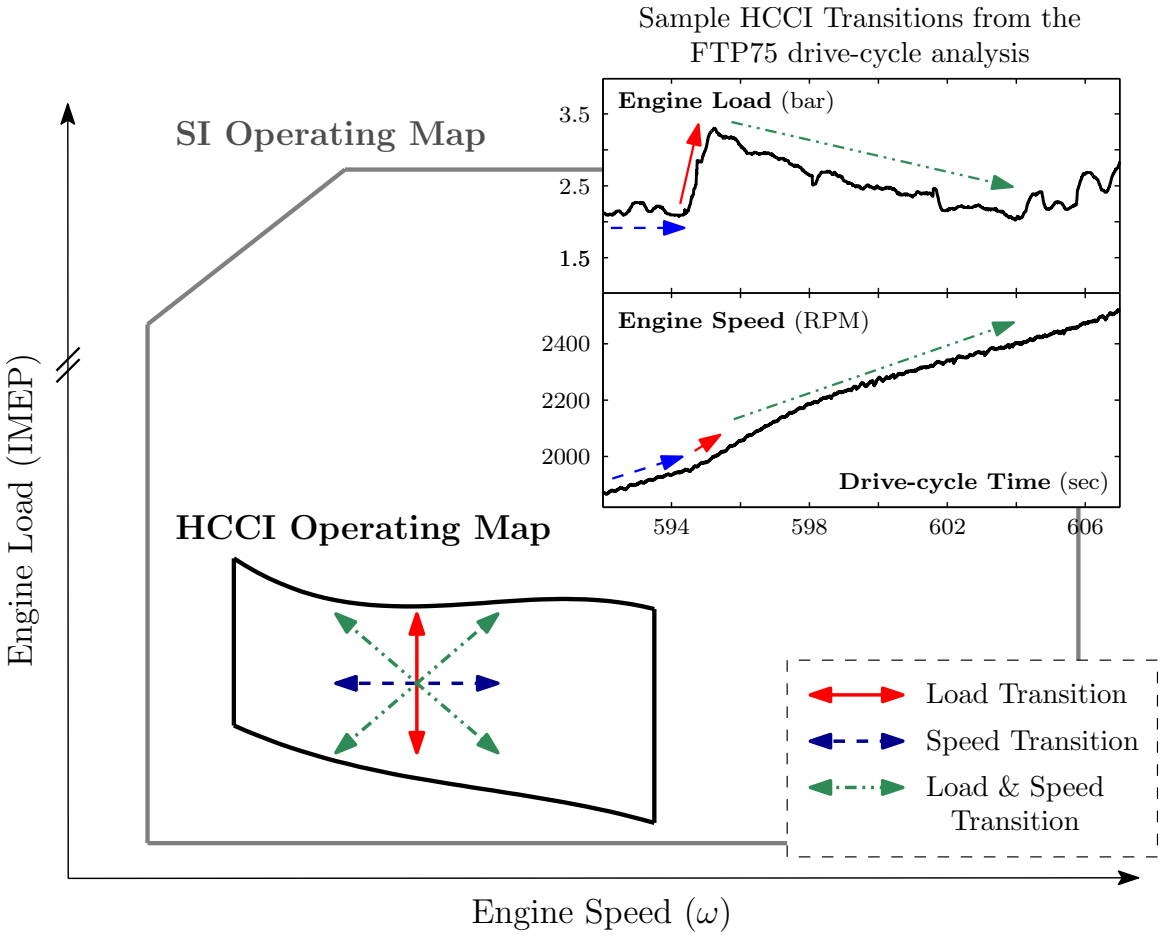

Figure 6.1: Load-Speed operating map of the engine showing HCCI and SI regions with representative HCCI transitions from an FTP75 drive-cycle analysis performed in [8].

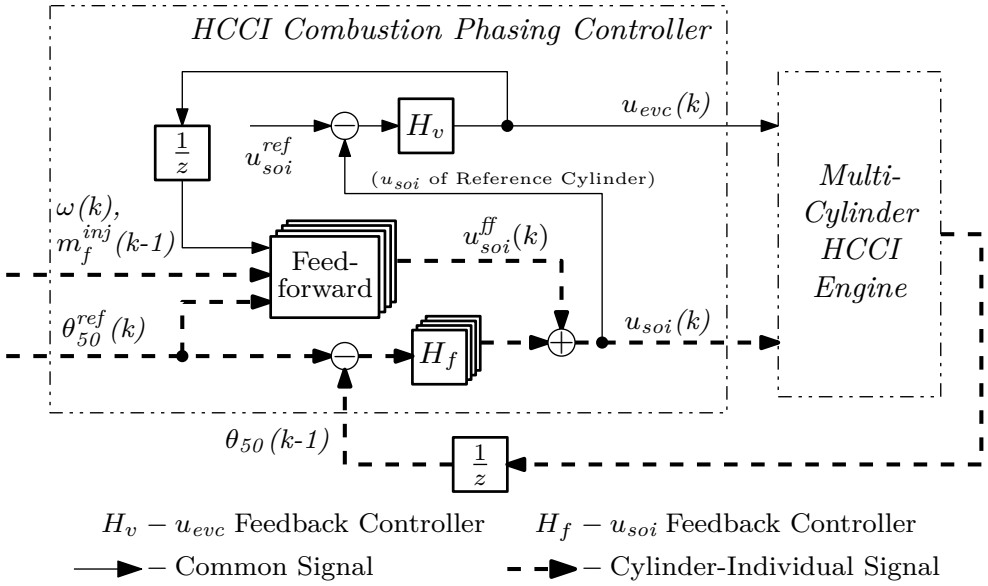

Figure 6.2: Controller architecture – two inputs u_{soi} and u_{evc} in a mid-ranging feedback configuration, with a model-based feedforward for u_{soi}.

6.1 Controller Design

The controller presented in this chapter improves on the baseline controller presented in Chap. 4. The goal of the control strategy is to track combustion phasing (θ_{50}) of the four cylinders to their desired set points (θ_{50}^{ref}) during both transient and steady state HCCI operation. During an HCCI transition, changes in engine load (IMEP), engine speed (ω), and desired combustion phasing (θ_{50}^{ref}) are externally specified. Four values of u_{soi} (one for each cylinder), and a single value of u_{evc} (common for the engine) are generated by the controller. The m_f^{inj} injected in each cylinder is specified as a function of the desired engine load, and is not used for θ_{50} tracking control. Equal masses of fuel are commanded to be injected in each cylinder.

An overview of the controller is presented in Fig. 6.2. The feedback loop consists of two PI controllers arranged in a mid-ranging control configuration. Mid-ranging is a process control technique in which a coarse actuator and a fine actuator are coordinated to control a single feedback output [69]. This two-input single-output control technique is selected considering the relative bandwidths and control authorities of the u_{soi} and u_{evc} actuators. The fine actuator u_{soi} is used to track desired θ_{50}^{ref}, while the coarse actuator u_{evc} is used over a larger time scale to return u_{soi} to its nominal setpoint, about which it has sufficient controller authority in both directions. This architecture has been used in HCCI engine control applications, see for example [34,70]. The controller is augmented with an u_{soi} feedforward component to improve transient

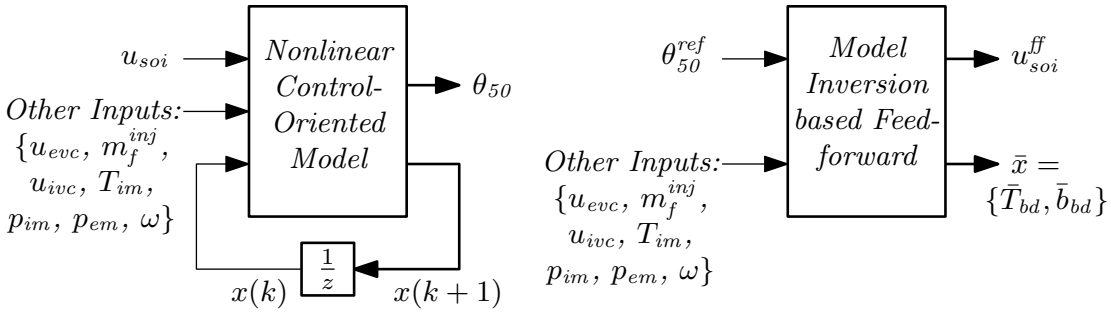

Figure 6.3: The nonlinear control-oriented model is inverted to determine the feedforward component u_{soi}^{ff}.

performance.

As discussed in Chap. 4, the baseline controller does not perform well during large load transitions, even leading to engine misfire in some cases. The performance of the controller is significantly improved in this chapter through two novel contributions – nonlinear-model inversion based u_{soi} feedforward, and gain scheduling u_{soi} feedback. The feedback block aims to detect if the combustion is in a high CV or a low CV region based on predicted unburned fuel mass, and applies a different control signal in each CV region. These novel aspects are discussed in this section.

6.1.1 Nonlinear Model Inversion based SOI Feedforward

HCCI transitions involving changes in desired load, engine speed, or θ_{50}^{ref} can cause significant θ_{50} variations if not correctly compensated for. The feedback loop, by definition, cannot react until atleast one engine cycle after these disturbances occur. In extreme cases, large transitions can cause the engine to misfire. Hence accurate feedforward can improve transient θ_{50} tracking performance during HCCI transitions by applying appropriate compensatory control action before large variations in system states can occur.

The feedforward u_{soi} component (u_{soi}^{ff}) is designed to drive θ_{50} to θ_{50}^{ref} at steady state, if all other inputs to the system stay constant. It is computed by inverting the nonlinear control-oriented model developed in Chap. 3, see Fig. 6.3. Theoretically this provides perfect θ_{50} tracking performance at steady state, in the absence of modeling error or plant ageing.

Inverting Nonlinear State Update Equations

As discussed previously, the nonlinear model is to be be inverted at steady state conditions, i.e. $x(k+1) = x(k) = \overline{x} = \left[\overline{T}_{bd}, \overline{b}_{bd}\right]^T$, with the desired output combustion phasing $\theta_{50} = \theta_{50}^{ref}$. The system equations presented in Sec. 3.7 can be rewritten as:

$$\overline{T}_{bd} = \left(\frac{p_{ivc}}{p_{em}}\right)^{\frac{1-n_c}{n_c}} \left[1 + \frac{\eta_m \, q_{lhv} R m_f^{inj}}{c_v p_{ivc} V_{ivc}} \left(\frac{V_{\overline{50}}}{V_{ivc}}\right)^{n_c-1}\right]^{\frac{1}{n_c}} \overline{T}_{ivc} \tag{6.1}$$

$$\overline{b}_{bd} = \frac{(\,AFR_s + 1)\, R m_f^{inj}}{p_{ivc} V_{ivc}\,(1 - x_r)} \overline{T}_{ivc} \tag{6.2}$$

$$x_r = 1 - (a_1 + a_2 u_{evc}) \left(\frac{p_{im}}{p_{em}}\right)^{a_3} \omega^{a_5} \overline{T}_{bd}^{a_4} \tag{6.3}$$

$$c_v = 1 + \alpha_1 x_r \overline{b}_{bd} \tag{6.4}$$

$$\overline{T}_{ivc} = x_r \alpha_2 \left(\frac{V_{evc}}{V_{ivc}}\right)^{n_c-1} \overline{T}_{bd} + (1 - x_r)\, T_{im}, \tag{6.5}$$

where $\overline{T}_{ivc}$ is the temperature at u_{ivc} at steady state, and $V_{\overline{50}}$ is the cylinder volume at the desired θ_{50}^{ref}. The system of equations (6.1)–(6.5) is solved using fixed point iteration. The resulting value of $\overline{T}_{ivc}$ is used along with the reference combustion phasing θ_{50}^{ref} in Eq. (3.26) and (3.29) to determine the desired u_{soi} feedforward component.

Improvement over Baseline Controller

In the baseline control strategy presented in Chap. 4, u_{soi}^{ff} is determined by inverting the model linearized around a typical operating point. This linearization approximation introduces errors that reduce the accuracy of u_{soi}^{ff}, especially if the system is far away from the linearization point. To compensate for these errors the controller relies more heavily on the feedback u_{soi} component, which reduces the utility of the feedforward during transients. The control strategy presented here improves the accuracy of the model-based feedforward by inverting the nonlinear model, thus avoiding errors caused by the linearization approximation. As seen in Sec. 6.1.1, the strategy presented here uses additional measured information $(p_{im}, p_{em}, u_{ivc}, T_{im})$ to generate a more accurate feedforward component.

The two feedforward strategies (the nonlinear and linear model inversion based feedforwards) are compared in Fig. 6.4. The simulation compares the u_{soi} response of the controllers to a m_f^{inj} step and a θ_{50}^{ref} step. It is seen that the combustion phasing and total u_{soi} responses are fairly similar, and both controllers demonstrate

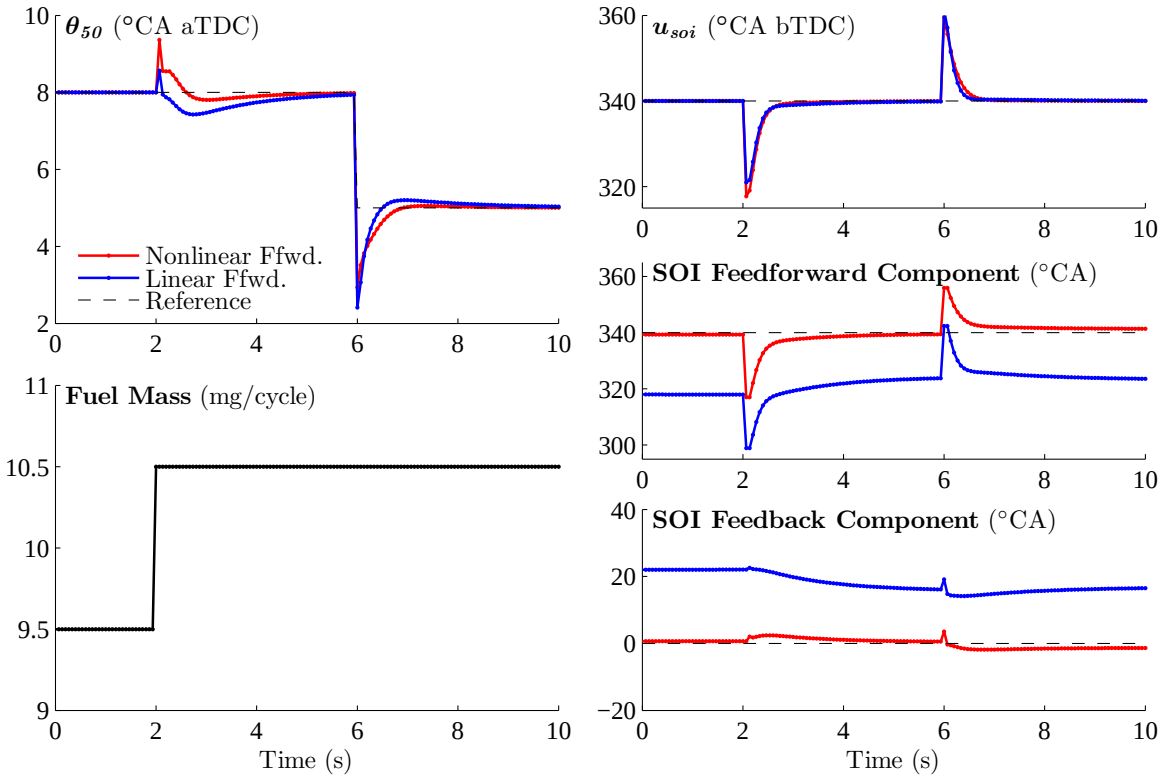

Figure 6.4: Comparing nonlinear and linear model inversion based feedforward in simulation. The feedforward component u_{soi}^{ff} in the nonlinear feedforward is much more accurate, and requires very little feedback correction.

satisfactory θ_{50}^{ref} tracking performance. The overshoots in θ_{50} for both strategies are acceptable. However, the feedforward component (u_{soi}^{ff}) generated by the nonlinear model inversion based feedforward is seen to be much more accurate. Since

$$u_{soi} = u_{soi}^{ff} + u_{soi}^{fb},$$

it also requires very little feedback correction. Given an exact model of the system, the feedback correction will be zero at steady state. Due to linearization errors, the linearized model inversion based feedforward is inaccurate, and the baseline control strategy of Chap. 4 has to rely more heavily on feedback to generate the correct value of u_{soi}. Note that the accuracy of the nonlinear feedforward is directly related to the accuracy of the underlying nonlinear combustion model.

6.1.2 Feedback Controller Design

As discussed in Chap. 5, late phasing and low load HCCI combustion dynamics are oscillatory, and this manifests itself in control-oriented models as a negative eigenvalue. The cylinder combustion is determined to be in the high CV oscillatory region if the existence of a significant amount of unburned fuel, and thus low combustion efficiency, are predicted. This is modeled to happen if the combustion phasing θ_{50} is later than a threshold combustion phasing value (θ_{50}^{thresh}). Further, θ_{50}^{thresh} varies with engine load or m_f^{inj}, but can be modeled to be constant across engine operating conditions for simplicity.

The proportional gain K_p^{soi} of the u_{soi} PI controller (H_f in Fig. 6.2) is gain scheduled, based on whether the controller decides that the system is in the high CV or low CV region:

$$K_p^{soi} = \begin{cases} K_{p,lowcv}^{soi} & \text{if } \theta_{50}(k) \leq \theta_{50}^{thresh}(m_f^{inj}) \\ K_{p,highcv}^{soi} & \text{if } \theta_{50}(k) > \theta_{50}^{thresh}(m_f^{inj}). \end{cases} \tag{6.6}$$

The values of the proportional gains ($K_{p,lowcv}^{soi}$ and $K_{p,highcv}^{soi}$) were determined from prior control design work done in the University of Michigan Powertrain Control Laboratory for the low CV region in [99] and for the high CV region in [5]. $K_{p,lowcv}^{soi}$ was determined through a nonlinear least-squares optimization of the closed loop system in simulation, as described in Sec. 4.1.1. $K_{p,highcv}^{soi}$ was determined through a pole placement analysis using a nonlinear high CV model. It is important to note

that $K^{soi}_{p,lowcv}$ and $K^{soi}_{p,highcv}$ have opposite signs, due to the presence of the negative eigenvalue in the high CV region. The integral gain K^{soi}_{i} of the u_{soi} PI controller was kept constant. The coarse actuator u_{evc} is controlled by a slow integrator (H_v in Fig. 6.2) over a larger time scale to return u_{soi} to its setpoint.

A similar switching concept is used in the controller design by Liao et al. in [92] and is used to track steps in desired θ^{ref}_{50} at a single load-speed HCCI operating point. However, as discussed in Sec. 5.2, unburned fuel heat release, and not increased heat transfer around TDC, is the primary physical phenomenon that determines the magnitude and dynamic evolution of highly variable late phasing HCCI. A correct understanding of the underlying physical phenomena is crucial to design model-based controllers that work over the entire engine operating range. Indeed, the controller presented here is shown to work for multiple load-speed transitions, as opposed to the validation results presented at a single load-speed operating point in [92].

Experimental Validation of Gain Scheduled Feedback

Experimental demonstrations of the benefits of the gain scheduled u_{soi} feedback are presented in Fig. 6.5 and Fig. 6.6. These figures compare the performance of the control architecture presented in Fig. 6.2 with fixed gain and with gain scheduled u_{soi} feedback for both transient and steady state operation respectively. Figure 6.5 compares the transient θ_{50} and load tracking performance during a load step down from $m^{inj}_{f} = 10.4$ mg to 8.7 mg. The value of θ^{thresh}_{50} is 10 °CA aTDC. As can be seen, the initial transient response of the controller with the gain scheduled feedback is significantly smoother. The IMEP steps between the initial and final values in a single cycle, and an engine misfire is prevented. At the lower load level the cylinder combustion dynamics enter the high CV, oscillatory region. The fixed gain feedback controller is unable to regulate θ_{50} well. A typical pattern is noted where the magnitude of oscillations are amplified by the controller before returning to the desired value, and starting up again. These oscillations are also associated with undesired fluctuations in the torque output. This oscillatory behavior is successfully attenuated by the gain scheduling controller. Note that the gain scheduling controller only switches gains when the value of θ_{50} is later than the desired threshold θ^{thresh}_{50}.

Figure 6.6 compares the fixed gain and the gain scheduled feedback blocks' performance for steady state conditions. In this figure each controller was run for over a thousand engine cycles at two different engine speeds, while it attempted to regulate the combustion phasing to a fixed value. The figure visualizes the time series data in

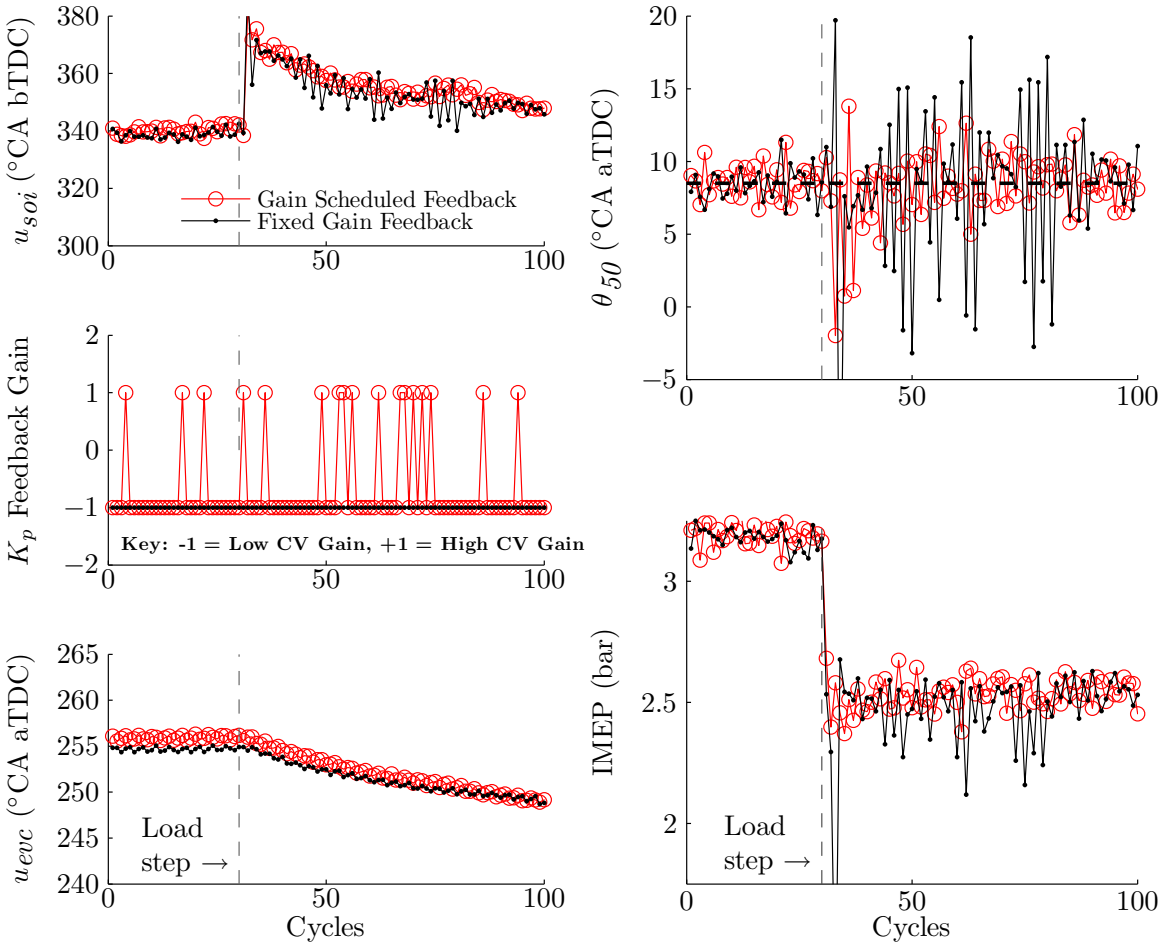

Figure 6.5: Comparison of gain scheduled feedback with fixed gain feedback. Transient response to load step down ($m_f^{inj} = 10.4$ mg $\rightarrow$ 8.7 mg), with $\theta_{50}^{thresh} = 10$°CA.

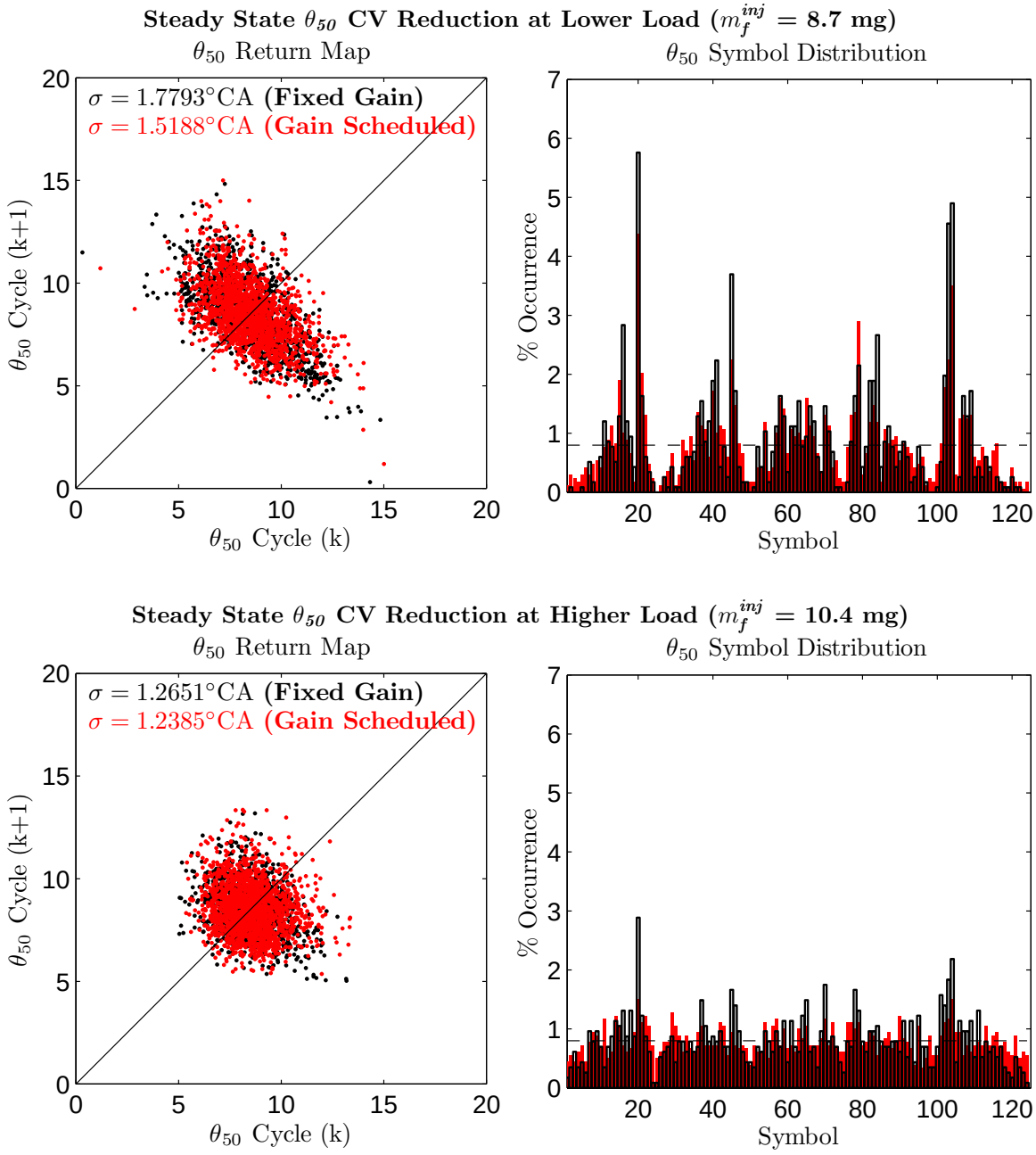

Figure 6.6: Comparison of gain scheduled feedback with fixed gain feedback. Steady state θ_{50} CV reduction at two engine loads.

terms of return maps and symbolic probability distribution plots. The return map shows the relationship between consecutive values of the combustion phasing θ_{50}. Please refer Sec. 5.4.2 for a discussion on the interpretation of return maps. Symbolic time-series analysis is a data-analysis technique that quantifies the probabilities of certain sequences of events occurring in noisy experimental data. The raw time-series data is transformed into a series of discretized symbols, and probabilities are assigned to finite-length sequences of these symbols. Temporal structure in observed data is revealed by the relative frequency of each possible symbol sequence. For example, in this case the time series data is divided into 5 equiprobable bins or symbols, and the symbol sequences are defined as triplets of these bins. The 5 bins can be thought of as datapoints with very early, early, normal, late, or very late phasings. Various types of statistics can be determined from the estimated symbol-sequence probability distribution. Symbolic analysis has been used in literature to characterize combustion data and compare combustion models [45, 90, 100].

In Fig. 6.6 reducing CV is understood in terms of reducing the standard deviation (σ) of the θ_{50} time series, contracting the θ_{50} return map, and flattening the symbolic probability distribution plot. Note that with these metrics, the gain scheduling feedback controller is able to significantly lower the CV at the lower load. This is also experimentally observed after about cycle 40 of the transient response of Fig. 6.5, after which the fixed gain feedback controller exhibits poor θ_{50}^{ref} regulation performance at low load conditions. The controller is of limited use in reducing the CV at the higher load operating point of Fig. 6.6. This behavior is expected as the onset of high CV is seen to occur later at higher loads, as discussed in Fig. 5.5. As confirmed by the flatter symbol sequence probability histogram of Fig. 6.6, the HCCI combustion dynamics in higher load case are mostly in the low CV dynamical region.

6.1.3 Stability of Controller

The stability of the improved controller with nonlinear feedforward and gain scheduled feedback can be analyzed using linear techniques. The analysis is similar to the stability analysis carried out for the baseline controller in Sec. 4.1.3. The nonlinear CV model presented in Chap. 5 is linearized at two operating points, one in the low CV region, and the other in the high CV region. The details of the linearization operating points are presented in Tab. 6.1. These operating points differ only in the value of u_{evc}.

As seen in the pole location map of Fig. 5.8, the temperature pole transitions

Quantity	Low CV Operating Point	High CV Operating Point
u_{evc}	241.1 °CA aTDC	252 °CA aTDC
m_f^{inj}	9.51 mg/cycle	9.51 mg/cycle
u_{soi}	330 °CA bTDC	330 °CA bTDC
ω	1800 rpm	1800 rpm
p_{im}	1.11 bar	1.11 bar
p_{em}	1.03 bar	1.03 bar
θ_{50}	5.48 °CA aTDC	10.89 °CA aTDC
Pole Locations	{0.320, 0.696}	{-0.446, 0.658}

Table 6.1: Linearization operating points for the CV model

from the right half plane to the left half plane as the system moves from the low CV operating point to the high CV operating point. This is seen in Tab. 6.1, where the model linearized at the low CV operating point has an open loop pole location at 0.320, while the location of the open loop pole moves to -0.446 for the model linearized at the high CV operating point. The presence of the negative eigenvalue results in oscillatory thermal dynamics at high CV conditions. It will be shown in this section that this fact results in the closed-loop baseline controller responses being oscillatory.

Controller Transfer Functions

Similar to the transfer function simplification carried out for the baseline controller in Sec. 4.1.3, the controller transfer functions are:

$$U_{soi}(z) = \frac{z\,(z-1)}{z\,(z-1) + K_{ff}^{evc} K_i^{evc}} \begin{bmatrix} K_p^{soi} + K_{ff}^{50} + \dfrac{K_i^{soi}}{z-1} \\ -K_p^{soi} - \dfrac{K_i^{soi}}{z-1} \\ \dfrac{K_{ff}^{m_f}}{z} \\ K_{ff}^{\omega} \\ \dfrac{K_{ff}^{evc} K_i^{evc}}{z\,(z-1)} \end{bmatrix}^T \begin{bmatrix} \Theta_{50}^{ref}(z) \\ \Theta_{50}^{fb}(z) \\ M_f^{inj}(z) \\ \Omega(z) \\ U_{soi}^{ref}(z) \end{bmatrix} \tag{6.7}$$

$$U_{evc}(z) = \frac{K_i^{evc} z}{z\,(z-1) + K_{ff}^{evc} K_i^{evc}} \begin{bmatrix} -K_p^{soi} - K_{ff}^{50} - \dfrac{K_i^{soi}}{z-1} \\ K_p^{soi} + \dfrac{K_i^{soi}}{z-1} \\ -\dfrac{K_{ff}^{\dot{m}_f}}{z} \\ -K_{ff}^{\omega} \\ 1 \end{bmatrix}^T \begin{bmatrix} \Theta_{50}^{ref}(z) \\ \Theta_{50}^{fb}(z) \\ M_f^{inj}(z) \\ \Omega(z) \\ U_{soi}^{ref}(z) \end{bmatrix}. \quad (6.8)$$

where

$$K_p^{soi} = \begin{cases} K_{p,lowcv}^{soi} & \text{if } \theta_{50}(k) \leq \theta_{50}^{thresh}(m_f^{inj}) \\ K_{p,highcv}^{soi} & \text{if } \theta_{50}(k) > \theta_{50}^{thresh}(m_f^{inj}). \end{cases} \quad (6.9)$$

Here $\Theta_{50}^{ref}(z), M_f^{inj}(z), \Omega(z), U_{soi}^{ref}(z)$ are the z-transforms of $\theta_{50}^{ref}(k), m_f^{inj}(k), \omega(k)$ & $u_{soi}^{ref}(k)$ respectively. Also, $\Theta_{50}^{fb}(z)$ is the z-transform of the feedback output $\theta_{50}(k-1)$. Mathematically, $\theta_{50}^{fb}(k) = \theta_{50}(k-1)$ or $\Theta_{50}^{fb}(z) = \frac{\Theta_{50}(z)}{z}$.

Closed-Loop Eigenvalues and Four Transfer Function Theorem

One can analyze the closed-loop eigenvalues of the systems formed by combining the controllers of Eq. (6.7) and Eq. (6.8), with the CV model linearized at the low CV and the high CV operating points specified in Tab. 6.1. Three different plant and controller combinations that correspond to the baseline and the improved controllers are considered. As per the analysis in Sec. 4.1.3, the closed-loop pole locations of the four transfer functions from the inputs (reference and input disturbance) to the outputs (θ_{50} and controller outputs) are considered, as follows:

1. Model linearized at low CV operating point, with $K_p^{soi} = K_{p,lowcv}^{soi}$ (Baseline and improved controllers): $\{0.9681, 0.8903, 0.6930, 0.3054, 0, -0.0127\}$.
2. Model linearized at high CV operating point, with $K_p^{soi} = K_{p,lowcv}^{soi}$ (Baseline controller): $\{0.9568, 0.9187, 0.6502, 0.0670, 0, -0.6946\}$.
3. Model linearized at high CV operating point, with $K_p^{soi} = K_{p,highcv}^{soi}$ (Improved controller): $\{0.9572, 0.8974, 0.6318, 0.0196 \pm 0.4907i, 0\}$.

From this list it is seen that using the baseline controller at high CV operating conditions introduces oscillatory dynamics through the closed-loop pole located on the negative real axis (-0.6946). Using $K_p^{soi} = K_{p,highcv}^{soi}$ instead, as suggested by the gain-scheduled feedback, pulls this closed-loop pole into the right half unit circle.

1. Low CV linearization point with $K_p^{soi} = K_{p,lowcv}^{soi}$ (Baseline & Improved Controller)

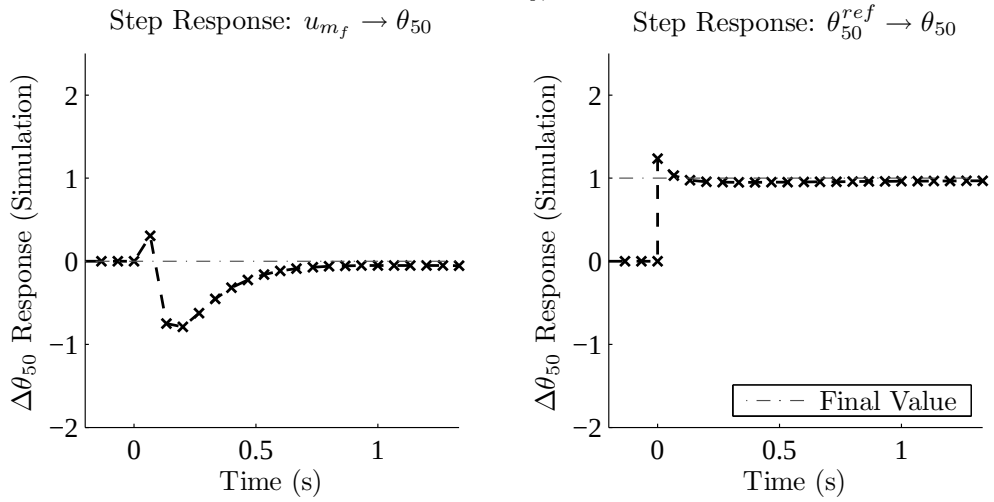

2. High CV linearization point with $K_p^{soi} = K_{p,lowcv}^{soi}$ (Baseline Controller)

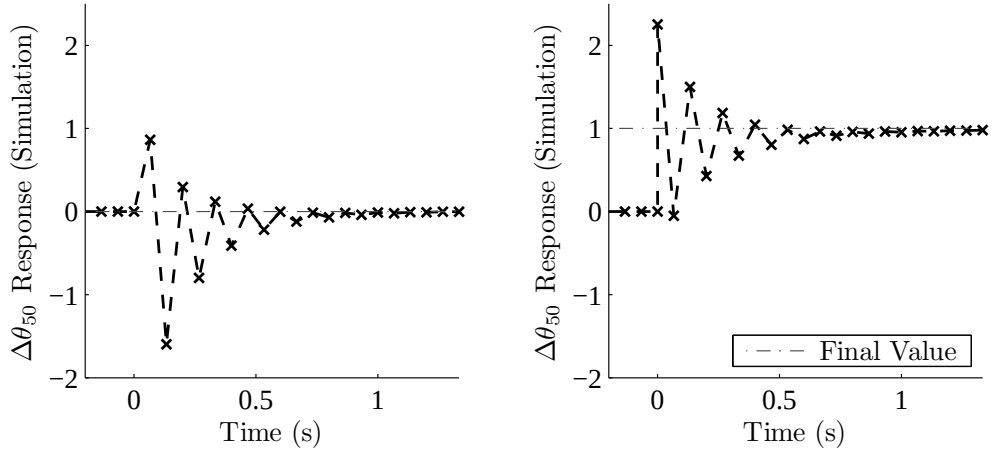

3. High CV linearization point with $K_p^{soi} = K_{p,highcv}^{soi}$ (Improved Controller)

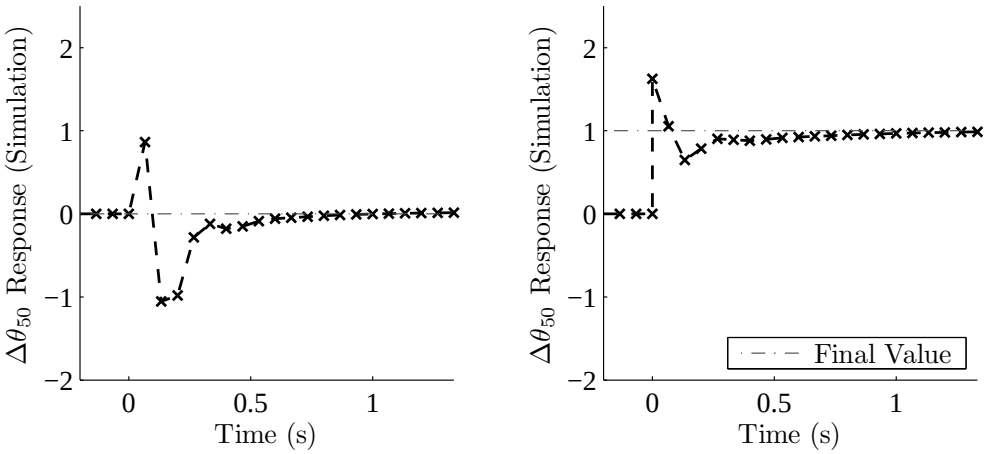

Figure 6.7: Simulated step responses for baseline and improved controllers. Using two different K_p^{soi} gains avoids oscillatory response seen in baseline controller.

This can be seen in an alternative manner in the closed-loop step responses shown in Fig. 6.7. In this figure, the θ_{50} responses of the closed-loop systems to unit steps in m_f^{inj} and θ_{50}^{ref} are compared. It is clearly seen that the responses of the improved controller are stable and non-oscillatory in both low CV and high CV dynamical regions.

Note that this analysis does not comment on the stability during the switching operation. Switching between individually stable systems does not guarantee stability of the switched system in general. Using the theory of switched linear systems to demonstrate stability of the gain scheduling scheme using linearized plant models is planned for future work. An example of such a stability analysis for a HCCI control strategy is seen in [92].

6.2 Experimental Validation of Controller

The experimental results in this section demonstrate that the controller can track desired combustion phasing during HCCI transitions similar those seen during a typical drive cycle. The transitions considered consist of a combination of simultaneously varying engine load (desired IMEP), engine speed, and desired combustion phasing (θ_{50}^{ref}).

First in Sec. 6.2.1 good θ_{50}^{ref} regulation performance during load transitions at a fixed engine speed is demonstrated. Results are presented for both tip-in and tip-out behavior. Experiments demonstrating good tracking performance during speed ramps at constant load are presented in Sec. 6.2.2. Section 6.2.3 presents control results for simultaneous load and speed transitions. Finally in Sec. 6.2.4 the controller is tested on some select transitions with high load slew rates from an FTP75 drive cycle analysis, which is used to represent typical driving behavior.

6.2.1 Load Transitions at Fixed Engine Speed

Figure 6.8 shows control results for two load transitions with engine speed fixed at 1500 rpm. The subfigures on the top and bottom present results for load steps down and up respectively. The load step down is the more challenging of the two to control, as the significantly reduced charge temperatures can lead to excessively late phasing, high CV, and potential engine misfire. In these transitions, the desired θ_{50}^{ref} and the gain scheduling threshold θ_{50}^{thresh} are kept constant.

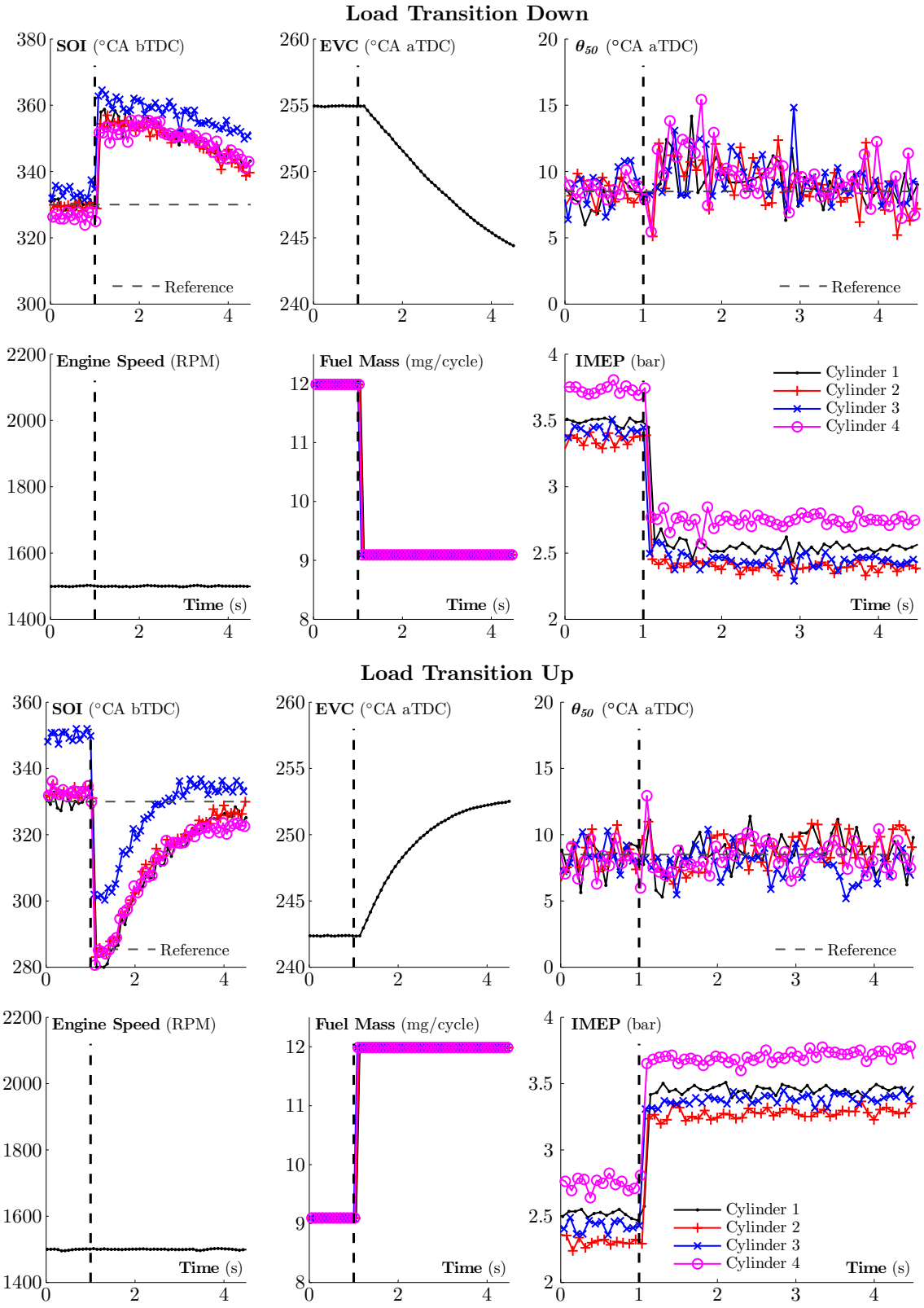

Figure 6.8: Load transition at fixed engine speed – θ_{50} regulation during load steps up and down. Note that the u_{soi} actuators are cylinder-individual, but there is only a single u_{evc} actuator for the entire engine.

The fuel mass for the transitions is stepped over a single cycle at time $t = 1\,\text{sec}$. The torques for all four cylinders step smoothly from the initial to the final values without any spikes or dips. Note that the cylinder torques differ due to cylinder-to-cylinder variations in a multi-cylinder engine. These torque differences can be controlled by varying m_f^{inj} on a cylinder-to-cylinder basis, but in this work m_f^{inj} for all cylinders was kept constant. Good θ_{50} regulation performance is observed for all four cylinders. The combustion phasing is regulated to the set-point of 8.5°CA aTDC, and stays within reasonable bounds during the load transition.

The control inputs u_{soi} and u_{evc} demonstrate typical mid-ranging behavior. The initial transient response to load step is controlled by the fine actuator (u_{soi}). The sudden initial jump in the u_{soi} response is driven by the u_{soi} feedforward block, and compensates for the sudden change in charge temperature before any adverse effect on the θ_{50} output can be seen. The coarse actuator (u_{evc}) slowly returns u_{soi} of a reference cylinder, here cylinder 1, back to its nominal setpoint, which is 330°CA bTDC in these tests. Note that due to cylinder-to-cylinder variations in a multicylinder engine, only one of the u_{soi} actuators can be returned to the nominal setpoint. Also, the u_{soi} actuator is saturated at 280°CA bTDC to avoid fuel injection while the intake valve is open.

These load transitions are large in the sense that they cover a major portion of the available HCCI load range at this engine speed and boost pressure, as limited by the ringing and high CV constraints. Also, load transitions of this magnitude would cause the baseline controller to fail and cause engine misfires. The proposed solution in Chap. 4 involved the addition of a model-predictive filter that intelligently slowed down the desired load command. The current controller is an improvement in the sense that it does not slow down the load command at all. It is able to compensate for the entire step in a single cycle, with a load slew rate of approximately 1 bar/cycle. This quick matching of the driver's desired torque demand improves driveability.

Figure 6.9 demonstrates how the measured pressure traces vary before and during a controlled load transition at a fixed engine speed of 1800 RPM. The data plotted in black occurs before the load transition, and the data plotted in red occurs after the load step down. The pressure traces shrink and the peak pressures drop significantly in a single cycle after the transition. The IMEP results confirm that the load drops smoothly from the initial to the final value with no significant oscillations. The θ_{50}^{ref} regulation performance is good, with the measured θ_{50} not deviating significantly from the desired $\theta_{50}^{ref} = 8.5\,^\circ$ CA aTDC.

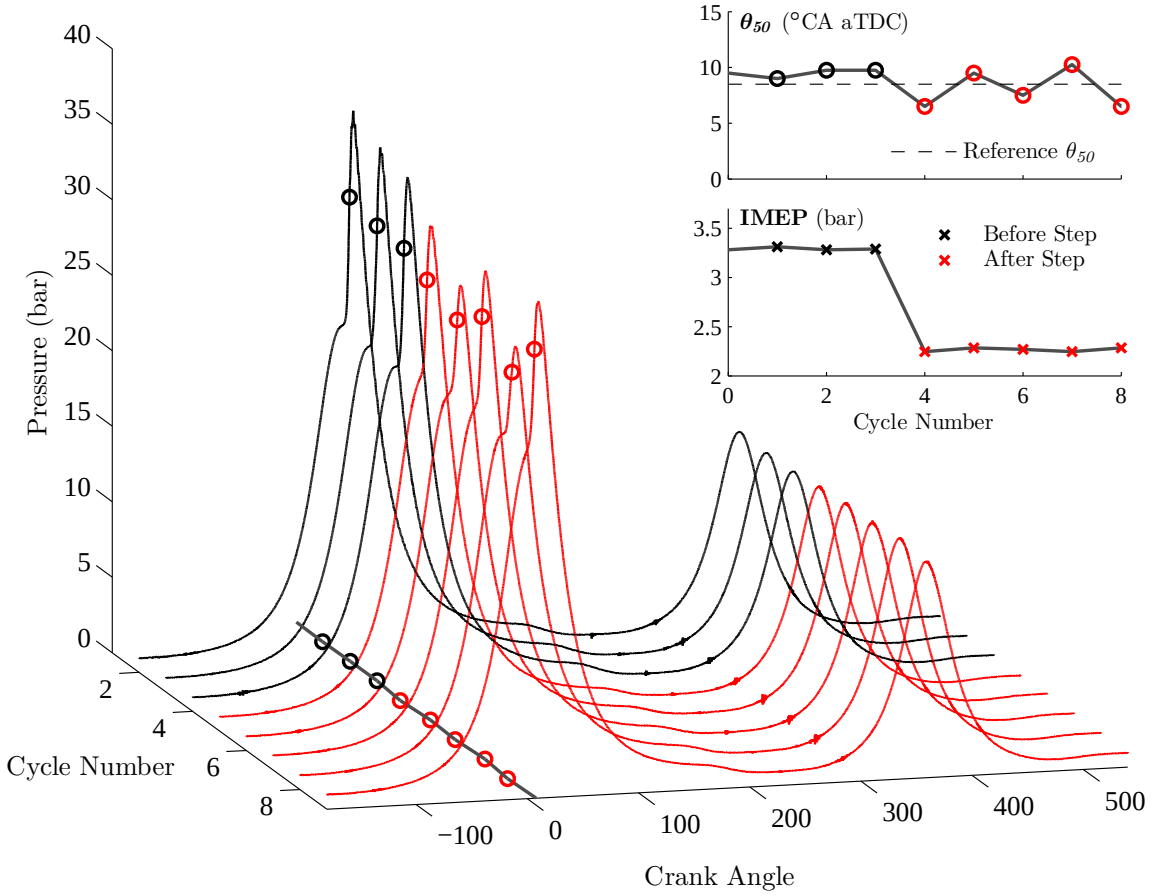

Figure 6.9: Pressure traces before and after a load step down at 1800 RPM. The cycle-by-cycle θ_{50} values are plotted on the pressure traces, and are projected onto the XY plane.

6.2.2 Engine Speed Transitions at Fixed Load

Next the control strategy is tested during engine speed ramps, see Fig. 6.10. The subfigures on the top and bottom present combustion phasing regulation results for an engine speed increase and decrease respectively. The engine speed is varied from 1500 rpm to 2100 rpm and back again, while maintaining a fixed m_f^{inj} and hence a nearly fixed engine load. The engine speed slew rate is determined by the experimental dynamometer dynamics.

It is seen that the controller successfully regulates θ_{50} to the desired $\theta_{50}^{ref} = 8.5°\text{CA}$. Combustion phasing response is smooth and non-oscillatory, while the IMEP does not vary much. The gain scheduling threshold (θ_{50}^{thresh}) is kept constant.

In Fig. 6.10, results are shown for all four cylinders. Henceforth, results for a single cylinder will be presented for clarity.

6.2.3 Simultaneous Load and Speed Transitions

In this section, θ_{50} regulation results are presented for simultaneous load & speed transitions. Figure 6.11 presents control results for all four combinations of the desired engine speed and engine load increasing and decreasing, i.e.:

1. Engine load ↑, engine speed ↑
2. Engine load ↓, engine speed ↓
3. Engine load ↓, engine speed ↑
4. Engine load ↑, engine speed ↓.

In these transitions, engine speed is varied from 1500 to 2100 RPM and vice-versa. The magnitude and rate of engine speed variation tested in Fig. 6.11 is as large as any HCCI transition seen in the FTP75 drive-cycle analysis, see Sec. 6.2.4. Due to experimental dynamometer restrictions, the engine speed slew rate was fixed and could not be varied. The desired load was commanded to vary at the same rate as the engine speed, as seen from the m_f^{inj} actuator plot. In these transitions, the desired θ_{50}^{ref} and the gain scheduling threshold θ_{50}^{thresh} are kept constant.

Figure 6.11 demonstrates satisfactory θ_{50}^{ref} regulation performance for all four transitions. Misfires are avoided, and the IMEP response is smooth. As can be seen, the magnitudes of u_{soi} and u_{evc} control efforts are significantly more when the desired load and speed move in the same direction (either both increase or both decrease). In fact when the desired engine speed and load move in opposite directions in the transitions presented, the required controller effort is nearly zero. The open loop responses of θ_{50} to the variations in speed and load cancel each other out. Note that the feedforward component of u_{soi} successfully realizes this and does not deviate from the reference

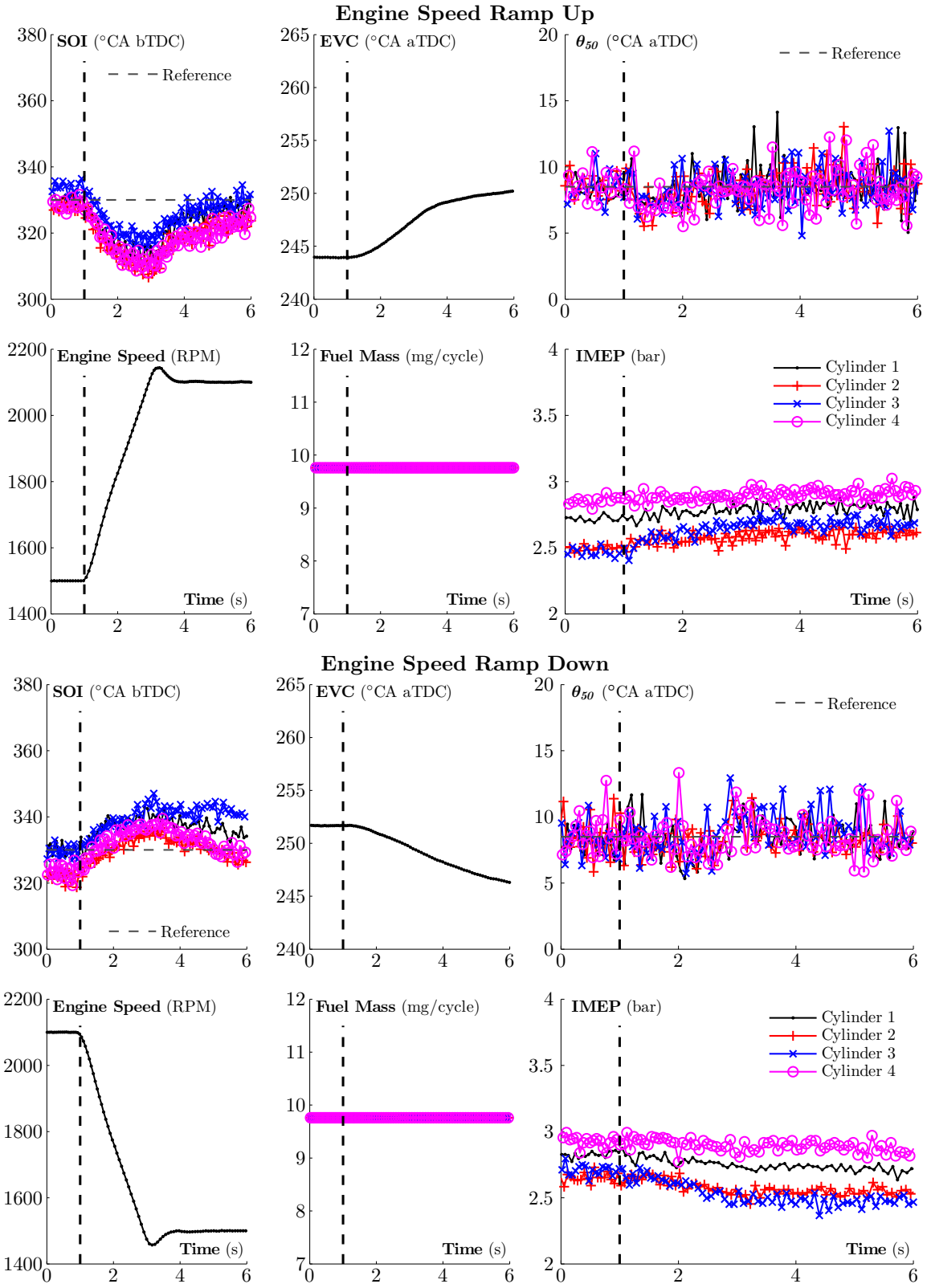

Figure 6.10: Engine speed transition at fixed load – θ_{50} regulation during load steps up and down. Note that the u_{soi} actuators are cylinder-individual, but there is only a single u_{evc} actuator for the entire engine.

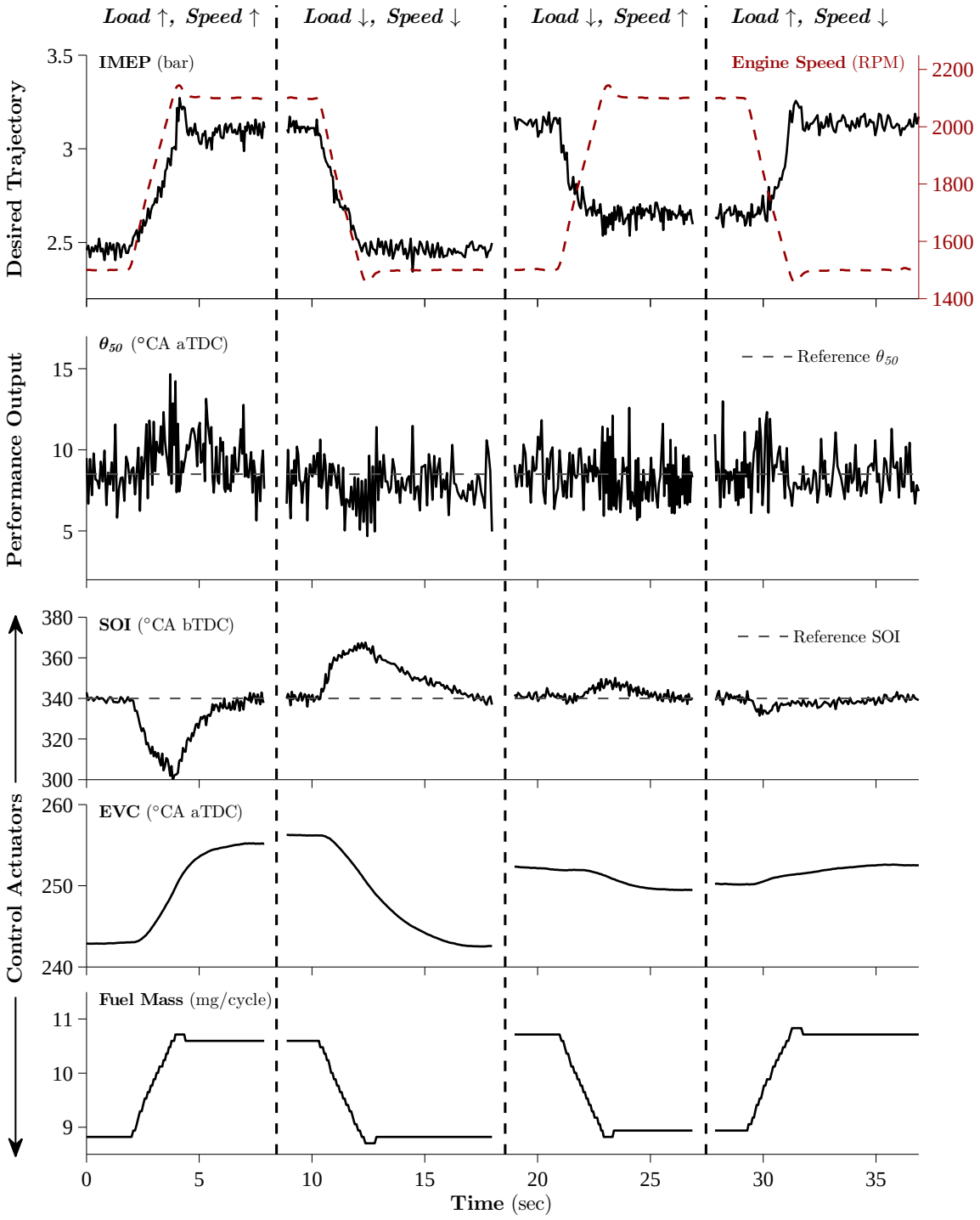

Figure 6.11: Simultaneous load and speed transitions – θ_{50} regulation results shown for four combinations of engine load and speed increasing and decreasing.

Table 6.2: Select HCCI transitions from FTP75 drive-cycle analysis

Name	Time (sec)		Speed (RPM)			IMEP (bar)	
	From	To	From	To	Chosen	From	To
Down	1301.9	1302.34	2110	2130	2100	3.46	2.39
Up	533.19	533.39	1790	1800	1800	2.63	3.69

u_{soi} setpoint.

6.2.4 HCCI Transitions seen in FTP75 drive cycle analysis

Finally, the controller is tested on select HCCI transitions from the FTP75 drive-cycle analysis performed in [8]. The FTP75 driving cycle was experimentally performed on a chassis dynamometer by a human driver in a Cadillac CTS car equipped with a 3.6L V6 engine. This is the baseline engine and vehicle configuration that is to be downsized to the 2.0L I4 multi-mode combustion engine used in this work. In [8] the engine torque and speed measurements are appropriately scaled to the new engine configuration, and an analysis of transitions within the HCCI region is performed. This analysis of the engine speeds and torques demanded in the HCCI region is used in this section to determine the HCCI transitions to test the controller on.

Selection of the HCCI Transitions to be Tested

The transitions tested on the multicylinder engine are listed in Tab. 6.2. HCCI transitions with high load slew rates were selected from FTP75 drive-cycle analysis. The transition named "Down" involves a load (IMEP) decrease from 3.46 bar to 2.39 bar in 7.5 engine cycles. The engine speed does not vary much, and is chosen to be fixed at 2100 rpm. The transition named "Up" involves a load (IMEP) increase from 2.63 bar to 3.69 bar in 3 engine cycles. Again, the engine speed does not vary much, and is chosen to be fixed at 1800 rpm.

The engine speed range of the HCCI operating region for the multicylinder engine is between 1500 RPM and 3000 RPM. However, the HCCI combustion model used in this work is tested for a smaller speed range between 1500 and 2200 RPM, and so the HCCI transitions selected from the FTP75 drive cycle analysis were restricted to this speed range. The engine load range of the transitions tested is limited by the high and low load range of the HCCI operating map.

Discussion of Experimental Results

Figure 6.12 presents θ_{50}^{ref} tracking results for the select HCCI transitions from the FTP75 drive-cycle analysis, as listed in Tab. 6.2. For both transitions, the IMEP performance output steps smoothly from the initial to the final desired level. Exact tracking of desired IMEP at steady-state is not achieved, since in this work there is no closed-loop control of IMEP, and m_f^{inj} is scheduled from an pre-determined look-up table.

In these transitions, the desired θ_{50}^{ref} varies as a function of load, and is set later for higher loads. This strategy is more realistic than regulating a constant θ_{50}^{ref} because it helps reduce high pressure rise rates at higher loads. However, this makes the control problem more challenging, as the transient control requires greater controller effort. As seen in Fig. 6.12, satisfactory transient θ_{50}^{ref} tracking is achieved for the transition named "Down", but there is a large θ_{50}^{ref} tracking error for about 1 second after the transition named "Up". However, two seconds after the transition is commanded, satisfactory tracking is achieved. Further this has no discernible effect on IMEP variability, and hence on driveability.

The initial poor θ_{50}^{ref} tracking performance in the transition "Up" is due to actuator saturation. The initial transient response to the load variation is almost exclusively provided by the fast actuator u_{soi}, which quickly saturates at 280°CA bTDC. As mentioned earlier, it is saturated at this level to avoid fuel injection while the intake valve is open. While u_{soi} is saturated, the only actuator available for θ_{50}^{ref} tracking control is the slow u_{evc} actuator that attempts to return u_{soi} away from saturation, and to its nominal value. Poor θ_{50}^{ref} tracking performance persists while the u_{soi} saturation exists.

Another interesting effect of actuator saturation is seen in the transition named "Down". Here it is u_{evc} that saturates at 241°CA aTDC at around $t = 4\,\text{sec}$. This saturation is a hardware limit of the cam phaser. As a result of the architecture of the controller in Fig. 6.2, this saturation does not affect the θ_{50}^{ref} tracking performance, but rather prevents u_{soi} from returning to its nominal value. This does not affect the transition under consideration, but does limit subsequent transitions. For example, in this case where u_{evc} is saturated at the early limit, further reductions in load are restricted.

Anti-windup schemes are implemented in the controller to help deal with both u_{soi} and u_{evc} actuator saturation. Also note that the K_p^{soi} gain scheduling threshold (θ_{50}^{thresh}) varies with load, as discussed in Sec. 5.3.

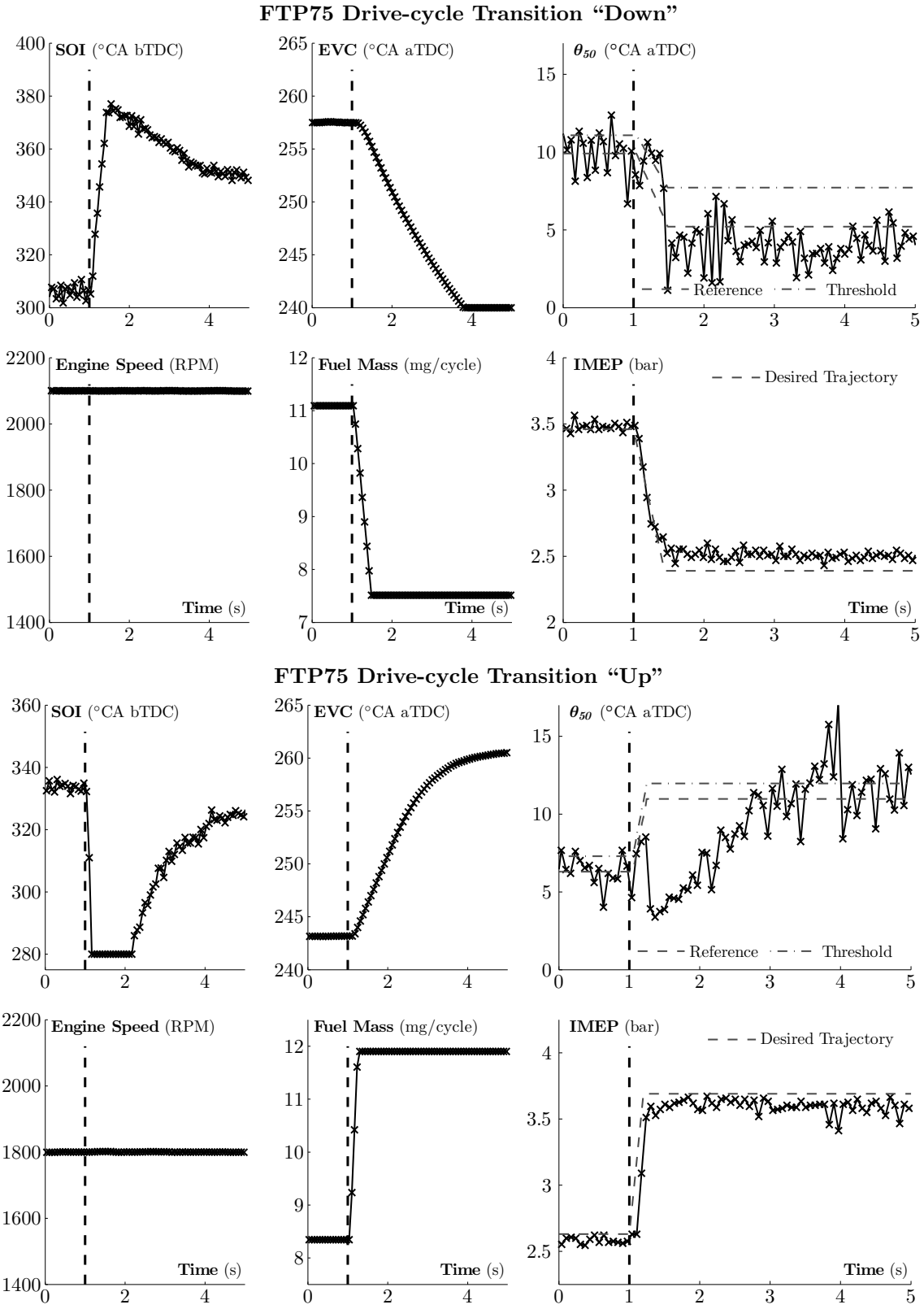

Figure 6.12: Load transition at fixed engine speed – θ_{50} regulation during load steps up and down. Note that the u_{soi} actuators are cylinder-individual, but there is only a single u_{evc} actuator for the entire engine.

6.3 Summary

A model-based control strategy is presented to track combustion phasing during HCCI transitions, which include a combination of load, speed and θ_{50}^{ref} variations. The controller uses cylinder-individual u_{soi} and m_f^{inj}, and cylinder-common u_{evc} as control actuators. Novel aspects of the controller include nonlinear model inversion-based feedforward, and gain scheduled feedback that distinguishes between HCCI combustion regimes demonstrating different dynamic behavior. The occurrence of high CV and low CV dynamic regions is understood through unburned fuel dynamics, and this physical understanding is used to to improve feedback performance.

The controller is tested on a number of HCCI transitions – including load transitions at fixed engine speeds, speed ramps at fixed engine loads, combined load and speed transitions, and select transitions from an FTP75 drive-cycle analysis. The controller successfully tracks θ_{50}^{ref} while transitioning smoothly from one load-speed operating point to the next. As compared to previous control solutions, the current controller does not slow down the desired load command, thus improving driveability. This stable and fast transient control enables the engine to maximize the length of stay in the HCCI region, and hence the efficiency benefit.

Actuator saturation can lead to sub-par θ_{50}^{ref} tracking or u_{soi} mid-ranging performance, but does not affect the IMEP tracking performance. However, this must be kept in mind while implementing the controller on a real engine.

Chapter 7
Conclusions and Future Work

7.1 Conclusions and Results

Homogeneous Charge Compression Ignition (HCCI) combustion is a promising low-temperature combustion mode for gasoline engines, with high thermal efficiency and low engine-out emissions. Performing load-speed transitions in the HCCI operating region requires careful regulation of in-cylinder charge conditions to avoid ringing and misfire constraints. The actuation strategy used in this work, recompression HCCI, introduces significant internal feedback through trapped residual gases that makes HCCI combustion phasing control an interesting controls challenge.

This work presents two modeling and controls strategies to solve the HCCI combustion phasing problem. In the first approach, a low-order control-oriented model is developed that describes HCCI combustion in the low cyclic variability HCCI operating region. It is desired to maintain combustion in this region for efficiency and stability reasons. A baseline controller that coordinates four u_{soi} actuators and one u_{evc} actuator to regulate combustion phasing is adapted from literature, and tuned using the model. It is experimentally shown that the baseline controller works satisfactorily for small to mid load transitions, but not for larger load transitions where engine misfires were recorded. The fuel governor strategy is introduced to improve load and combustion phasing tracking performance. In this strategy, the baseline controller is augmented with a reference governor that modifies the desired load trajectory if future actuator violations are predicted. The fuel governor is a predictive control strategy that uses the plant model to predict future closed-loop trajectories. It is experimentally shown that this control strategy improves load transition performance, and extends the controllable load transition range. One disadvantage of the fuel governor strategy is that the observed load transition is slower than desired when future actuator constraint violations are predicted.

Experimental results suggest that HCCI combustion enters a region of high cyclic variability (CV) at low load or at late phasing conditions. Further, the combustion can enter this high CV region during transients, even if the starting and ending points of the transient are in a low CV dynamical region. These observations motivate the second modeling and control strategy presented in this dissertation. The oscillatory dynamics at low load and late phasing conditions are understood in terms of low combustion efficiency, increased unburned fuel, and NVO heat release. These insights are used to augment the previously described HCCI model with an unburned fuel state and recompression heat release. It is shown that this CV model is capable of predicting the onset of high CV, and the nature of the variability in both low and high CV dynamical conditions. The model predicts the appearance of a negative real eigenvalue at late phasing conditions.

The understanding gained through the analysis and modeling of the nature and occurrence of the high CV dynamical region is used to develop an improved HCCI combustion phasing controller. The baseline controller is augmented with a nonlinear model inversion-based feedforward, and a gain-scheduling feedback. The nonlinear model inversion-based feedforward eliminates linearization errors, and is shown to be more accurate in simulation. The change in open loop plant dynamics at high CV conditions from damped to oscillatory suggests that different feedback gains are required in these conditions, thus motivating the gain scheduling feedback. Linear analysis demonstrates that the baseline controller feedback gains lead to oscillatory closed loop step responses, which are substantially improved when using high CV gains. The proposed controller is tested extensively in experiments run on a multi-cylinder engine. Successful output tracking is demonstrated for load steps, speed ramps, and simultaneous load and speed transients. Sample transitions with high load slew rates from an FTP75 drive cycle simulation are experimentally tested with the controller.

7.2 Future Work and Open Challenges

This work emphasizes the need for transient HCCI controllers to consider lowered main combustion efficiency, and heat release due to the presence of unburned and recycled fuel in the recompression region. Future work should include improving the simple modifications made in the CV model to predict the onset and nature of high variability. More sophisticated modeling of the heat release during NVO should extend the range of validity of the model.

Recompression HCCI engines can demonstrate high cylinder-to-cylinder variability. Developing control-oriented models for each cylinder can be a time and resource intensive task. Also, model fidelity reduces over time due to engine ageing, which in turn reduces the accuracy of the model inversion-based feedforward. Adaptive techniques that improve the model and controller accuracy are proposed as a solutions to these problems. Preliminary adaptive techniques are currently being experimentally tested at the University of Michigan Powertrain Control Laboratory.

Finally, implementation of the control strategies proposed in this work on production ECU hardware is left for future work. The author believes that the controllers proposed is this dissertation are feasible for implementation from computational runtime and calibration effort perspectives.

Appendices

Appendix A

Burned Gas Fraction

As seen in Fig. A.1, the charge in the cylinder at any point of time is modeled as a mixture of three components – air, fuel and burned gases. The chemical composition of these mixtures is determined from the stoichiometric combustion equation. For example, from Eq. (A.1), which represents the stoichiometric combustion of iso-octane, the constituents of the in-cylinder charge are considered to be:

1. Fuel (iso-octane): C_8H_{18}
2. Air: $O_2 + 3.773N_2$
3. Burned gases: $8CO_2 + 9H_2O + 47.16N_2$

Note that the burned gas fraction is distinct from the residual gas fraction. During lean combustion the residual gases contain air. By definition the burned gases cannot contain any oxygen. In fact $b_c = b_{bd}x_r \implies b_c < x_r$.

Chemical Equation of Combustion The stoichiometric ($\lambda_c = 1$) and lean ($\lambda_c > 1$) combustion equations for iso-octane C_8H_{18} are given by:

$$C_8H_{18} + 12.5\,(O_2 + 3.773N_2) \rightarrow 8CO_2 + 9H_2O + 47.16N_2. \tag{A.1}$$

$$\begin{aligned} C_8H_{18} + 12.5\lambda_c\,(O_2 + 3.773N_2) + \frac{x_r}{1-x_r}(8CO_2 + 9H_2O + 47.16N_2) \\ \rightarrow \frac{1}{1-x_r}\,(8CO_2 + 9H_2O + 47.16N_2) + 12.5\,(\lambda_c - 1)\,(O_2 + 3.773N_2)\,. \end{aligned} \tag{A.2}$$

A.1 Molar fraction of oxygen

The molar fraction of oxygen (χ_{O2}) is an alternative measure of composition used in literature. It is defined as the ratio of the number of moles of oxygen to the total number of moles of reactants before combustion. In this section, the relationship between χ_{O2} and b_{bd} will be developed.

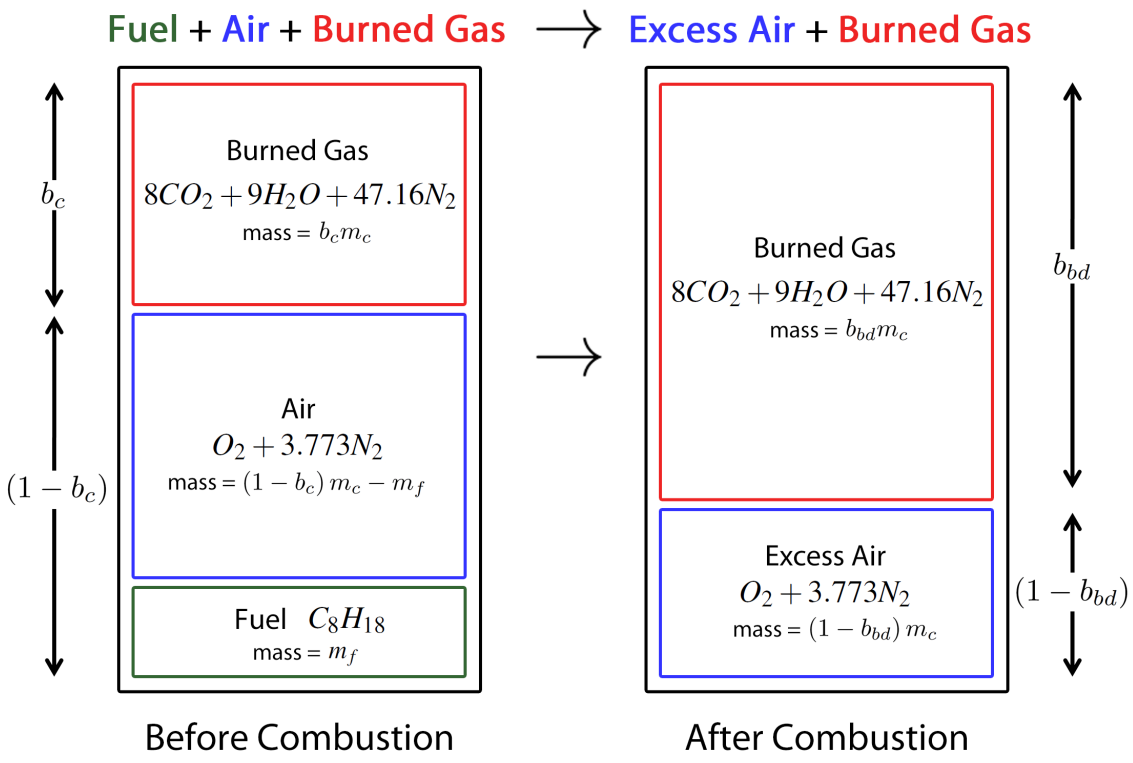

Figure A.1: Cylinder composition before and after combustion.

From Eq. (A.2) it is clear that if $\lambda_c > 1$, there is excess air in the exhaust. A portion of this excess air in the exhaust is recycled through the residual gases. As the composition of the residual gases and the gases after combustion is assumed to be the same, the ratio of the moles is also the ratio of the masses. The ratio of the masses is known to be x_r, by definition. This leads to the expression for χ_{O2} in terms of the in-cylinder air-fuel equivalence ratio λ_c and the residual gas fraction x_r:

$$\chi_{O2}(k) = \frac{N_{O2}}{N_{total}} = \frac{12.5\lambda_c(k)}{1 + 59.66\lambda_c(k) + \frac{64.16x_r(k)}{1-x_r(k)}}. \tag{A.3}$$

Finally, the air-fuel equivalence ratio λ_c can be expressed in terms of the burned gas fraction through Eq.(3.33), which is reproduced below:

$$\lambda_c(k) = \frac{1}{AFR_s} \cdot \left[(1 - b_c(k)) \frac{m_c}{m_f} - 1 \right] \tag{A.4}$$

$$m_c(k) = \frac{p_{ivc}V_{ivc}}{RT_{ivc}(k)}. \tag{A.5}$$

Equations (A.3) to (A.5) express the molar fraction of oxygen (χ_{O2}) in terms of the burned gas fraction state.

Appendix B
Model Coefficients

B.1 HCCI Model Coefficients

The two-state HCCI model for low CV conditions is presented in Chap. 3. The numerical values of the parameters and constants used in this model are listed in Tab. B.1 and Tab. B.2 respectively.

Table B.1: HCCI Combustion Model Coefficients

Symbol	Value	Description	References
α_0	-0.21277	x_r regression: constant u_{evc} term	Eq. (3.2), (3.36)
α_1	0.002180	x_r regression: linear u_{evc} term	Eq. (3.2), (3.36)
α_2	-0.61611	x_r regression: pressure ratio exponent	Eq. (3.2), (3.36)
α_3	0.80054	x_r regression: T_{bd} exponent	Eq. (3.2), (3.36)
α_4	-0.25650	x_r regression: ω exponent	Eq. (3.2), (3.36)
c_e	0.6886	Scaling constant for temperature drop during exhaust	Eq. (3.8), (3.39)
β_0	0	Charge cooling effect due to injection during recompression	Eq. (3.9)
β_1	0.89	Combustion efficiency sigmoid: scaling term	Eq. (3.16), (3.38)
β_2	34.9	Combustion efficiency sigmoid: offset term	Eq. (3.16), (3.38)
β_3	4.9	Combustion efficiency sigmoid: shape term	Eq. (3.16), (3.38)
β_4	1.997	Combustion efficiency sigmoid: speed term (constant)	Eq. (3.16), (3.38)

Continued on next page

Table B.1 – continued from previous page

Symbol	Value	Description	References
β_5	3.457×10^{-4}	Combustion efficiency sigmoid: speed term (linear)	Eq. (3.16), (3.38)
β_6	2.6563	Specific heat correction term	Eq. (3.17), (3.37)
A	1286	Arrhenius pre-exponential factor	Eq. (3.26), (3.40)
B	-11280	Arrhenius pre-exponential factor	Eq. (3.26), (3.40)
n_p	4.51	Arrhenius pressure exponent	Eq. (3.26), (3.40)
k_0	408	Arrhenius threshold offset term	Eq. (3.27), (3.40)
b_0	2.908	Combustion duration offset term	Eq. (3.29), (3.41)
b_1	1.306	Combustion duration linear term	Eq. (3.29), (3.41)

Table B.2: HCCI Combustion Model Constants

Symbol	Value	Description	References
n	1.3	Polytropic exponent	Eq. (3.9), (3.10), (3.13), (3.18), (3.20), (3.28), (3.35), (3.39)
q_{lhv}	44×10^3	Lower heating value of fuel	Eq. (3.14), (3.18), (3.20), (3.35)
R	288.3	Gas constant	Eq. (3.14), (3.18), (3.20), (3.21), (3.32), (3.35)
AFR_s	14.7	Stoichiometric air-fuel mass ratio	Eq. (3.21), (3.33), (3.34), (3.35)

B.2 CV Model Coefficients

The three-state HCCI model for both low CV and high CV conditions is presented in Chap. 5. The numerical values of the parameters and constants used in this model are listed in Tab. B.3 and Tab. B.4 respectively.

Table B.3: Extended HCCI Model Coefficients

Symbol	Value	Description	References
α_0	-0.2596	x_r regression: constant u_{evc} term	Eq. (3.2), (3.36), (5.9)
α_1	0.002562	x_r regression: linear u_{evc} term	Eq. (3.2), (3.36), (5.9)
α_2	-0.7005	x_r regression: pressure ratio exponent	Eq. (3.2), (3.36), (5.9)
α_3	0.7938	x_r regression: T_{bd} exponent	Eq. (3.2), (3.36), (5.9)
α_4	-0.2741	x_r regression: ω exponent	Eq. (3.2), (3.36), (5.9)
c_e	0.7845	Scaling constant for temperature drop during exhaust	Eq. (3.8), (3.39), (5.8)
β_0	0	Charge cooling effect due to injection during recompression	Eq. (3.9)
β_{1a}	0.8404	Combustion efficiency sigmoid: scaling term (constant)	Eq. (5.2)
β_{1b}	-0.1246	Combustion efficiency sigmoid: scaling term (linear)	Eq. (5.2)
β_1	1	Combustion efficiency sigmoid: scaling term	Eq. (5.6)
β_{2a}	15.039	Combustion efficiency sigmoid: offset term (constant)	Eq. (5.2)
β_{2b}	1.154	Combustion efficiency sigmoid: offset term (linear)	Eq. (5.2)
β_3	2.9	Combustion efficiency sigmoid: shape term	Eq. (3.16), (3.38), (5.2), (5.6)
β_4	1.502	Combustion efficiency sigmoid: speed term (constant)	Eq. (3.16), (3.38)
β_5	3.563×10^{-4}	Combustion efficiency sigmoid: speed term (linear)	Eq. (3.16), (3.38)
β_6	3.5214	Specific heat correction term	Eq. (3.17), (3.37)
μ	1.8×10^{-4}	NVO heat release term	Eq. (5.8)

Continued on next page

Table B.3 – continued from previous page

Symbol	Value	Description	References
A	524.3	Arrhenius pre-exponential factor	Eq. (3.26), (3.40)
B	-11005	Arrhenius pre-exponential factor	Eq. (3.26), (3.40)
n_p	4.71	Arrhenius pressure exponent	Eq. (3.26), (3.40)
k_0	404	Arrhenius threshold offset term	Eq. (3.27), (3.40)
b_0	2.908	Combustion duration offset term	Eq. (3.29), (3.41)
b_1	1.306	Combustion duration linear term	Eq. (3.29), (3.41)

Table B.4: Extended HCCI Model Constants

Symbol	Value	Description	References
n	1.3	Polytropic exponent	Eq. (3.9), (3.10), (3.13), (3.18), (3.20), (3.28), (3.35), (3.39)
q_{lhv}	44×10^3	Lower heating value of fuel	Eq. (3.14), (3.18), (3.20), (3.35)
R	288.3	Gas constant	Eq. (3.14), (3.18), (3.20), (3.21), (3.32), (3.35)
AFR_s	14.7	Stoichiometric air-fuel mass ratio	Eq. (3.21), (3.33), (3.34), (3.35)

Appendix C
Publications

C.1 Journal Articles

1. S. Jade, J. Larimore, E. Hellström, L. Jiang, and A. Stefanopoulou, "Controlled Load and Speed Transitions in a Multi-Cylinder Recompression HCCI Engine," *IEEE Transactions on Control Systems Technology*, 2013, submitted for review. [101].
2. J. Larimore, S. Jade, E. Hellström, L. Jiang, and A. Stefanopoulou, "Adaptive Control of a Recompression 4-Cylinder HCCI Engine," *IEEE Transactions on Control Systems Technology*, 2013, submitted for review [102].
3. S. Jade, E. Hellström, J. Larimore, L. Jiang, and A. Stefanopoulou, "Reference Governor for Load Control in a Multi-Cylinder Recompression HCCI Engine," *IEEE Transactions on Control Systems Technology*, 2013, to appear [99].
4. E. Hellström, J. Larimore, S. Jade, A. Stefanopoulou, and L. Jiang, "Reducing cyclic variability while regulating combustion phasing in a four-cylinder HCCI engine," *IEEE Transactions on Control Systems Technology*, 2013, to appear [93].

C.2 Conference Articles

5. J. Larimore, S. Jade, E. Hellström, A. G. Stefanopoulou, J. Vanier, and L. Jiang, "Online adaptive residual mass estimation in a multicylinder recompression HCCI engine," *in Proc. ASME Dynamic Systems and Control Conference*, 2013 [103].
6. S. Jade, E. Hellström, J. Larimore, L. Jiang, and A. Stefanopoulou, "Enabling Large Load Transitions on Multicylinder Recompression HCCI Engines using Fuel Governors," *in Proc. American Control Conference*, 2013 [104].
7. J. Larimore, E. Hellström, S. Jade, L. Jiang, and A. Stefanopoulou, "Controlling Combustion Phasing Variability with Fuel Injection Timing in a Multi-Cylinder HCCI Engine," *in Proc. American Control Conference*, 2013 [5].
8. S. Jade, E. Hellström, L. Jiang, and A. Stefanopoulou, "Fuel governor augmented control of recompression HCCI combustion during large load transients," *in Proc. American Control Conference*, 2012 [71].

9. S. Jade, E. Hellström, A. Stefanopoulou, and L. Jiang, "On the influence of composition on the thermally-dominant recompression HCCI combustion dynamics," *in Proc. ASME Dynamic Systems and Control Conference*, 2011 [105].

C.3 Patent Applications

10. J. Larimore, S. Jade, L. Jiang, E. Hellstrom, A. Stefanopoulou, and J. Vanier, "Device and method for real-time residual gas estimation," 2013, Application filed, Patent App. No.: 61/766754 [106].
11. S. Jade, E. Hellstrom, A. Stefanopoulou, and L. Jiang, "Fueling strategy for controlled autoignition engines," Apr. 11 2013, US Patent 20,130,090,838 (Application) [107].
12. S. Jade, E. Hellstrom, A. Stefanopoulou, and L. Jiang, "Fuel governor for controlled autoignition engines," Apr. 11 2013, US Patent 20,130,090,837 (Application) [108].

Bibliography

[1] T. J. Wallington, J. L. Sullivan, and M. D. Hurley, "Emissions of CO_2, CO, NO_x, HC, PM, HFC-134a, N_2O and CH_4 from the global light duty vehicle fleet," *Meteorologische Zeitschrift*, vol. 17, no. 2, pp. 109–116, 2008-04-01T00:00:00. [Online]. Available: http://www.ingentaconnect.com/content/schweiz/mz/2008/00000017/00000002/art00002 viii, 2

[2] Centre for Climate and Energy Solutions, "Comparison of Actual and Projected Fuel Economy for New Passenger Vehicles," http://www.c2es.org/federal/executive/vehicle-standards/fuel-economy-comparison, 2012, [Online; accessed 28-Oct-2013.] Source: An, F., and A. Sauer. 2004. Comparison of Passenger Vehicle Fuel Economy and GHG Emission Standards Around the World. Pew Center on Global Climate Change, Washington, DC; Updated data obtained from "Global passenger vehicle standards," The International Council for Clean Transportation, Retrieved from http://www.theicct.org/info-tools/global-passenger-vehicle-standards, June 2012. See more at: http://insights.wri.org/news/2012/08/what-look-epas-forthcoming-standards-emissions-light-duty-vehicles#sthash.ADaBKksG.dpuf. ix, 2

[3] E. Hellström and A. G. Stefanopoulou, "Modeling cyclic dispersion in autoignition combustion," in *IEEE Conf. Dec. Control*, 2011. ix, 27, 71, 73

[4] E. Hellström, A. G. Stefanopoulou, and L. Jiang, "Cyclic variability and dynamical instabilities in autoignition engines with high residuals," *IEEE Transactions on Control Systems Technology*, vol. 21, no. 5, pp. 1527–1536, 2013. xi, 70, 73, 80

[5] J. Larimore, E. Hellström, S. Jade, L. Jiang, and A. G. Stefanopoulou, "Controlling combustion phasing variability with fuel injection timing in a multicylinder HCCI engine," in *Proc. American Control Conference*, 2013. xi, 40, 70, 73, 92, 122

[6] E. Hellström, A. Stefanopoulou, J. Vavra, A. Babajimopoulos, D. Assanis, L. Jiang, and H. Yilmaz, "Understanding the Dynamic Evolution of Cyclic Variability at the Operating Limits of HCCI Engines with Negative Valve Overlap," *SAE Int. J. Engines*, vol. 5, no. 3, pp. 995–1008, 2012. xi, 13, 35, 41, 69, 73, 77, 80, 81

[7] L. Manofsky, J. Vavra, D. Assanis, and A. Babajimopoulos, "Bridging the Gap between HCCI and SI : Spark- Assisted Compression Ignition," *SAE Paper*, no. 2011-01-1179, 2011. xi, 41, 77

[8] S. Nüesch, E. Hellström, L. Jiang, and A. G. Stefanopoulou, "Influence of Transitions between SI and HCCI Combustion on Driving Cycle Fuel Consumption," in *Proc. European Control Conference*, Zürich, Switzerland, 2013. xi, 86, 87, 107

[9] C. on Transitions to Alternative Vehicles, F. B. on Energy, E. S. D. on Engineering, and P. S. N. R. Council, *Transitions to Alternative*

Vehicles and Fuels. The National Academies Press, 2013. [Online]. Available: http://www.nap.edu/openbook.php?record_id=18264 1

[10] Committee on the Assessment of Technologies for Improving Light-Duty Vehicle Fuel Economy; National Research Council, *Assessment of Fuel Economy Technologies for Light-Duty Vehicles*. The National Academies Press, 2011. [Online]. Available: http://www.nap.edu/openbook.php?record_id=12924 1

[11] M. Yao, Z. Zheng, and H. Liu, "Progress and recent trends in homogeneous charge compression ignition (HCCI) engines," *Progress in Energy and Combustion Science*, vol. 35, no. 5, pp. 398–437, Oct. 2009. 3, 11

[12] F. Zhao, T. N. Asmus, D. N. Assanis, J. E. Dec, J. A. Eng, and P. M. Najt, *Homogeneous Charge Compression Ignition (HCCI) Engines – Key Research and Development Issues*. SAE International, 2003, pT-94. 3, 4

[13] H. Zhao, Ed., *HCCI and CAI Engines for the Automotive Industry*. Woodhead Publishing Limited and CRC Press LLC, 2007. 3

[14] S. Onishi, S. Hong Jo, K. Shoda, P. Do Jo, and S. Kato, "Active thermo atmospheric combustion (atac) - a new combustion process for internal combustion engines," *SAE Paper*, no. 790501, 1979. 3

[15] M. Noguchi, Y. Tanaka, T. Tanaka, and Y. Takeuchi, "A study on gasoline engine combustion by observation of intermediate reactive products during combustion," *SAE Paper*, no. 790840, 1979. 3

[16] P. Najt and D. Foster, "Compression-ignited homogeneous charge combustion," *SAE paper*, no. 830264, 1983. 3, 11

[17] R. Thring, "Homogeneous-charge compression-ignition (HCCI) engines," *SAE Paper*, no. 892068, 1989. 3

[18] "Honda readies activated radical combustion two-stroke engine for production motorcycle," *Automotive Engineer*, pp. 90–92, Jan 1997. 3

[19] J. Willand, R.-G. Nieberding, G. Vent, and C. Enderle, "The knocking syndrome - its cure and its potential," *SAE Paper*, no. 982483, 1998. 3, 4, 12, 15

[20] J. Heywood, *Internal Combustion Engine Fundamentals*. McGraw-Hill Science/Engineering/Math, 1988. 3, 17

[21] A. Kulzer, J. Hathout, C. Sauer, R. Karrelmeyer, W. Fischer, and A. Christ, "Multi-Mode Combustion Strategies with CAI for a GDI Engine," *SAE Paper*, no. 2007-01-0214, 2007. 3

[22] J. Eng, "Characterization of pressure waves in hcci combustion," *SAE Paper*, no. 2002-01-2859, 2002. 4

[23] J. Dec, "A computational study of the effects of low fuel loading," *SAE Paper*, no. 2002-01-1309, 2002. 4

[24] C.-J. Chiang and A. G. Stefanopoulou, "Sensitivity analysis of combustion timing of Homogeneous Charge Compression Ignition gasoline engines," *J. Dyn. Syst. Meas. Control*, vol. 131, no. 1, pp. 014 506–1 to 014 506–5, 2009. 5, 25, 31, 41

[25] J.-O. Olsson, P. Tunestål, and B. Johansson, "Closed-Loop Control of an HCCI Engine," *SAE paper*, no. 2001-01-1031, 2001. 5, 16

[26] F. Agrell, H.-e. Ångström, B. Eriksson, J. Wikander, and J. Linderyd, "Integrated Simulation and Engine Test of Closed Loop HCCI Control by Aid of Variable Valve Timings," *SAE paper*, no. 2003-01-0748, 2003. 5

[27] J. S. Souder, J. K. Hedrick, J. H. Mack, and R. W. Dibble, "Microphones and Knock Sensors for Feedback Control of HCCI Engines," *ICEF*, no. ICEF2004-960, 2004. 5

[28] F. Agrell, H. Ångström, B. Eriksson, J. Wilkander, and J. Linderyd, "Transient Control of HCCI Through Combined Intake and Exhaust Valve Actuation," *SAE paper*, no. 2003-01-3172, 2003. 5

[29] G. M. Shaver and J. C. Gerdes, "Cycle to Cycle Control of HCCI Engines," *IMECE*, no. IMECE2003-41966, 2003. 6

[30] C. J. Chiang and A. G. Stefanopoulou, "Control of Thermal Ignition in Gasoline Engines," *American Control Conf.*, 2005. 6

[31] G. Haraldsson, P. Tunestål, B. Johansson, and J. Hyvönen, "Transient Control of a Multi Cylinder HCCI Engine During a Drive Cycle," *SAE paper*, no. 2005-01-0153, 2005. 6, 19

[32] G. M. Shaver, J. C. Gerdes, and M. Roelle, "Physics-Based Closed-Loop Control of Phasing, Peak Pressure and Work Output in HCCI Engines Utilizing Variable Valve Actuation," *American Control Conf.*, 2004. 6

[33] N. J. Killingsworth, S. M. Aceves, D. L. Flowers, and M. Krstic, "Extremum Seeking Tuning of an Experimental HCCI Engine Combustion Timing Controller," *American Control Conf.*, 2007. 6

[34] M. Karlsson, K. Ekholm, P. Strandh, R. Johansson, P. Tunestål, and B. Johansson, "Closed-loop control of combustion phasing in an HCCI engine using VVA and variable EGR," in *5th IFAC Symp. Advances in Auto. Contr.*, 2007. 6, 43, 88

[35] N. Ravi, H.-H. Liao, A. F. Jungkunz, C.-F. Chang, H. H. Song, and J. C. Gerdes, "Modeling and Control of an Exhaust Recompression HCCI Engine Using Split Injection," *J. Dyn. Syst. Meas. Control*, vol. 134, no. January 2012, pp. 011 016–1–12, 2012. 6, 15, 19

[36] J. Bengtsson, P. Strandh, R. Johansson, P. Tunestål, and B. Johansson, "Model predictive control of Homogeneous Charge Compression Ignition (HCCI) engine dynamics," *IEEE Int. Conf. Control Applications*, pp. 1675–1680, 2006. 6

[37] C.-J. Chiang and C.-L. Chen, "Constrained control of Homogeneous Charge Compression Ignition (HCCI) engines," *5th IEEE Conf. Industrial Electronics and Applications*, 2010. 6

[38] N. Ravi, H.-H. Liao, A. F. Jungkunz, A. Widd, and J. C. Gerdes, "Model predictive control of HCCI using variable valve actuation and fuel injection," *Control Eng. Prac.*, vol. 20, pp. 421–430, 2012. 6

[39] H. Yilmaz, "2012 DOE Merit Review – ACCESS," http://www1.eere.energy.gov/vehiclesandfuels/pdfs/merit_review_2012/adv_combustion/ace066_yilmaz_2012_o.pdf, 2012, [Online; accessed 9-Sep-2012]. 7

[40] G. Haraldsson, P. Tunestal, B. Johansson, and J. Hyvönen, "HCCI closed-loop combustion control using fast thermal management," *SAE Paper*, no. 2004-01-0943, pp. 599——610, 2004. 11

[41] D. Lee, L. Jiang, H. Yilmaz, and A. G. Stefanopoulou, "Air charge control for turbocharged spark ignition engines with internal exhaust gas recirculation," in *American Control Conference (ACC), 2010*. IEEE, 2010, pp. 1471–1476. 11

[42] M. Christensen, A. Hultqvist, and B. Johansson, "Demonstrating the multi fuel capability of a homogeneous charge compression ignition engine with variable compression ratio," *SAE Paper*, no. 1999-01-3679, 1999. 11

[43] G. Haraldsson, P. Tunestal, B. Johansson, and J. Hyvönen, "HCCI combustion phasing in a multi cylinder engine using variable compression ratio," *SAE Paper*, no. 2002-01-2858, 2002. 11

[44] A. Babajimopoulos, P. V. Challa, G. A. Lavoie, and D. Assanis, "Model-based Assessment of Two Variable Cam Timing Strategies for HCCI Engines: Recompression vs. Rebreathing," *ASME Internal Combustion Engine Division Spring Technical Conf.*, 2009, ICES2009-76103. 12, 19

[45] E. Hellström, J. Larimore, A. G. Stefanopoulou, J. Sterniak, and L. Jiang, "Quantifying cyclic variability in a multicylinder HCCI engine with high residuals," *J. Eng. Gas Turbines and Power*, vol. 134, no. 11, p. 112803, 2012. 13, 35, 40, 69, 71, 73, 77, 81, 96

[46] R. Fitzgerald, R. Steeper, J. Snyder, R. Hanson, and R. Hessel, "Determination of cycle temperature and residual gas fraction for HCCI negative valve overlap operation," *SAE Int. J. Engines*, no. 3(2010-01-0343), pp. 124–141, 2010. 13

[47] R. P. Fitzgerald and R. Steeper, "Thermal and Chemical Effects of NVO Fuel Injection on HCCI Combustion," *SAE*, no. 2010-01-0164, 2010. 15

[48] N. Ravi, H.-h. Liao, A. F. Jungkunz, and J. C. Gerdes, "Modeling and control of exhaust recompression HCCI using split injection," *American Control Conf.*, 2010. 15

[49] C. Marriott and R. Reitz, "Experimental investigation of direct injection-gasoline for premixed compression ignited combustion phasing control," *SAE Paper*, no. 2002-01-0418, 2002. 15

[50] J. Bengtsson, P. Strandh, R. Johansson, P. Tunestål, and B. Johansson, "Hybrid modelling of Homogeneous Charge Compression Ignition (HCCI) engine dynamic – a survey," *Int. J. Control*, vol. 80, no. 11, pp. 1814–1848, Nov. 2007. 16

[51] J. Bengtsson, M. Gäfvert, and P. Strandh, "Modeling of HCCI Engine Combustion for Control Analysis," *IEEE Conf. Decision and Control*, pp. 1682–1687, 2004. 18, 29

[52] M. Halstead, L. Kirsch, and J. Keck, "The Autoignition of Hydrocarbon Fuels at High Temperatures and Pressures-Fitting of a Mathematical Model," *Combustion and Flame*, vol. 30, pp. 45–60, 1977. 18, 29

[53] C. G. Mayhew, K. L. Knierim, N. A. Chaturvedi, S. Park, J. Ahmed, and A. Kojic, "Reduced-order modeling for studying and controlling misfire in four-stroke HCCI engines," *IEEE Conf. Decision and Control*, pp. 5194–5199, 2009. 19

[54] G. Shaver and J. Gerdes, "Cycle-to-cycle control of HCCI engines," *ASME Int. Mech. Eng. Congress and Exposition*, no. IMECE 2003-41966, 2003. 19

[55] D. Rausen, A. Stefanopoulou, J.-M. Kang, J. Eng, and T.-W. Kuo, "A mean value model for control of Homogeneous Charge Compression Ignition (HCCI) engines," *J. Dyn. Syst. Meas. Control*, vol. 127, no. 3, pp. 355–362, Sep. 2005. 19

[56] C. Chiang and A. G. Stefanopoulou, "Stability analysis in homogeneous charge compression ignition (HCCI) engines with high dilution," *IEEE Trans. Control Syst. Technol.*, vol. 15, no. 2, pp. 209–219, March 2007. 19, 69, 73, 75

[57] D. Blom, M. Karlsson, K. Ekholm, P. Tunestål, and R. Johansson, "HCCI engine modeling and control using conservation principles," *SAE paper*, no. 2008-01-0789, 2008. 19

[58] M. Shahbakhti and C. R. Koch, "Physics Based Control Oriented Model for HCCI Combustion Timing," *J. Dyn. Syst. Meas. Control*, vol. 132, no. 2, p. 021010, 2010. 19

[59] N. Ravi, M. J. Roelle, H.-H. Liao, A. F. Jungkunz, C.-F. Chang, S. Park, and J. C. Gerdes, "Model-Based Control of HCCI Engines Using Exhaust Recompression," *IEEE Trans. Control Syst. Technol.*, vol. 18, no. 6, pp. 1289–1302, Nov. 2010. 19

[60] R. Perry and D. Green, *Perry's Chemical Engineers' Handbook*. McGraw-Hill New York, 2008. 23

[61] N. Ravi, N. Chaturvedi, J. Oudart, D. Cook, E. Doran, A. Kojic, and M. Pimpare, "Control-oriented physics-based modeling of engine speed effects in HCCI," *IEEE Conf. Decision and Control*, 2012. 27

[62] C.-J. Chiang, "Modeling and control of Homogeneous Charge Compression Ignition engines with high dilution," Ph.D. dissertation, University of Michigan, 2007. 29

[63] H. J. Curran, P. Gaffuri, W. J. Pitz, and C. K. Westbrook, "A Comprehensive Modeling Study of Iso- Octane Oxidation," *Combust. Flame*, vol. 129, pp. 253–280, 2002. 29

[64] S. R. Turns, *An Introduction to Combustion: Concepts and Applications*, 2nd ed. McGraw-Hill series in mechanical engineering, 2000. 29, 30

[65] J. Livengood and P. Wu, "Correlation of autoignition phenomena in internal combustion engines and rapid compression machines," in *Symposium (International) on Combustion*, vol. 5, no. 1. Elsevier, 1955, pp. 347–356. 29

[66] X. He, M. Donovan, B. Zigler, T. Palmer, S. Walton, M. Wooldridge, and A. Atreya, "An experimental and modeling study of iso-octane ignition delay times under Homogeneous Charge Compression Ignition conditions," *Combustion and Flame*, vol. 142, no. 3, pp. 266–275, 2005. 29

[67] G. M. Shaver, J. C. Gerdes, M. J. Roelle, P. A. Caton, and C. F. Edwards, "Dynamic modeling of residual-affected homogeneous charge compression ignition engines with variable valve actuation," *J. Dyn. Syst. Meas. Control*, vol. 127, no. 3, p. 374, 2005. 29

[68] J. Larimore, E. Hellström, J. Sterniak, L. Jiang, and A. Stefanopoulou, "Experiments and Analysis of High Cyclic Variability at the Operational Limits of Spark-Assisted HCCI Combustion," in *American Control Conf.*, 2012. 35

[69] B. Allison and A. Isaksson, "Design and performance of mid-ranging controllers," *J. Proc. Control*, vol. 8, no. 5-6, pp. 469–474, 1998. 43, 88

[70] N. Ravi, H.-H. Liao, A. F. Jungkunz, and J. C. Gerdes, "Mid-ranging control of a multi-cylinder HCCI engine using split fuel injection and valve timings," *6th IFAC Symp. Advances in Auto. Contr.*, 2010. 43, 88

[71] S. Jade, E. Hellström, L. Jiang, and A. Stefanopoulou, "Fuel governor augmented control of recompression HCCI combustion during large load transients," in *American Control Conf.*, 2012. 44, 122

[72] M. Voicu, *Advances in Automatic Control*, ser. The Kluwer international series in engineering and computer science. Kluwer Academic Press, 2004. 48, 49

[73] A. Casavola and E. Mosca, "Reference governor for constrained uncertain linear systems subject to bounded input disturbances," *Conf. Decision and Control*, pp. 3531–3536, 1996. 56

[74] P. Kapasouris, M. Athans, and G. Stein, "Design of Feedback Control Systems for Stable Plants with Saturating Actuators'," *IEEE Conf. Decision and Control*, 1988. 56

[75] ——, "Design of Feedback Control Systems for Unstable Plants with Saturating Actuators," *IFAC Symposium on Nonlinear Control System Design*, 1990. 56

[76] E. G. Gilbert and K. T. Tan, "Linear Systems with State and Control Constraints: The Theory and Application of Maximal Output Admissible Sets," *IEEE Trans. Autom. Control*, vol. 36, pp. 1008–1020, 1991. 56

[77] A. Bemporad, A. Casavola, and E. Mosca, "Nonlinear control of constrained linear systems via predictive reference management," *IEEE Trans. Autom. Control*, vol. 42, no. 3, pp. 340–349, 1997. 56

[78] A. Bemporad, "Reference governor for constrained nonlinear systems," *IEEE Trans. Autom. Control*, vol. 43, no. 3, pp. 415–419, 1998. 56

[79] E. Gilbert, I. Kolmanovsky, and K. Tan, "Discrete-time reference governors and the nonlinear control of systems with state and control constraints," *Int. J. Robust Nonlin. Control*, vol. 5, pp. 487–504, 1995. 56

[80] E. G. Gilbert and I. Kolmanovsky, "Fast reference governors for systems with state and control constraints and disturbance inputs," *Int. J. Robust Nonlinear Control*, vol. 9, pp. 1117–1141, 1999. 56, 58

[81] ——, "Set-point control of nonlinear systems with state and control constraints : a Lyapunov function reference governor approach," *Conf. Decision and Control*, pp. 2507–2512, 1999. 56

[82] E. Gilbert and I. Kolmanovsky, "Nonlinear tracking control in the presence of state and control constraints: a generalized reference governor," *Automatica*, vol. 38, no. 12, pp. 2063–2073, Dec. 2002. 56

[83] J. Sun and I. Kolmanovsky, "Load governor for fuel cell oxygen starvation protection: a robust nonlinear reference governor approach," *IEEE Trans. Control Syst. Technol.*, vol. 13, no. 6, pp. 911–920, 2005. 56

[84] A. Vahidi, I. Kolmanovsky, and A. Stefanopoulou, "Constraint management in fuel cells : a fast reference governor approach," *American Control Conf.*, vol. 6, pp. 3865 – 3870, 2005. 56, 58

[85] V. Tsourapas, J. Sun, and A. Stefanopoulou, "Incremental step reference governor for load conditioning of hybrid fuel cell and gas turbine power plants," *American Control Conf.*, pp. 2184–2189, Jun. 2008. 56

[86] ——, "Incremental step reference governor for load conditioning of hybrid fuel cell and gas turbine power plants," *IEEE Trans. Control Syst. Technol.*, vol. 17, no. 4, pp. 756–767, Jul. 2009. 56

[87] J. M. Elder, J. T. Boys, and J. L. Woodward, "Integral cycle control of stand-alone generators," *IEE Proc. C - Gener. Transm. Distrib.*, vol. 132, no. 2, pp. 57–66, 1985. 56

[88] D. Henderson, "An advanced electronic load governor for control of micro hydro-electric generation," *IEEE Trans. Energy Convers.*, vol. 13, no. 3, pp. 300–304, 1998. 56

[89] I. Kolmanovsky, E. Gilbert, and J. Cook, "Reference governors for supplemental torque source control in turbocharged diesel engines," in *American Control Conf.*, 1997. 56

[90] C. Daw, K. Edwards, R. Wagner, and J. J.B. Green, "Modeling cyclic variability in spark-assisted HCCI," *J. Eng. Gas Turbines and Power*, vol. 130, no. 5, p. 052801, 2008. 69, 73, 96

[91] A. Ghazimirsaied, M. Shahbakhti, and C. Koch, "HCCI engine combustion phasing prediction using a symbolic-statistics approach," *J. Eng. Gas Turbines and Power*, vol. 132, no. 8, p. 082805, 2010. 69

[92] H.-H. Liao, A. Widd, N. Ravi, A. F. Jungkunz, J.-M. Kang, and J. C. Gerdes, "Control of recompression HCCI with a three region switching controller," *Control Eng. Prac.*, vol. 21, no. 2, pp. 135–145, 2013. 69, 70, 73, 75, 93, 100

[93] E. Hellström, J. Larimore, S. Jade, L. Jiang, and A. G. Stefanopoulou, "Reducing cyclic variability while regulating combustion phasing in a four-cylinder HCCI engine," *IEEE Transactions on Control Systems Technology*, 2013, to appear. 70, 73, 122

[94] H.-H. Liao, N. Ravi, A. Jungkunz, A. Widd, and J. C. Gerdes, "Controlling Combustion Phasing of Recompression HCCI with a Switching Controller," *6th IFAC Symp. Advances Auto. Control*, 2010. 71

[95] L. Koopmans, O. Backlund, and I. Denbratt, "Cycle to cycle variations: Their influence on cycle resolved gas temperature and unburned hydrocarbons from a camless gasoline compression ignition engine," *SAE*, no. 2002-01-0110, 2002. 73

[96] R. M. Wagner, K. D. Edwards, C. S. Daw, J. B. Green, Jr., and B. G. Bunting, "On the nature of cyclic dispersion in spark assisted HCCI combustion," in *SAE World Congress*, 2006, SAE 2006-01-0418. 73

[97] M. Sjöberg and J. E. Dec, "An investigation into lowest acceptable combustion temperatures for hydrocarbon fuels in HCCI engines," *Proceedings of the Combustion Institute*, vol. 30, no. 2, pp. 2719–2726, Jan. 2005. 75

[98] G. Weiss, "Time-reversibility of linear stochastic processes," *J. Appl. Probab.*, vol. 12, no. 4, pp. 831—836, 1975. 81

[99] S. Jade, E. Hellström, J. Larimore, L. Jiang, and A. Stefanopoulou, "Reference Governor for Load Control in a Multi-Cylinder Recompression HCCI Engine," *IEEE Transactions on Control Systems Technology*, 2013, to appear. 92, 122

[100] C. Finney, J. Green Jr., and C. Daw, "Symbolic time-series analysis of engine combustion measurements," *SAE paper*, no. 980624, 1998. 96

[101] S. Jade, J. Larimore, E. Hellström, L. Jiang, and A. Stefanopoulou, "Controlled Load and Speed Transitions in a Multi-Cylinder Recompression HCCI Engine," *IEEE Transactions on Control Systems Technology*, 2013, submitted for review. 122

[102] J. Larimore, S. Jade, E. Hellström, A. G. Stefanopoulou, and L. Jiang, "Adaptive Control of a Recompression 4-Cylinder HCCI Engine," *IEEE Transactions on Control Systems Technology*, 2013, submitted for review. 122

[103] J. Larimore, S. Jade, E. Hellström, A. G. Stefanopoulou, J. Vanier, and L. Jiang, "Online adaptive residual mass estimation in a multicylinder recompression HCCI engine," in *Proc. ASME Dynamic Systems and Control Conference*, Palo Alto, CA, USA, 2013. 122

[104] S. Jade, E. Hellström, J. Larimore, L. Jiang, and A. Stefanopoulou, "Enabling Large Load Transitions on Multicylinder Recompression HCCI Engines using Fuel Governors," 2013, American Control Conf. 122

[105] S. Jade, E. Hellström, A. Stefanopoulou, and L. Jiang, "On the influence of composition on the thermally-dominant recompression HCCI combustion dynamics," in *ASME Dyn. Syst. Contr. Conf.*, 2011. 123

[106] J. Larimore, S. Jade, L. Jiang, E. Hellstrom, A. Stefanopoulou, and J. Vanier, "Device and method for real-time residual gas estimation," 2013, Application filed, Patent App. No.: 61/766754. 123

[107] S. Jade, E. Hellstrom, A. Stefanopoulou, and L. Jiang, "Fueling strategy for controlled-autoignition engines," Apr. 11 2013, US Patent 20,130,090,838 (Application). 123

[108] ——, "Fuel governor for controlled autoignition engines," Apr. 11 2013, US Patent 20,130,090,837 (Application). 123